UNIVERSITA' DEGLI STUDI DI VERONA

DEPARTMENT OF

Computer Science

GRADUATE SCHOOL OF

Natural Science and Engineering

DOCTORAL PROGRAM IN

Nanoscience and Advanced Technologies

Cycle/year
37th, 2022

TITLE OF THE DOCTORAL THESIS

Studying Antimony Selenide Thin Film Solar Cells

S.S.D. **PHYS-03/A**

Coordinator: Prof. **Adolfo Speghini**

Signature

Tutor: Prof. **Alessandro Romeo**

Signature

Doctoral Student: Dott.ssa: **Narges Torabi**

Signature

La borsa di dottorato è stata cofinanziata con risorse del
Programma Operativo Nazionale Ricerca e Innovazione 2014-2020, risorse FSE REACT-EU
Azione IV.4 “Dottorati e contratti di ricerca su tematiche dell’innovazione”
e Azione IV.5 “Dottorati su tematiche Green”

This research was supported by a PhD scholarship funded under the PON (National Operational Program) on Research and Innovation 2014-2020, under Ministerial Decree No. 1061/2021 (M.D. 1061/2021 PON REACT-EU), co-financed by the European Social Fund (ESF)– REACT-EU initiative. I gratefully acknowledge this financial support, which has enabled my research and academic development.

Studying Antimony Selenide Thin Film Solar Cells

Narges Torabi

PhD Thesis

2025

Life is not easy for any of us. But what of that? We must have perseverance and, above all, confidence in ourselves. We must believe that we are gifted for something, and that this thing, at whatever cost, must be attained.

Marie Curie

Abstract

In the field of thin-film photovoltaics, exploring and optimizing various materials and techniques is crucial for advancing device performance. Modifying different components in thin-film solar cells enhances efficiency and deepens our understanding of the underlying physical phenomena.

This thesis investigates Sb_2Se_3 thin-film solar cells grown by the thermal evaporation technique in a superstrate configuration device. It explores both cadmium-based (Cd-based) and cadmium-free (Cd-free) window layers, as well as the influence of the absorber layer thickness on the device performance. Additionally, it evaluates the effect of air post-annealing treatment (PAT) as a passivation method.

The structural properties of Sb_2Se_3 and the performance of CdS/Sb_2Se_3 devices were analyzed. Sulfur diffusion at this interface could alter the optoelectrical properties of Sb_2Se_3, resulting in a V_{oc} deficit. To address this, CdSe was introduced as an alternative buffer layer, eliminating the sulfur interdiffusion. Moreover, the presence of selenium in CdSe helped mitigate selenium loss at the junction by reducing the concentration gradient. The CdSe/ Sb_2Se_3 solar cells showed remarkable stability, and regardless of a relatively narrow bandgap of CdSe, this replacement also increased photocurrent density (J_{sc}). However, the use of Cd-based materials window layers not only limits light absorption at shorter wavelength regions but also leads to Cd diffusion in the Sb_2Se_3 film.

To overcome these limitations, a transparent, Cd-free alternative material, tin oxide (SnO_2), was employed and deposited using atomic layer deposition (ALD) at EMPA laboratories. A 15 nm SnO_2 film served as a suitable substrate for growing Sb_2Se_3 film, increasing the grain size (to approximately 1 μm). By applying this wide band gap material, J_{sc}, and carrier collection at the short wavelength regions improved. However, a higher doping density and, consequently, a higher V_{oc} compared to CdSe-based solar cells were also observed.

Also, the effects of absorber thickness were analyzed since Sb_2Se_3 shows a superior absorption coefficient. The structural and electrical properties of solar cells with 400 and 1200 nm thickness of Sb_2Se_3 were compared. We observed that an ultra-thin film of 400 nm captures photons effectively. The solar cell illustrated higher performance, particularly for the J_{sc} value.

Applying PAT in air ambient at a low temperature on the finished devices shows passivating behavior. Oxygen diffusion throughout Sb_2Se_3 films differs with the film thickness. However, the oxygen exposure during the annealing always reduces the defect density. This treatment improved the overall photovoltaic parameters, especially the V_{oc} and fill factor values.

Acknowledgments

Looking back on my PhD journey, I feel thankful for all the amazing people who helped me along the way. I could not have gone through all the challenges and growth without everyone's support.

First and foremost, I am deeply thankful to my supervisor, Professor Alessandro Romeo, for his support and guidance. Through all the ups and downs, he stood by me, encouraged my independence, and helped me grow not only as a researcher but also as a person.

I also want to thank my colleagues and friends, Drs. Prubeesh Punathil, Solidea Zanetti, Simya OK, Ikram Anefnaf, Mariyam Mukhtar, Sharmiladevi Ramamoorthy, and Elisa Artegiani – especially during my time at Empa laboratories. You made the lab a friendly and supportive place. The knowledge we shared, the laughter we had, and the friendships we formed made even the toughest days easier. Also, I appreciate Dr. Ivan Rimmaudo's support during his visit and beyond.

I am very grateful to the Thin Films and Photovoltaics Laboratory at Empa for their warm welcome during my visit. A heartfelt thank you to Dr. Romain Carron for his kindness and help during my stay. To Drs. Evgeniia Gilshtein, Simon Moser, Huagui Lai, Maximilian Krause, and Nisika, thank you for making my time there fulfilling and enjoyable. The friendships and support I found at Empa helped me through difficult days, and I will always be thankful for that.

To my family and loved ones –being away from you has been one of the hardest parts of this journey. Mom and Dad, I felt your love and support every day –even the days I couldn't call. Your belief in me gave me the strength to keep going, even when things got hard. To my brother – your love has always been a constant in my life. Being apart from you during this time was incredibly tough, and I missed our bond more than words can say. Knowing you were cheering me on, even from afar, meant the world to me.

And to the friends I made outside the lab, you have been my escape, support, and joy. Your kindness and friendship have meant the world to me through our conversations and laughter and simply being there when I needed it.

This journey has changed me in ways I never expected. It has been challenging but also fulfilling and unforgettable. I owe so much to everyone who stood by me and helped me grow.

From the bottom of my heart—thank you.

Funding and Collaboration Acknowledgments

This thesis was conducted as part of multiple research projects, which provided both financial and collaborative support:

- **INSOBILD (Innovative Solutions for Building Integrated Photovoltaic)**, Ref. 2022.0094- ID 52271- CUP B33C22001760007, funded by **Fondazione Cariverona**.
- **ACT-FAST: Sustainable Antimony Chalcogenide Thin-Film Tandem Solar Technology**, funded by the **Clean Energy Transition Partnership**.
- **RENEW-PV (CA21248)**, funded by the **European Cooperation in Science and Technology (e-COST)**. I also gratefully acknowledge e-COST for supporting conference participation and short research visits.

I am also deeply appreciative of the **Thin Film and Photovoltaic Laboratory team at Empa** for their collaboration during my research visit, particularly for their support in SnO_2 growth via ALD and the characterization performed at their facilities.

My gratitude extends to **NOIVION** and, in particular, **Dr. Gianpiero Tedeschi** for their collaboration in the growth of Sb_2Se_3 films.

I would like to express my sincere gratitude to **Dr. José María Delgado Sánchez, University of Seville,** for his invaluable assistance in thin-film characterization.

I would also like to acknowledge the **Technological Platform Center (CPT) at the University of Verona**, especially **Dr. Marco Giarola**, for his support in Raman measurements.

I am grateful to **Dr. Meneghesso Gaudenzio's research group at the University of Padua** for their contributions to device characterization.

Finally, I would also like to acknowledge my involvement in organizing the 14th Kesterite + RenewPV, the international workshop on Kesterite-based thin film solar cells and on new materials for photovoltaics, which took place on 26-28 June 2024 at the University of Verona.

Publications:

Directly related to this thesis:

Torabi, N., Artegiani, E., Gasparotto, A., Piccinelli, F., Meneghini, M., Meneghesso, G. and Romeo, A., 2023. **Analysis of CdSe as an alternative buffer layer for Sb_2Se_3 solar cells. Solar Energy**, 264, p.111990.

Torabi, N., Delgado-Sanchez, J. M., Kuliček, J., Rezek. B., Artegiani, E., Jakuza, P., Meneghini, M., Romeo, A., **The effect of thickness and air annealing on electrical and structural properties of Sb_2Se_3 solar cells by thermal evaporation**, submitted for publication.

Torabi, N., Mukhtar, M., Artegiani, E., Anefnaf, I., Carron, R. and Romeo, A., 2024, June. **Comparison of SnO_2 and CdSe Buffer Layers for Sb_2Se_3 Thin Film Solar Cells**. In 2024 IEEE 52nd Photovoltaic Specialist Conference (PVSC) (pp. 1-4). IEEE.

Torabi, N., Zanetti, S., Artegiani, E., Piccinelli, F., Punathil, P. and Romeo, A., 2022. **comparison of CdS and CdSe buffer layers for antimony selenide (Sb_2Se_3) solar cells by vacuum evaporation**. In Proceedings of 8th World Conference on Photovoltaic Energy Conversion (pp. 406-408).

Torabi. N., Artegiani. E., Tedeschi. G., Anefnaf. I., Olavil Karayi. S., Mukhtar. M., and Romeo. A., 2023, **Growth of Sb_2Se_3 by Ionized Jet Deposition for Thin Film Solar Cells Application**, In Proceedings of 40th European Photovoltaic Solar Energy Conference.

Indirectly related to this thesis:

Anefnaf, I., Simya, O.K., Artegiani, E., **Torabi, N.**, Mukhtar, M., Jakuza, P., Meneghini, M. and Romeo, A., 2024, June. **Investigation of $Cu_2ZnSn(S, Se)_4$ Solar Cells Fabricated Through Aqueous Non-Vacuum Spray Deposition**. In 2024 IEEE 52nd Photovoltaic Specialist Conference (PVSC) (pp. 0290-0294). IEEE.

Mukhtar, M., Artegiani, E., **Torabi, N.**, Anefnaf, I., Barrantes, J.J.N., Meneghini, M. and Romeo, A., 2024, June. **Study of Ultra-Thin Cadmium Telluride Solar Cells**. In 2024 IEEE 52nd Photovoltaic Specialist Conference (PVSC) (pp. 0648-0651). IEEE.

Simya, O.K., Anefnaf, I., Punathil, P., Artegiani, E., **Torabi, N.**, Mukhtar, M. and Romeo, A., 2024, June. **Impact of Lithium as Interfacial Treatment for CZTSSe Solar Cells**. In 2024 IEEE 52nd Photovoltaic Specialist Conference (PVSC) (pp. 0640-0644). IEEE.

Artegiani, E., Punathil, P., Zanetti, S., **Torabi, N.** and Romeo, A., 2022. **study of cdsete/cdte devices fabricated by thermal evaporation**. In Proceedings of 8th World Conference on Photovoltaic Energy Conversion (pp. 273-275).

Punathil, P., Zanetti, S., Artegiani, E., **Torabi, N.** and Romeo, A., 2022. **analysis of selenization temperature for the performance improvement of spin coated** CZTSSe **solar cells**. In Proceedings of 8th World Conference on Photovoltaic Energy Conversion (pp. 339-341).

Razykov, T.M., Bosio, A., Kouchkarov, K.M., Khurramov, R., Tivanov, M.S., Bayko, D.S., Romeo, A., Romeo, N., **Torabi, N.** and Utamuradova, S.B., 2023, **Effect of Substrate Temperature on Structure, Morphology and Optical Properties of Sb2Se3 Thin Films Fabricated by Chemical-Molecular Beam Deposition Method from Sb and Se Precursors for Solar Cells**, In Proceedings of 40th European Photovoltaic Solar Energy Conference.

Olavil Karayi, S., Anefnaf, I., **Torabi, N.**, Punathil, P., Zanetti, S., Lozzi, L., Artegiani, E., Mukhtar, M., Romeo, A., 2023, **Enhanced Performance of CZTSSe Solar Cells through Chlorine-Based Impurity Inclusion Process**, In Proceedings of 40th European Photovoltaic Solar Energy Conference.

Artegiani, E., Gasparotto, A., Mukhtar, M., Olavil Karayi, S., **Torabi, N.**, Anefnaf, I., Romeo, A., 2023, **Study of different approaches to fabricate CdSeTe/CdTe devices by thermal evaporation**, In Proceedings of 40th European Photovoltaic Solar Energy Conference.

Table of Contents

Chapter One

Introduction

Experiencing simple pleasures–like feeling the Spring breeze or walking on a rainy afternoon–has taken on new meaning over the last decade: climate change has transformed our world. Across the planet, climate predictability has become a challenge as shifting weather patterns have altered what we once took for granted. These changes signal a more significant challenge beyond our daily experiences–the global energy crisis.

1.1 Energy Crisis

Since the pre-industrial era, Earth's temperature has increased by approximately 1°C [1], declaring the startling amount of heat human activities have trapped. This is unsurprising as global energy consumption has skyrocketed over the past two centuries. Fossil fuels supply more than 80% of our energy needs (Figure 1.1) [2], emitting a vast combustion byproduct, CO_2 emissions, into the atmosphere. This disturbs the energy current balance in Earth's atmosphere, resulting in global warming. One step to mitigate this issue was the adoption of the Paris Agreement by almost all countries worldwide, aiming to keep the global temperature

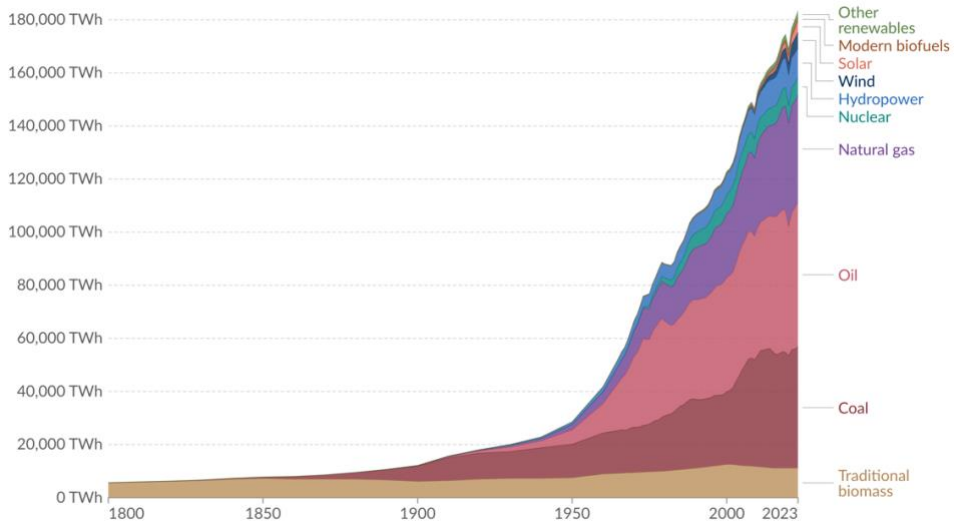

Figure 1.1 Global energy consumption [2].

increase below a threshold of 1.5°C [3]. Additionally, fossil fuel resources will be depleted one day, and before then, we should find alternative green energy sources.

Two alternative energy sources have emerged as low-carbon emission options to meet global energy demands. First, nuclear energy is known for its high efficiency but is often accompanied by concerns related to safety, waste management, and high operational costs. Second, renewable energy sources such as wind, hydropower, and solar are abundant and inexhaustible. Solar energy is one of the most powerful energy sources, and sunlight is the most abundant energy source that Earth receives. It is free, green, and mostly available across the world. Besides sunlight affecting and deriving countless natural processes, it can be converted to heat or electrical energy. The technology to convert sunlight directly to electricity is photovoltaic (PV).

1.2 Photovoltaic History

The evolution of photovoltaic technology began in 1839 when Edmond Becquerel discovered the photovoltaic effect. He observed that a silver-coated platinum electrode immersed in the electrolyte under light exposure generates an electric current. In 1873, the photoconductivity of selenium was observed, and after three years, William Adams and Richard Day found that the illumination of selenium contacted to platinum showed a photovoltaic effect. This led to the fabrication of the first solar cell, composed of gold, selenium, and a metal contact, in 1894 by Charles Fritts. Also, the explanation of the photoelectric effect by Albert Einstein in 1904, confirmed by the experiment of Robert Millikan in 1916, enhanced the understanding of the photovoltaic effect. The first silicon-based solar cell was made in 1954 in Bell Laboratories with an efficiency of 6%. So, for the first time, photovoltaic technology was implemented in the real world, but the application was limited by high production cost ($200 per Watt) [4]. However, that technology offered advantages, such as more efficient and remote power supply solutions for space applications, attracting more attention by the late 1950s, which resulted in more research on improving efficiency and reducing production costs. The oil crisis in oil-dependent Western countries during the 1970s led to a pivotal global interest in alternative energy sources, accelerating research in photovoltaic technology [5]. This led to the innovative development of solar cells and more government investment to develop the technology.

1.2.1 First-generation solar cells

The first-generation solar cells are silicon-based solar cells that operate using a homojunction formed by p-type and n-type monocrystalline silicon wafers. These devices' efficiency was initially improved from 6% to 15% within a few years. Subsequent advancements in PV technology further enhanced the efficiency of solar cells and modules, reaching 25% and 19%, respectively [6]. The growth of monocrystalline silicon was an obstacle to mitigating the production costs. Researchers developed multicrystalline silicon solar cells to address this issue, although the efficiency remained lower (19%) than monocrystalline solar cells [7]. Before the 1980s, solar modules were applied in remote locations or for temporary energy supply needs, but after, they found their way to the suburban and urban residential market [5], [8]. Silicon solar cells currently hold more than 90% of the market share [9]. Also, Chinese solar companies such as LONGi Solar and JA Solar have recently expanded their production capacity for high-efficiency monocrystalline silicon solar cells, reducing production costs [10].

1.2.2 Second-generation solar cells

Another step in facing the main challenge of first-generation monocrystalline solar cells was the introduction of thin film technology based on polycrystalline materials. Thin films –with their high absorption coefficient– can effectively capture sunlight using minimal. Thus, they offer advantageous features to reduce fabrication costs and develop innovative PV devices [11]. A thin film is a layer of material with a thickness ranging from few nanometers to a few micrometers. Therefore, it reduces material usage and allows for creative applications such as flexible solar cells. This technology offers various growth techniques, including physical evaporation deposition (PVD), chemical evaporation deposition (CVD), and chemical deposition methods, reducing manufacturing expenses [12].

The second-generation solar cells–thin film solar cells–is based on materials like amorphous silicon (a-Si), cadmium telluride (CdTe), and copper indium gallium diselenide (CIGS). The highest reported efficiencies of these solar cells are 10.2% [13], 23.1% [14], and 23.64% [15], respectively, which is lower than the record efficiency of silicon solar cells, 27.3% [16]. Also, chalcogenide materials such as copper zinc tin sulfide (CZTS) and antimony selenide (Sb_2Se_3)

have been introduced to thin film solar cells as absorbers, offering new possibilities. For instance, CZTS is a promising material with abundant elements that has been introduced as an alternative to CIGS. CZTS solar cells can be processed by solution-based methods, offering an inexpensive fabrication process achieving up to 15% efficiency [17].

One of the main limitations of applying polycrystalline materials in thin film solar cells is the higher defect density, which impacts charge carrier mobility and reduces the device's performance. These defects can result from grain boundaries, non-uniform material deposition, or impurities during fabrication. However, with passivation techniques and optimization of deposition methods, these problems have been considerably overcome [18]. Companies such as First Solar pioneered the thereby growing in importance for the renewable energy industry.

1.2.3 Third-generation solar cells

Third-generation solar cells represent the latest advancements in photovoltaic technology. This generation aims to overcome the efficiency limits and cost barriers of traditional silicon-based solar cells. It utilizes a wide range of new materials and novel designs to improve energy conversion.

The heart of this generation is utilizing advanced materials like perovskites, quantum dots, and organic semiconductors. Perovskite solar cells, in particular, have gained attention because of their outstanding optoelectronic properties, which help them achieve both high efficiency and low-cost manufacturing. The absorption of these materials can be tailored to capture light in different wavelengths effectively [19].

Quantum dots are nanometer-sized semiconductor particles that, because of their size, exhibit quantum effects that change their electronic and optical properties compared to bulk materials. This feature allows engineering the band gap to capture different wavelengths of light, leading to more efficient light absorption [7], [20]. Similarly, organic photovoltaics (OPVs), which use organic molecules or polymers, offer lightweight, flexible, and potentially lower-cost alternatives to traditional solar technologies. These cells are particularly attractive for applications such as wearable electronics, portable devices, and flexible solar panels [21].

Furthermore, third-generation solar cells explore novel cell architectures, including tandem cells, multi-junction devices, and bifacial solar modules. These structures stack multiple layers of materials with different band gaps to capture a broader spectrum of sunlight, significantly enhancing efficiency [22], [23].

The third generation not only leverages novel materials and device design but also integrates photovoltaics with other technologies. For instance, building-integrated photovoltaics (BIPV) apply solar cells directly into buildings, offering new energy-harvesting solutions [24].

Together, these innovations represent the future of solar technology, aiming to drive the widespread adoption of photovoltaics by improving performance, lowering costs, and enabling new applications in various sectors.

Over the past decade, antimony selenide (Sb_2Se_3) has been studied as an emerging absorber in thin-film solar cells due to its promising optoelectronic properties. This thesis investigates antimony selenide (Sb_2Se_3) thin-film solar cells grown by thermal evaporation to gain insights into optimizing their performance. The following chapters present an overview of the working principle of solar cells, the fabrication and characterization methods employed in this thesis, as well as Sb_2Se_3 properties and research trajectory.

Chapter Two

Background

2.1 Photovoltaic effect

The first observation of the photovoltaic effect–*the direct conversion of light into electricity*– was from a photoelectrochemical cell. So, the required steps for the photovoltaic effect can be explained by a hypothetical chemical cell, where light can decompose water to H_2 and O_2. In this non-equilibrium condition, if we do not remove the gases, they will recombine at the same rate as their decomposition, and finally, the gas pressure will stabilize. To remain functional, the gases must be removed; hence, we need a selective filter for one gas type to allow only one type of gas to pass through. However, transmitting the molecules toward the desired filter requires a driving force within the cell [8].

The corresponding process happens for charge carriers in a solid-state solar cell. Photovoltaic devices convert sunlight into electricity in three main steps: *light absorption, charge separation,* and *charge collection*. Through this process, sunlight excites electrons of a light-absorbing material, and then an electric field directs electrons and holes to be collected at an external load circuit [4], [8].

An effective process relies on choosing a suitable material to engineer the device. The unique properties of semiconductors enable the development of photovoltaic technology. The following sections discuss some of the semiconductors' essential properties underpinning this development.

2.2 Semiconductors

While electrons occupy discrete energy levels in an isolated atom, in a solid material– where many atoms come together– the wave function of electrons overlaps. Due to the Pauli exclusion principle that states two electrons cannot occupy the same state, the energy levels split. In a solid, energy levels split into the number of electrons– which is very large–so energy levels

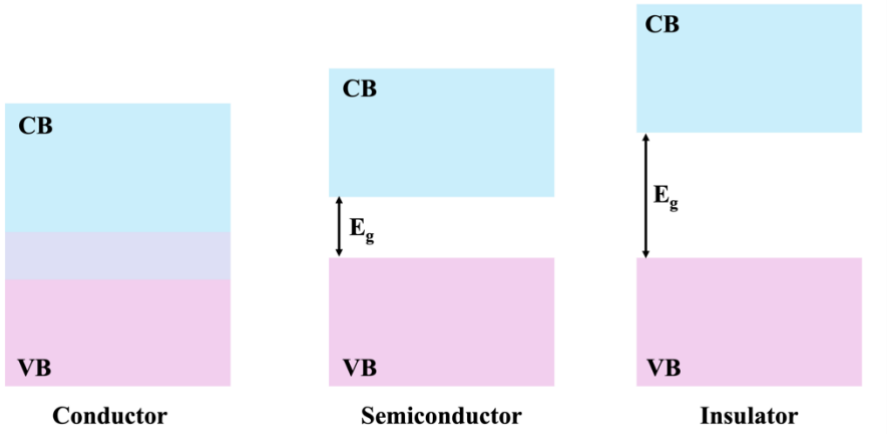

Figure 2.1 Band alignment of conductor, semiconductor, and insulator.

will be close together and appear as a continuum; these allowed energy reigns of electrons are known as bands. These bands are named as valence band (VB), corresponding to the highest occupied energy levels, and conduction band (CB), corresponding to the lowest unoccupied energy levels, and are separated by a gap known as band gap (E_g), the forbidden energy region. Most materials fit into three categories: *conductor, insulator, and semiconductor* [25].

The valence and conduction bands overlap in a conductor, so there is no forbidden gap. Electrons can easily be excited to the conduction band and be free to conduct electricity or heat. When the band gap is large (E_g>3 eV), exciting the electrons from the conduction band to the valence band requires a substantial amount of energy and results in an insulator material. Semiconductors stand between conductors and insulators, as the band gap is between 0.5 to 3 eV, and electrons can be excited by thermal energy, electrical field, or light. Figure 2.1 depicts the schematic of the band alignment of these categories [4].

Understanding the occupation of electron states leads to determining the number of free carriers that turn to define conductivity. Since electrons are half-integral particles, they follow the Fermi-Dirac law, and their distribution depends only on energy. At absolute zero temperature, electrons–with no kinetic energy– always occupy the lowest energy levels. So, the highest energy level at this temperature is called the Fermi energy, E_F. In a conductor, where the conduction and valence bands overlap, the Fermi energy lies within the conduction band where electrons freely move. In contrast, in an insulator, Fermi energy lies somewhere between the band gap, and the large band gap makes the electron excitation difficult. In a semiconductor, Fermi energy is within the band gap, but the smaller band gap allows the thermal excitation of electrons. This level can be changed according to the distribution of electrons and holes in the

conduction and valence bands. An intrinsic semiconductor is a perfect crystal without impurities in which the number of electrons in the conduction band and holes in the valence band are equal. The fermi level is roughly in the middle of the band gap in such material [25]. The introduction of impurity atoms into the lattice –known as doping– of a semiconductor can modify its electrical properties. Donors are atoms with more valence electron(s) required for chemical bonding with the semiconductor atoms. The electron(s) is weakly bound to the donor atoms, and therefore, this extra electron(s) can easily move to the conduction band. These extra electrons raise the Fermi level closer to the conduction band, creating an n-type semiconductor. Conversely, an atom with valence electron(s) less than required for chemical bonding in the semiconductor is an acceptor that creates a vacancy or hole– a conceptual particle representing the absence of an electron– in the valence band. The acceptor atom readily accepts electron(s) from the valence band to fill the hole. In other words, hole(s) loosely bound to the acceptor could easily be donated to the valence band. In a semiconductor doped with an acceptor atom, named a p-type semiconductor, additional hole(s) lower the Fermi level closer to the valence band [4], [8], [25].

2.3 Junctions

In photovoltaic energy conversion, a driving force –*such as an electric field*– is needed to separate charge carriers after light absorption by the material. This is the origin of the photovoltaic effect, and the mechanism can be engineered optimally based on the application. Connecting two materials with different electronic properties, which means different band alignments, provides the desired driving force of solar cells. Two possible connections can be between a metal and a semiconductor, the *Schottky junction*, and between different semiconductors, named a *p-n junction*. Solar cells function mostly by a p-n junction categorizing into *homojunction* and *heterojunction*. Homojunction forms when the p-type and n-type semiconductors of the same material join, and heterojunction is made of two different materials. In both cases, when p-type and n-type semiconductors meet, the p-n junction forms in thermal equilibrium, as will be explained [4].

The n-region has a high electron concentration, and the p-region has a high hole concentration, called majority carriers. After connecting, the majority carriers diffuse across the interface toward the other region, electrons from the n-region, and holes from the p-region, leaving

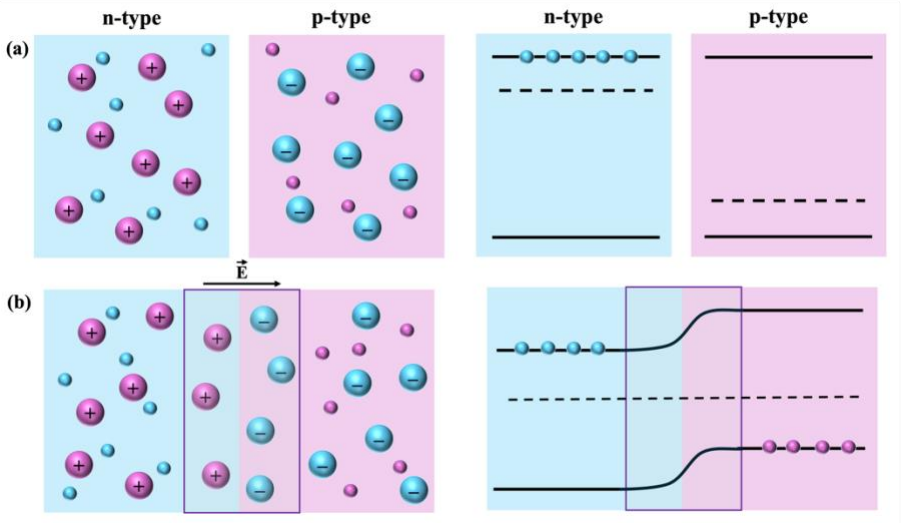

Figure 2.2 Schematic of p-type and n-type semiconductors before connecting (a), and after connecting, the formation of a p-n junction (b).

behind ionized impurity atoms. The movement of carriers depletes the area at the interface known as the space charge region (SCR) or depletion region. This leads to forming an electric field –a built-in voltage (V_{bi}) at the junction– that opposes more carrier diffusion. At the point that the diffusion of majority carriers (electrons in the n-type and holes in the p-type) is balanced by drifting the minority carriers (holes in the n-type and electrons in the p-type) across the junction, thermal equilibrium is reached. In this thermal equilibrium condition, Fermi levels of n-type and p-type materials are equal, and the net current is zero. Figure 2.2 shows an example of a band alignment for p-type and n-type semiconductors before and after connecting. Generally, a p-n junction behaves like a diode, and applying a voltage disturbs the equilibrium, altering the potential barrier of the junction. Figure 2.3 shows a p-n junction under a forward bias. The applied potential opposes the potential barrier of the junction, so the diffusion of the majority carrier increases (net current≠0). The minority carriers at the edge with a diffusion length comparable to the depletion region width can cross over the junction. Finally, these minority carriers recombine with majority carriers, while the majority carriers are supplied from the external circuit, resulting in the net current of majority carriers. The applied field disturbs the distribution of carriers (and Fermi energy levels), and the junction, which is almost free of carriers, will be affected the most. However, we can still consider the Fermi energy levels in p and n regions unaffected as quasi-Fermi levels. Thus, under the forward bias (V>0), the difference of quasi-Femi levels is equal to the applied field $E_{F,p} - E_{F,n} = -eV$. A reverse bias strengthens the internal field of the p-n junction and suppresses the diffusion current.

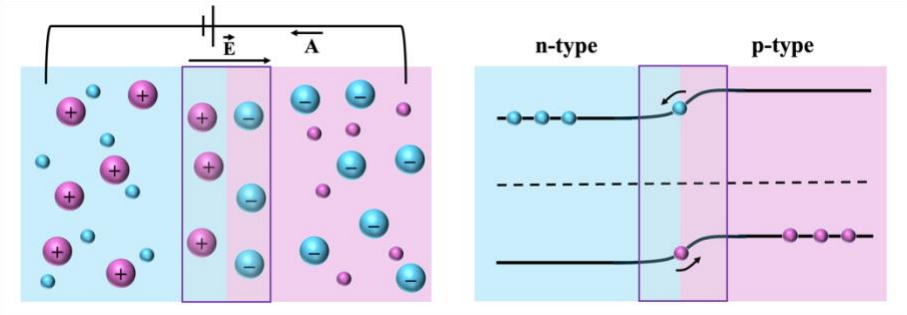

Figure 2.3 Schematic of a p-n junction under a forward bias.

However, the drift current experiences a small increase due to the wider depletion region and is limited by the number of minority carriers [4], [8], [25].

A metal-semiconductor junction can form between a metal with either a large or small work function (the minimum energy needed to move an electron from the material, Fermi level, to a vacuum) and n-type or p-type semiconductors. The band offset of a p-type semiconductor with metal in both small and large work function cases is shown in Figure 2.4. Under a connection between a p-type semiconductor and a metal with a large work function, holes can flow from the semiconductor conduction level to the metal without any barrier. The resultant band bending–known as Ohmic contact–facilitates transmitting the carrier and is ideal for charge collection (Figure 2.4 b). Upon contacting a small work function of metal and a p-type semiconductor, holes move from the semiconductor to metal, leaving behind negative ions. This creates a depletion region in the semiconductor, resulting in downward band bending and making a barrier for hole movement (Figure 2.4 a) [4].

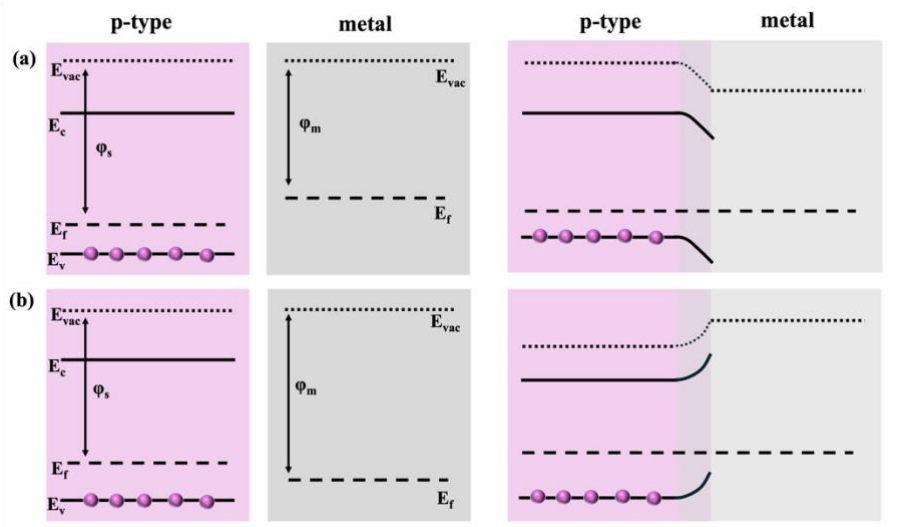

Figure 2.4 Schematic of metal and p-type semiconductor (a) before connecting and (b) after connection.

2.4 Operating principle of p-n junction-based solar cells

So far, the properties of semiconductors make them a suitable choice for making solar cells, and we can design a solar cell based on the photovoltaic effect process. In a typical solar cell structure, n-type and p-type semiconductors can act as electron and hole filters, respectively. The p-n junction of these two provides us with the driving force to transfer the carriers. Finally, the device can be connected to a load by two metal contacts. Therefore, a p-n junction-based solar cell comprises a light absorber layer (p-type), a window layer (n-type), and two metal contacts.

The first step in a PV device operation is light absorption, making the material's bandgap a crucial factor. The bandgap determines the range of photon energies that can be absorbed, as during photoabsorption, only photons with energies equal to or larger than the bandgap can excite electrons. Absorbing a photon with energy equal to E_g excites the electrons from the highest energy level in the valence band (valence band maximum) to the lowest energy level in the conduction band (conduction band minimum). For the photons with $E>E_g$, electrons are promoted to higher energy levels in the conduction band, and then they will be relaxed at the conduction band minimum through a thermal loss. The other consideration of a light harvester material is the band structure that affects efficient light absorption. In the band structure formation of the material, when the valence band maximum (VBM) and the conduction band minimum (CBM) align in momentum space, allowing electrons to transition directly by absorbing or emitting a photon without requiring a change in momentum, such material is direct band gap (Figure 2.5 a). On the other hand, an indirect band gap material has its CBM and VBM at different momentum values, meaning that electron transitions require assistance from a phonon –a quantum of lattice vibration– to conserve momentum (Figure 2.5 b). Materials with suitable direct band gaps provide the effective photo absorption necessary for making an efficient solar cell [4].

The backbone of a solar cell is the p-n junction that provides us with the required driving force to separate the photo-generated charge carriers. Upon joining n-type and p-type semiconductors, the band alignment of the p-n junction under thermal equilibrium is shown in Figure 2.2 b. Once the light hits the absorber layer, electrons are promoted to the CB, leaving behind holes in the VB, increasing minority carriers. The light-generated electrons (holes) diffuse to the depletion region and are swept by the internal field to the n region (p region). As

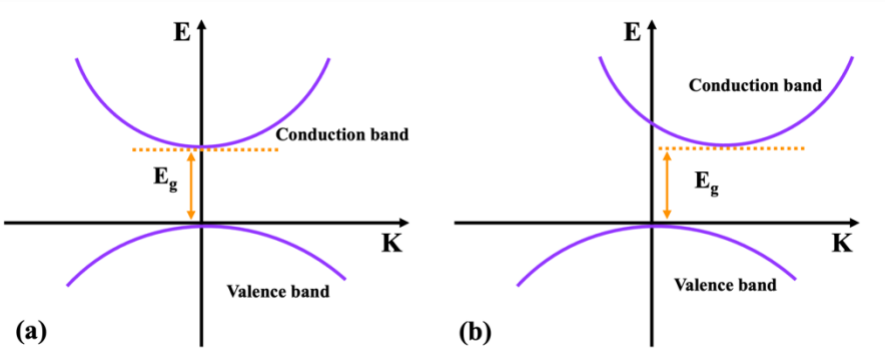

Figure 2.5 A schematic of direct (a) and indirect (b) transition in semiconductors.

this photocurrent flows through the external circuit, it forms an electric field (E′) opposing the internal field of the junction (E), E_{tot}=E-E′. This facilitates the diffusion of the majority carriers toward the junction, increasing the current. However, the overall photocurrent contribution comes mainly from the minority carriers efficiently swept by the junction. Accordingly, the solar cell is no longer in thermal equilibrium under illumination. Instead, it behaves similarly to a p-n junction under forward bias, as discussed in the previous section [4], [8].

The last step is the charge collection once the junction navigates the carriers to p-type and n-type layers. As previously mentioned, Ohmic contact facilitates the charge movement by making an efficient band bending within the semiconductors.

These interactions between the generation, separation, and transport of the light-induced carriers under the internal electric field enable a solar cell to generate electrical power from sunlight. The band offset of a p-n junction-based solar cell is illustrated in Figure 2.6.

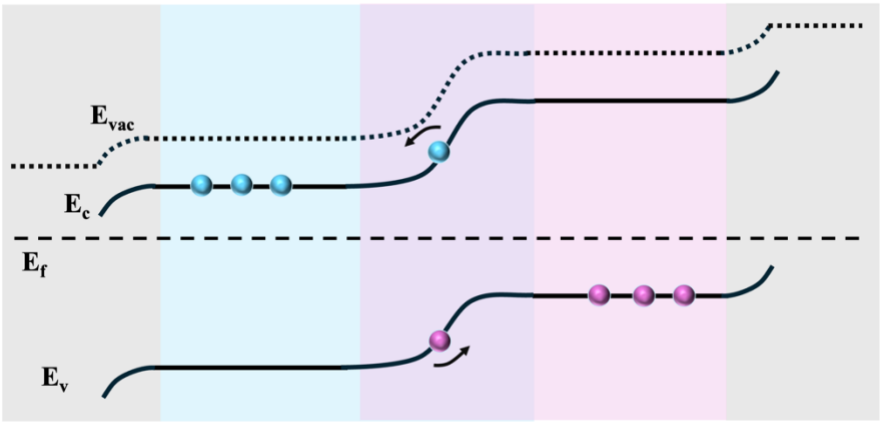

Figure 2.6 Schematic of band alignment of a solar cell.

2.5 Solar cell performance

2.5.1 J-V curve

The performance of a solar cell can be characterized by the current-voltage (I-V) curve. A solar cell performs like a diode in dark conditions so that the Shockley diode equation can define the current for an ideal diode in dark conditions by Equation 2.1:

$$I = I_0(e^{\frac{qV}{nKT}} - 1)$$

We have seen that the behavior of the illuminated p-n junction is similar to that of a p-n junction under forward bias. Consequently, the superposition of photocurrent (I_L) and dark current is the I-V curve of a working solar cell, given by Equation 2.2:

$$I = I_0(e^{\frac{qV}{nKT}} - 1) - I_L$$

However, the light-generated current of a solar cell depends on the illuminated area (solar cell's size), so current density-voltage (J-V) is more useful in characterizing the device. The parameters that can be extracted from the J-V curve are the open-circuit voltage (V_{oc}), short-circuit current density (J_{sc}), maximum power point (P_{max}), and fill factor (FF). V_{oc} is the maximum voltage the solar cell can produce under open-circuit conditions, representing the upper limit of the voltage built up by the p-n junction under illumination. Under short-circuit conditions, when the voltage across the device is zero, the maximum current density that the solar cell can generate is J_{sc}. The solar cell operates between these two points with a power given by P = IV. So, the maximum power point (P_{max}) is the point on the curve where the product of J and V is the highest. The current density (J_m) and voltage (V_m) should be close to J_{sc} and V_{oc} values to optimize the P_{max} (Figure 2.7 (a) illustrates a typical J-V curve of a solar cell). This way, the J-V curve will be a square-like shape. The parameter that measures the squareness of the J-V curve is the fill factor (FF), given by Equation 2.3:

$$FF = \frac{J_m \times V_m}{J_{sc} \times V_{oc}}$$

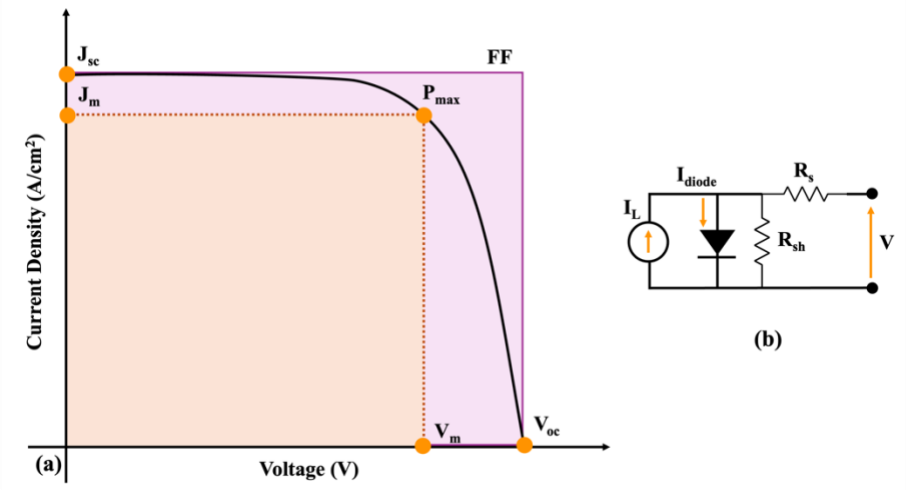

Figure 2.7 (a) typical J-V curve, and (b) the equivalent circuit of a solar cell.

The most critical parameter for evaluating the performance of a solar cell is power conversion efficiency (PEC). It measures how effectively a solar cell converts sunlight into usable electrical power, defined as the ratio of the maximum electrical power output to the solar input power [4], [8], [25], [26].

$$\mathrm{PCE}\ (\eta) = \frac{P_{out}}{P_{in}} = \frac{J_{sc} \times V_{oc} \times FF}{P_{in}}$$

2.5.2 Losses in solar cell operation

In reality, a solar cell can go under different losses before and after light absorption, reducing efficiency.

Solar cells experience optical losses, such as reflection losses, in which part of the incident light is reflected off the surface, and transmission losses, where a part of the light is absorbed by components other than the light-harvesting material. Solar cells also face internal losses when photo-generated charge carriers are not effectively separated or collected [27].

Resistive losses, such as shunt resistance (R_{sh}) and series resistance (R_s) (shown in Figure 2.7 b), influence the device's performance. The shunt resistance represents the current leakage pathways, while series resistance demonstrates resistance within the solar cell and its contacts. Low shunt resistance reduces V_{oc}, and high series resistance limits J_{sc}. The impact of these

resistances can be seen on the J-V curve where R_{sh} and R_s reduce the curve slope near V_{oc} and J_{sc}, respectively, and mainly reduce the fill factor [26].

During optical absorption, an exciton –an electron-hole pair– is generated by promoting an electron from VBM to CBM. However, the electron in the CB is in the metastable state and will eventually be stabilized in the valence band. This reverse phenomenon, known as recombination, is one of the limiting factors in solar cell operation. It annihilates the electron-hole pair and releases energy as either a photon (radiative recombination) or phonon (non-radiative recombination). Radiative recombination is a spontaneous emission where an electron from CBM recombines with a hole from VBM, releasing a photon. This recombination is dominant in direct band gap semiconductors such as GaAs. Non-radiative recombination happens when the energy is dissipated as heat in the reaction with phonon. This can occur via defect states –Shockley-Read-Hall (SRH) Recombination– or through interactions involving other charge carriers, as in Auger recombination. Trap states, caused by impurities or structural imperfections within the band gap, play a crucial role in SRH recombination. In this process, an electron is captured by a trap state before relaxing to the VBM, releasing energy as heat. In Auger recombination, the recombination energy is transferred to another electron (or hole), exciting it to a higher energy state within the conduction (or valence) band. The excited carrier then quickly loses energy as heat during relaxation [28].

2.5.3 Quantum Efficiency

Quantum efficiency (QE) is another essential parameter that quantifies the capability of a solar cell to convert incident photons into charge carriers. It gives insight into how light absorption, charge generation, and collection processes within the solar cell are effective. Quantum efficiency is usually presented as a function of the wavelength of the incident light by providing a detailed spectral response of the device. There are two different types of quantum efficiency: internal quantum efficiency (IQE) and external quantum efficiency (EQE). IQE is defined as the ratio of the number of collected electrons to the number of absorbed photons. Meanwhile, EQE is the ratio of the number of collected electrons to the number of incident photons at a specific wavelength. By accounting for all photons, including those that are not absorbed, EQE provides information about the losses within the device at a given wavelength [8].

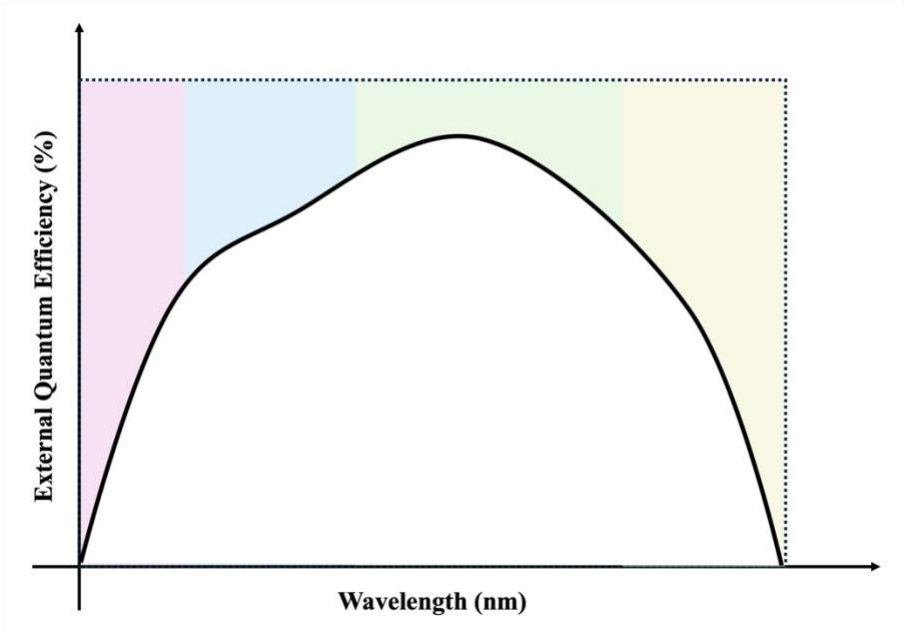

Figure 2.8 Typical EQE response of a solar cell.

Figure 2.8 illustrates a typical EQE curve of a solar cell. The EQE of an ideal solar cell is unity (100%) and square-shaped– any deviation from the ideal value indicates losses within the device. At shorter wavelengths, shown in purple square, the loss refers to light absorption by the front contact, so the carrier will not reach the junction. Another loss at these wavelengths is the parasitic absorption by the window layer, highlighted in the blue region. At longer wavelengths, the EQE increases as the probability of the light absorption by the harvester material enhances. Deviations from unity in this wavelength region are due to the low diffusion length of photogenerated carriers. This leads to recombination loss within the bulk material before the carriers can reach the junction. The last yellow sector refers to photons with lower energy than the absorber material's band gap and the carriers' low diffusion length [26], [29].

2.6 Thin Film Solar Cell Structure

Thin-film solar cells are heterojunction-based devices comprising a substrate, two conductive contacts, p-type and n-type semiconductors. These components can be arranged in a substrate or superstrate configuration depending on the fabrication order, as shown in Figure 2.9. The light travels through the metal contact and window layer in either structure to the absorber layer. Hence, both layers should be as transparent as possible to maximize light transmission and absorption. A transparent conducting oxide (TCO) is a suitable choice for forming the

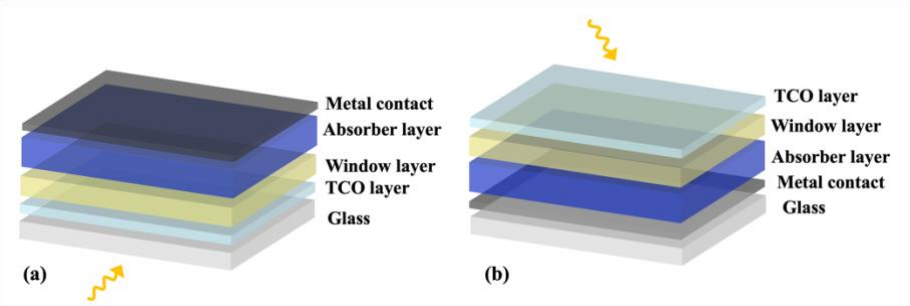

Figure 2.9 (a) substrate and (b) superstrate configurations of thin-film solar cells.

ohmic contact with the window layer, as it combines high optical transparency with excellent electrical conductivity. The n-type material (window layer) is in contact with TCO and, from the other side, in contact with the p-type (absorber layer) material to form a p-n junction. Also, another ohmic contact between p-type and metal contact facilitates the charge collection at the external circuit.

This stacking in substrate and superstrate configurations has benefits and drawbacks originating from material and substrate properties and intended solar cell applications. For instance, substrate configuration is well-suited for lightweight and flexible solar cells as the absorber grows directly on the metal contact. However, a flexible substrate limits the growth temperature, which is not a concern in superstrate structure. Additionally, optical optimization can be achieved more easily in superstrate configuration by using a TCO-coated glass substrate. Choosing between substrate and superstrate structure is making a balance between long-term stability, material compatibility, and specific solar cell application.

Chapter Three

Antimony Selenide

The potential of Sb_2Se_3 as a light-absorbing material for thin film solar cells was first demonstrated in 2014, with an initial power conversion efficiency (PCE) of 2.26% [30]. Since then, the efficiency has grown remarkably, reaching a value of over 10% in a decade [31], [32]. Despite the advancements, many fundamental aspects of Sb_2Se_3's behavior in photovoltaic devices remain unsolved. Notably, the similarities between Sb_2Se_3 and CdTe make it possible to leverage well-established CdTe technologies to advance the development of Sb_2Se_3 solar cells. The following sections discuss the material properties of Sb_2Se_3 and trace the development history of Sb_2Se_3-based solar cells, mentioning the relevant milestones and challenges.

3.1 Sb_2Se_3 Properties

A light harvester semiconductor material in a solar cell must have proper optoelectronic properties. The material should possess a suitable band gap with a high absorption coefficient, allowing for effective optical absorption and charge generation. Additionally, it should have decent electrical conductivity, high carrier mobility, and a long charge carrier diffusion length to ensure charges are transported effectively before they recombine.

Sb_2Se_3 properties make it a promising material for photovoltaic applications. A low melting point (855K) of Sb_2Se_3 allows high-quality thin film growth by low-temperature vacuum-based deposition techniques [33], which is important to scale up the technology. It exhibits a band gap between 1–1.2 eV, a high absorption coefficient ($>10^5$ cm^{-1}) [34], and good charge-carrier transport properties [35]. Additionally, it is a stable material made of earth-abundant and low-toxicity elements [36].

The following sections describe the structural and optical properties of Sb_2Se_3 in more detail.

3.1.1 Structural Properties

Sb_2Se_3 is a semiconductor from V_2-VI_3 inorganic compounds belonging to an isostructural family such as Sb_2Se_3. It crystallizes in an orthorhombic structure and adopts the Pbnm group with lattice parameters of a = 11.7938, b = 3.9858, and c = 11.6478 Å. The structure comprises one-dimensional chains of $(Sb_4Se_6)_n$ units aligned along the c-axis (as shown in Figure 3.1). Within these chains, Sb and Se atoms are covalently bonded, while the chains themselves are held together by weak van der Waals interactions between Se atoms. The stereochemically active Sb s-orbital lone pair induces asymmetric bonding, influencing the structure and resulting in this quasi-one-dimensional (Q-1D) structure. This unique geometry results in anisotropic carrier transport along [001] direction. Moreover, the Q-1D structure aligns the grain boundaries parallel to the ribbons, leading to benign charge recombination at the grain boundaries [37], [38].

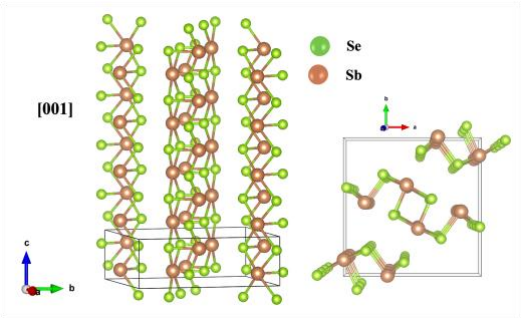

Figure 3.1 Crystal structure of Sb_2Se_3 [118].

3.1.2 Optoelectronic Properties

The photovoltaic effect is the generation of charge carriers by light absorption. Thus, the band gap –the energy of photons– and absorption coefficient –absorption capability– of the material are essential for designing a solar cell. Polycrystalline Sb_2Se_3 exhibits an indirect band gap of 1.03±0.01 eV and a direct band gap of 1.17±0.02 eV at room temperature. An indirect transition requires a phonon to conserve momentum, which makes the transition less probable than a direct case. The lone pair s-orbital of the Sb_2Se_3 structure causes its indirect band gap, yet it

demonstrates a remarkably high absorption coefficient (>10^{-5} cm^{-1}). The reason originates from a relatively low (0.14 eV) difference between the direct and indirect band gaps. This low difference enables efficient direct transitions at photon energy slightly higher than the indirect band gap, making Sb_2Se_3 a semi-direct band gap light absorber [34].

This high absorption coefficient allows for decreasing the thickness of the Sb_2Se_3 film. Chen et al. [34] demonstrated that 400 nm thick Sb_2Se_3 film absorbs all photons with wavelengths below 800 nm, while a micron thick film is sufficient to capture longer wavelengths.

3.1.3 Defects

Defects are an inherent feature of crystalline materials that affects the semiconductors' electronic properties. These imperfections can take the form of missing or misplaced atoms, unintended impurities, or grain boundaries, and they are categorized as point defects (0D), line defects (1D), planar defects (2D), or bulk defects (3D). While some defects are benign or even helpful in tailoring the semiconductor properties, many are detrimental, especially in photovoltaic applications. These defects may serve as traps or recombination centers for charge carriers in solar cells, undermining the crucial processes of photon absorption, charge separation, and collection [28].

Defects in semiconductors are broadly classified as *shallow* and *deep*, depending on their energy level positions within the band gap. Shallow defects introduce states close to the CBM or VBM, often serving as acceptors or donors, allowing carriers to escape by thermal activation. Deep defects, in contrast, have energy levels far from the band edges and act as nonradiative recombination centers, reducing carrier lifetime and mobility [39].

The polycrystalline nature of the absorber layer in thin film solar cells highlights the effects of the defects. Interfacial regions of heterojunction and grain boundaries form various defects depending on the material's composition, crystallographic structure, and fabrication process.

The intrinsic defects of Sb_2Se_3 include two vacancies (V_{se}, V_{sb}) where an atom is missing from its lattice site; two interstitials (Sb_i, Se_i) where an atom is located away from its expected lattice position; and two antisite defects (Sb_{Se}, Se_{Sb}) where one atom replaces another at its lattice site. However, the low symmetry Q-1D structure of Sb_2Se_3 introduces complex defects in non-

equivalent atomic sites within the ribbons. For instance, Sb and Se atoms occupy two (Sb_1, Sb_2) and three (Se_1, Se_2, Se_3) distinct positions, respectively [39], [40], [41].

The defect formation is dependent on the stoichiometric environment during growth. Experimental [31], [32], [33], [42] and computational [43] studies have shown that Se-rich conditions favor acceptor-like defects, such as $Se_{Sb,}$ contributing to p-type conductivity. In contrast, Se-poor conditions promote the formation of donor-like defects, such as V_{Se}, leading to n-type behavior. Accordingly, Se-rich Sb_2Se_3 film improves carrier lifetime and reduces recombination, while Se-poor film traps carriers and degrades device performance, leading to V_{oc} deficit.

3.2 Sb_2Se_3 thin film solar cell development

As mentioned in Section 2.6, thin film solar cells are made in two different configurations, considering the material properties and device applications. Sb_2Se_3 thin film solar cells have also been fabricated in both configurations, and the highest efficiency is reported for a substrate device structure. Various approaches have been applied to these solar cells, improving their efficiency. The following sections explain some of the advancements in each part of the device. A summary of developed devices is also tabulated in Table 1.

3.2.1 Growth Methods

The anisotropic carrier transport properties of Sb_2Se_3 have garnered notable interest due to their potential to mitigate grain boundary recombination. Developing an efficient solar cell requires the preparation of a high-quality thin film to minimize recombination losses caused by defects. Controlling the ribbon's orientation is crucial in a Q-1D material such as Sb_2Se_3. Therefore, optimizing growth parameters can effectively improve charge transport in Sb_2Se_3. Various physical vapor deposition and chemical methods have been investigated to grow Sb_2Se_3 thin films. Notable methods include thermal evaporation [44], [45], rapid thermal evaporation (RTE) [46],[47] closed–space sublimation (CSS) [48], vapor transport deposition (VTD) [49], pulsed laser deposition (PED) [50], magnetron sputtering [51], and chemical bath deposition (CBD) [52].

For the first time in 2014, Zhuo et al. prepared Sb_2Se_3 thin film by spin coating with a hydrazine-based solution and applied it to a superstrate device structure using TiO_2 heterojunction. Despite ribbon orientation mostly along (hk0) planes, the device showed a 2.26% efficiency (V_{oc} = 520 mV), highlighting Sb_2Se_3 as a promising material for photovoltaic applications [30].

The same group deposited Sb_2Se_3 using thermal evaporation in the superstrate device structure on the CdS buffer layer. The device showed 1.9% efficiency and a lower V_{oc} of 300 mV compared to the previous study. Their results suggested that TiO_2 forms a favorable band alignment with Sb_2Se_3 while lower CB in CdS leads to a deeper Fermi level, limiting the V_{oc} [53]. In the same year, Liu et al. successfully applied thermally evaporated Sb_2Se_3 to a substrate device structure. They analyzed the thermal stability of Sb_2Se_3, revealing that Sb_2Se_3 begins to lose weight at 423°C, with a significant increase at its melting point. This indicated that the substrate temperature during deposition should not exceed 423°C to prevent re-evaporation of the material [44].

RTE was considered an efficient growth method for producing high-quality films due to antimony selenide's low melting point. During RTE, the substrate and material source are positioned close (<10 mm), so the deposition can occur rapidly within tens of seconds. Zhou et al. reported a well-originated Sb_2Se_3 film along (hk1) planes using the RTE method. The results were promising, J_{sc} = 25.14 mA/cm^2, V_{oc} = 400 mV, FF = 55.7%, and efficiency = 5.6%. Meanwhile, their computational study showed that the recombination loss is minimal if Sb_2Se_3 grows along (001) planes [54].

CSS is a widely used technique to grow semiconductors, especially CdTe. Similar to RTE, CSS features a close source–to–substrate distance but operates in a well-controlled pressure environment where the material can directly sublimate from solid to gas (as it comes with the name). Thus, these conditions enable deposition at high substrate temperatures, resulting in higher-quality thin films, making CSS well-suited for scaling up to industrial applications. Leveraging similarities between Sb_2Se_3 and CdTe, Hutter et al. fabricated Sb_2Se_3 thin film solar cells using CSS. The device achieved comparable parameters to Sb_2Se_3 solar cell by RTE, J_{sc} = 33.4 mA/cm^2, V_{oc} = 420 mV, FF = 43.2%, and efficiency = 6.06% [48].

In RTE and CSS, the deposition occurs rapidly within a short source–to–substrate distance that could lead to defect formation. VTD involves transporting the vaporized material toward the substrate using a carrier gas. The key growth parameters controlling the thin film quality include source–to–substrate distance, source and substrate temperature, and partial pressure of the gas. Wen et al. grew a high-quality Sb_2Se_3 thin film using VTD by carefully optimizing the growth parameters. Therefore, they improved the crystallinity and suppressed bulk and interfacial defects, resulting in a high-performance device of 7.6% (V_{oc} = 488 mV) [55].

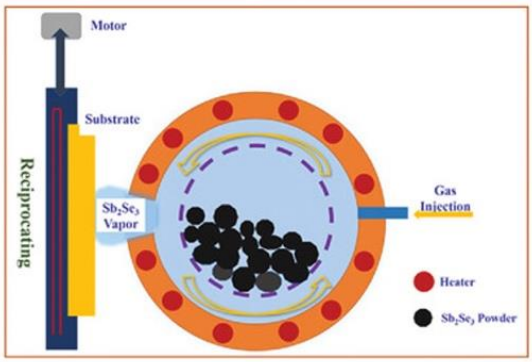

Figure 3.2 The schematic of the injected vapor deposition method [30].

Regardless of the introduction of different deposition techniques, Sb_2Se_3 solar cells still suffer from V_{oc} deficit, which originates from mid-gap defects. Growing in Se-rich conditions is known as a strategy to minimize the formation of these detrimental defects. Considering this fact, Duan et al. developed an innovative injected vapor deposition (IVD) that achieved the highest efficiency reported by a physical growth method. The schematic is shown in Figure 3.2; the system consists of two parts: the substrate that can move up and down and a roller covered with the heater that contains a break to spray the vapor. Here, a mixture of Se pellets and Sb_2Se_3 powder was placed in the roller, and the vapor was injected using a carrier gas, Ar. Through this method, they grew well-originated Sb_2Se_3 film, suppressing deep defects that resulted in a high efficiency of 10.12% (V_{oc} = 488 mV) [31].

The record efficiency of the Sb_2Se_3 thin film solar cell was reported as 10.57% in 2022 by Zhao et al. They introduced an additive-assisted chemical bath deposition method to grow Sb_2Se_3, aiming to improve the film quality. In principle, this technology is designed to control and adjust the film properties thoroughly by introducing additives. They employed thiourea (CH_4N_2S) and selenourea (CH_4N_2Se) to regulate the growth, improving both the crystallinity and morphology of the film, especially using selenourea. They concluded that this method

enhanced charge separation and collection efficiency while suppressing non-radiative recombination. As a result, the device achieved a high J_{sc} of 33.52 mA/cm^2, which contributed to the high efficiency [32].

3.2.2 Window Layer

The window layer, also known as the electron transport layer (ETL), is the n-type material that forms the p-n heterojunction with Sb_2Se_3. This layer should have a wide band gap to transmit the light to the absorber and form proper band alignment to navigate carriers efficiently. In heterojunction, where two materials with different lattice constants come together, the lattice mismatch leads to defects formation [56]. To mitigate these interfacial defects, the lattice mismatch of the materials must be minimized.

Moreover, two types of band alignments can form at a heterojunction: *spike-like* and *cliff-like*, as shown in Figure 3.3. When the CBM of the window layer is higher than that of the absorber layer, a spike-like alignment forms, creating a barrier for photogenerated carriers. In contrast, a cliff-like interface forms when the CBM of the window layer is lower than that of the absorber layer. The barrier in spike-like alignment can suppress recombination caused by mid-gap states, while cliff-like assists trapping carriers, lowering the V_{oc}. As a result, the spike-like offset is more favorable, but a barrier that is too high leads to a J_{sc} deficit [57].

CdS is the most used window layer in Sb_2Se_3 thin film solar cells, and many studies have reported CdS-based devices. CdS is also employed in other thin film solar cells such as CdTe, CIGS, and CZTS and can be prepared easily by chemical bath deposition (CBD) or PVD methods. However, drawbacks of CdS as the n-type partner for Sb_2Se_3 include high lattice

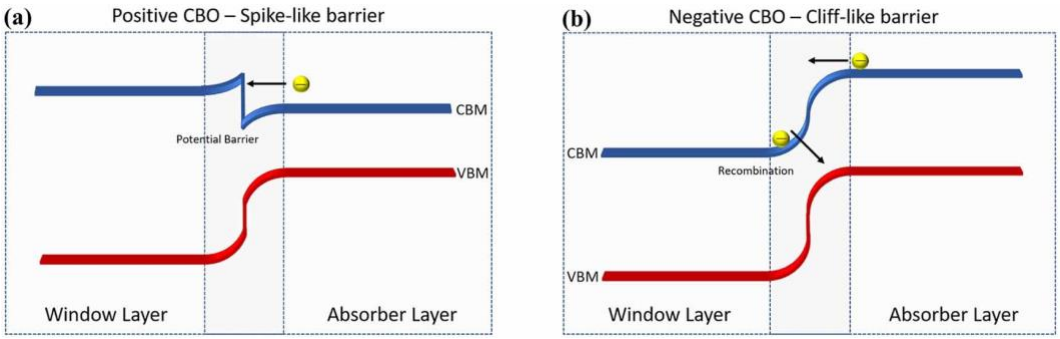

Figure 3.3 The illustration of (a) spike-like (positive conduction band offset) and (b) cliff-like (negative conduction band offset) band alignment in heterojunction [57].

mismatch (>10%) [58], [59], parasitic absorption due to a narrow band gap (2.4 eV), and Cd diffusion into the absorber layer [60]. Also, the conduction band offset between CdS and Sb_2Se_3 has been reported to be both cliff-like and spike-like, depending on the device structure and fabrication conditions [61], [62].

To overcome these challenges, strategies such as oxygenating the film to tune the band gap [63], [64], [65] and applying CdS nanorods to stimulate [hk1] growth [66] resulted in improved device performance. Additionally, applying $CdCl_2$ treatment was reported to be efficient in suppressing interfacial defects [67], and Zn-doping transferred a cliff-like band alignment to a spike-like band offset [68].

Concerns over Cd toxicity and parasitic absorption of CdS have driven the development of Cd-free wide band gap materials such as TiO_2, SnO_2, and ZnO with lattice parameters compatible with Sb_2Se_3 film.

TiO_2 can be an excellent choice for the window layer due to its chemical stability and wide band gap (3.2 eV). This buffer layer has been deposited using chemical processing and physical evaporation techniques.

The first planner Sb_2Se_3 solar cell was fabricated with a TiO_2 junction and reported a relatively high V_{oc} of 520 mV [30]. The conduction band offset of the TiO_2/Sb_2Se_3 junction was reported as flat without any transition layer [69] and cliff-like [70]. However, $TiCl_4$ treatment benefited band alignment between TiO_2 and Sb_2Se_3 and stimulated [001] ribbon growth [71]. Recent progress on TiO_2 ETLs has underlined that the phase and deposition method play an important role in the device's performance. Don et al. demonstrated that mixed-phase TiO_2 films deposited via sputtering yielded severe interfacial charge barriers and, thus, J-V distortions and performance variability. Their work highlighted that anatase-phase TiO_2 exhibits superior band alignment and charge transport properties. Further building on this, they later optimized the reactive DC sputtering technique for highly crystalline anatase TiO_2 films. This method avoided the phase inconsistency of earlier deposition techniques. It demonstrated a high efficiency of 8.12%, highlighting the potential of sputtering as an industrially viable technique that could be scaled up for cadmium-free solar cells [72], [73].

ZnO is also a non-toxic, wide band gap alternative window layer that has been applied using methods such as spray pyrolysis [46] and magnetron sputtering [74]. The CBO between ZnO and Sb_2Se_3 has been found to be cliff-like [69]. Annealing ZnO films in different ambientes

such as air and vacuum tuned its optoelectronic properties. In particular, air-annealing reduced oxygen vacancies, thus improving heterojunction quality and increasing efficiency, illustrating the ZnO defect impact on device performance [74]. Wang et al. studied the influence of ZnO crystal orientation on Sb_2Se_3 growth in a superstrate configuration. They found that randomly oriented ZnO induced the formation of (221) ribbons in Sb_2Se_3 films, resulting in a device efficiency of 6% [46].

SnO_2 is a highly transparent and stable material with a high n-type doping density and deep conduction and valence band offsets. The SnO_2/Sb_2Se_3 heterojunction exhibited a spike-like band alignment, and Zhong et al. demonstrated that the carrier dynamics at this heterojunction suppress the recombination rate of deep defects [75]. Despite this suitable junction, the reported efficiency of SnO_2-based solar cells has remained relatively low. Recently, Luo et al. investigated the impact of post-annealing SnO_2 films –grown by the ALD method– in a substrate device structure. They concluded that annealing improved the SnO_2 film quality and carrier lifetime, resulting in a spike-like heterojunction and effective passivation of bulk defects. This advancement achieved a performance of 7.39%, comparable to other Cd-free-based devices [76].

3.2.3 Back contact and hole transport material

Introducing a hole transport material (HTM) between the back contact and Sb_2Se_3 can improve charge extraction by reducing the resistance of the back contact. Various organic and inorganic materials have been investigated, such as 4,4′,4″,4‴-(9-octylcarbazole-1,3,6,8-tetrayl)tetrakis(N,N-bis(4-methoxyphenyl)aniline)(CZ-TA), poly(3-hexylthiophene) (P3HT), 9′ -spirobifluorene (spiro-OMeTAD) [77], PbS quantum dot [78], and NiO_x [79].
Chen et al. introduced PbS colloidal quantum dots to structure p-i-n Sb_2Se_3 solar cells, resulting in an efficiency of 6.5%. They concluded that the layer reduced the recombination at the back contact and enhanced the carrier collection [78]. Another study investigated the impact of CZ-TA and spiro-OMeTAD hole transport layers, leading to improved carrier collection near the back contact. The JV and EQE results of this study are shown in Figure 3.4, and the device with CZ-TA HTL achieved an efficiency of 6.84% [77]. Recently, Shalvey et al. [80] compared three HTMs–P3HT, PCDTBT, and spiro-OMeTAD– to evaluate their effectiveness in mitigating pinhole blocking and optimizing energy band alignment at the back contact of

Sb_2Se_3 solar cells. These HTMs separated physically Sb_2Se_3 and back contact, leading to a less defective junction. Also, the HTM lowered the Schottky barrier at the back contact, eliminating the rollover effect of J-V curve devices without HTMs. Sb_2Se_3 solar cells with a P3HT layer showed 7.44% efficiency.

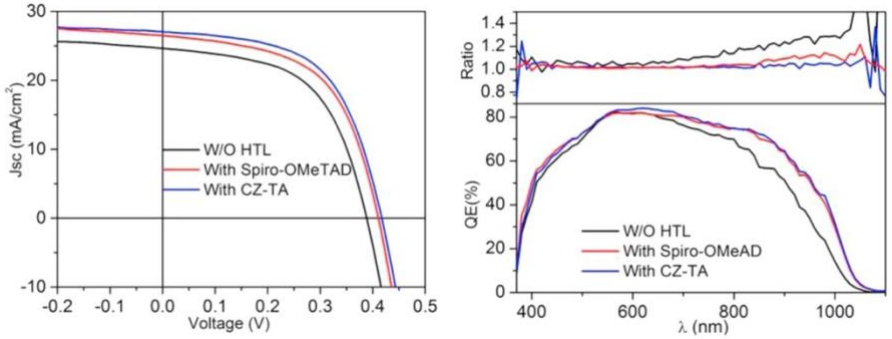

Figure 3.4 J-V and EQE results of Sb_2Se_3 solar cells with and without HTMs [77].

3.3 Summary

Sb_2Se_3 thin-film solar cells with efficiencies above 10% showed high J_{sc} values, proving efficient carrier collection. However, the V_{oc} deficit has remained a bottleneck even for these devices, illustrating relatively low V_{oc} values of 488 and 467 mV [32], [31].

In the research of this emerging chalcogenide material, Cd-based and Cd-free window layers have been used, while the CdS-based junction showed better performance. nevertheless, transparent ETLs have shown promising application in Sb_2Se_3 solar cells, leaving room for further optimization and deeper studies to raise the performance of Cd-free-based devices. according to the literature, the creation of selenium-rich conditions improves the quality of thin films, both in vacuum-based or chemical processing methods. However, a better understanding of the conditions that promote columnar growth of Sb_2Se_3 may accelerate the development of high-efficiency devices.

The critical issue of V_{oc} deficit urges a comprehensive study of material defects. Understanding the nature of defects guides us in identifying solutions that lead to high-performance solar cells. Finally, further device optimization to address challenges at the back contact or mitigate shunt paths will help improve these solar cells' overall performance.

Table 3.1 Summary of notable publications on Sb_2Se_3 thin film solar cells over the last decade.

Window layer	Configuration	Results	Growth method	Efficiency	Year/Ref
TiO_2	Superstrate	First Sb_2Se_3 thin film-based solar cell	Spin coating	2.26%	2014/[30]
CdS	Substrate	Fabrication substrate device based on vacuum deposition method	TE	2.1%	2014/[44]
ZnO	Superstrate	Influence of plane's orientation on device performance	RTE	5.6%	2015/[47]
TiO_2	Superstrate	Appling CSS for the first time	CSS	6.06%	2018/[48]
CdS	Superstrate	Studying defects in Sb_2Se_3	VTD	7.6%	2018/[55]
TiO_2/CdS	Substrate	Growing nanrod of Sb_2Se_3 along (001)	CSS	9.2%	2019/[81]
CdS	Substrate	Improved V_{oc} via selenization	sputtering	6.84%	2020/[82]
CdS	Substrate	Growth condition design	IVD	10.2%	2022/[31]
CdS	Superstrate	Novel additive-assisted CBD synthetize of Sb_2Se_3	CBD	10.57%	2022/[32]
TiO_2	Superstrate	Optimization of TiO_2 layer	CSS	8.12%	2024/[72]

Chapter Four

Methods

This chapter outlines the principles of the experimental methods used throughout this thesis. It covers the fabrication techniques for growing thin films, as well as material and device characterization methods.

4.1 Thin Film Fabrication

These sections briefly introduce the growth methods utilized for preparing thin films in this thesis.

4.1.1 Thermal Evaporation

Physical vapor deposition (PVD) is an atomistic deposition process that grows thin films. In PVD processes, the vapor of atoms or molecules from a solid or liquid source of a material is transported through a vacuum or gaseous environment to the substrate, where it condenses. PVD processes can deposit films with various thicknesses, from a few nanometers to several micrometers, on substrates of different shapes and sizes for various applications. Thermal evaporation (TE) or vacuum evaporation is a PVD process in which material vapor from a solid source travel to the substrate with little or no collision through a vacuum environment. Among many different vacuum evaporation techniques, thermal evaporation is the simplest and most widely utilized to grow thin films. Source temperature, substrate temperature, distance between source and substrate, and evaporation rate control the film growth. Figure 4.1 illustrates a typical thermal evaporation system that requires three components: a vacuum chamber, a heating source, and a film thickness control. A high vacuum environment ranging from 10^{-5} to 10^{-9} torr increases the free path of atoms, minimizing the collision of atoms and gas molecules.

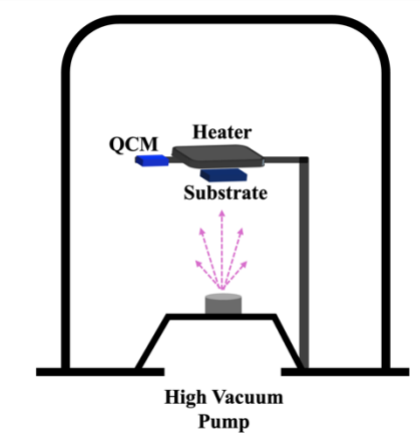

Figure 4.1 Schematic from a typical thermal evaporation system.

The source material is placed in a crucible or on a boat of a resistive element and is heated to the desired evaporation temperature. Resistive heating provides the necessary heat by passing current through a high-temperature resistant material, like tungsten. A quartz crystal microbalance (QCM) measures changes in frequency correlating to the mass of the deposited material and monitors film thickness precisely. The substrate can be heated by a heating source like a resistive heater to help crystallize the film during the deposition [83].

In this study, Sb_2Se_3 is prepared by heating a graphite crucible, while a QCM controls the deposition rate and film thickness. The chamber pressure is maintained at 3×10^{-6} mbar, and the deposition rate is kept at 15 nm/sec to avoid the decomposition of Sb_2Se_3 during film growth. Finally, our system's source–to–substrate distance is about 15 cm.

4.1.2 Atomic Layer Deposition

Another approach to growing thin films is chemical vapor deposition (CVD). This method forms a film through chemical reactions occurring in the vapor phase of the material either near or directly on a heated substrate. During CVD, reactant gases enter the reactor by forced flow and interact with the substrate's surface, where deposition occurs. Finally, by-product gases are purged away from the system.

Atomic layer deposition (ALD) is a special highly-controlled CVD method to achieve film growth with excellent conformality, uniformity, and thickness control. Unlike conventional CVD, in ALD deposition, each precursor enters separately and saturates the surface, and the next precursor enters after chamber evacuation. This process results in the film growth taking

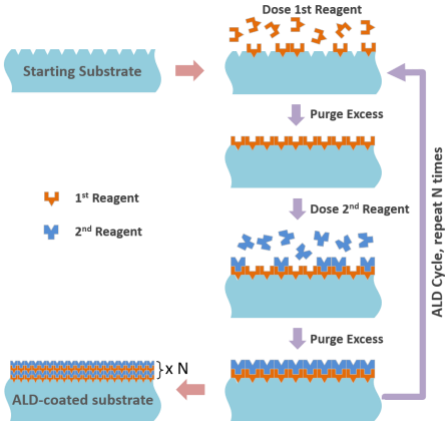

Figure 4.2 Schematic of reaction in ALD deposition [119].

place in a cyclic manner, and the cycle will be repeated as many times as needed to obtain the desired thickness. In ALD, each cycle deposits 0.1 to 3 Å film thickness –depending on the process– so the growth rate is lower than conventional CVD methods. The unique feature of ALD is a self-limiting reaction, allowing the precise fabrication of ultrathin and uniform films. This feature arises because each precursor reacts only with available surface sites, ensuring that the reaction stops once a monolayer is formed. This "saturation" of the surface prevents uncontrolled growth and thickness variations, enabling the precise fabrication of ultrathin and uniform films [84].

In this work, SnO_2 was grown by ALD and applied as a Cd-free window layer for Sb_2Se_3 solar cells. The deposition was performed at a substrate temperature of 100°C and a base pressure of 0.4 mbar with argon as the carrier gas. Tetrakis(dimethylamino)tin(IV) (TDMASn) and H_2O were used as precursors. During the deposition TDMASn as tin precursor was kept at a temperature of 75°C while H_2O was unheated. The chemical reactions in this process have been calculated by Density Functional Theory and given as follows [85]:

$$(OH)_2^* + Sn(DMA)_4 \rightarrow O_2Sn(DMA)_2^* + 2HDMA^{\uparrow}$$

$$O_2Sn(DMA)_2^* + 2H_2O \rightarrow (OH)_2^* + SnO_2 + 2HDMA^{\uparrow}$$

In these equations * refers to surface species and ↑ is the evolution of the gaseous products.

4.1.3 Chemical Bath Deposition

Chemical bath deposition is a method that produces a film by immersing a substrate in a precursor solution. The solution temperature, pH, and reagents concentration control the reaction kinetics. The experimental setup includes a container, sample holder, magnetic bar, and thermometer, as shown in Figure 4.3. To deposit metal chalcogenide using CBD, the solution comprises metal salt (the cation precursor) and a chalcogenide source (the anion precursor). Also, a complexing agent can be added to slow down the reaction or to supply ligands for the metal ion. When the temperature of the solution increases, the cations and anions are gradually generated. These ions then combine on the substrate through a nucleation process, resulting in film growth via an ion-by-ion condensation process. It possesses a simple, economical experimental setup that is efficient for large-scale depositions. Also, various metal chalcogenides can be grown by CBD at low temperatures on various substrates [86].

Cadmium sulfide was grown by CBD as a buffer layer in this study. The chemical bath was prepared by adding 15 ml of cadmium acetate and 32 ml of ammonia (20 %) to 200 ml of deionized water at a temperature of 60°C. After 10 minutes of keeping the sample inside this solution, 10 ml of thiourea was added. The deposition time was optimized to 16 minutes to achieve the desired film quality. After deposition, the sample was rinsed with deionized water and then sonicated in isopropyl alcohol for one minute to clean it and remove any residual contaminants.

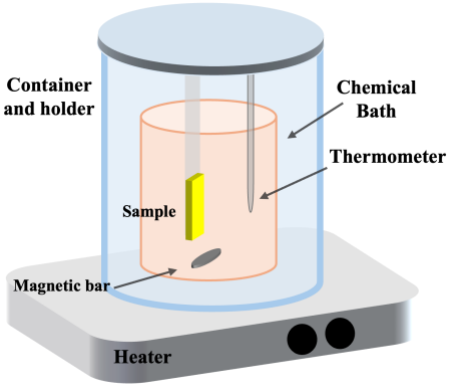

Figure 4.3 Schematic of a typical CBD setup.

4.2 Thin Film Characterization

This thesis used X-ray diffraction (XRD), Raman spectroscopy, atomic force microscopy (AFM), scanning electron microscopy (SEM), and secondary ion mass spectroscopy (SIMS) to analyze thin film properties.

4.2.1 X-ray Diffraction

XRD is a widely used fundamental technique to determine the structural properties of materials, especially those with crystalline phases. It provides versatile, non-destructive analysis, accurately identifying crystal structures, phase composition, crystallite sizes, and strain distributions [26].

XRD is based on the interaction between X-rays and atoms inside the crystalline material. When X-rays with wavelengths comparable to interatomic distance strike the sample at specific angles, it will undergo elastic scattering from atoms. This scattering results in constructive interference at certain angles, leading to diffraction patterns described by Bragg's law:

$$n\lambda = 2d\sin\theta$$

Here, n is an integer, λ is the wavelength of the incident X-rays, d is the interplanar spacing, and θ is the diffraction angle. The visualization of X-ray diffraction is shown in Figure 4.4.

This diffraction is a fingerprint of a crystalline material that provides information about the material's orientation, texture, and degree of crystallinity. Since the semiconductor's structure strongly affects the performance of solar cells, XRD plays a key role in characterizing thin

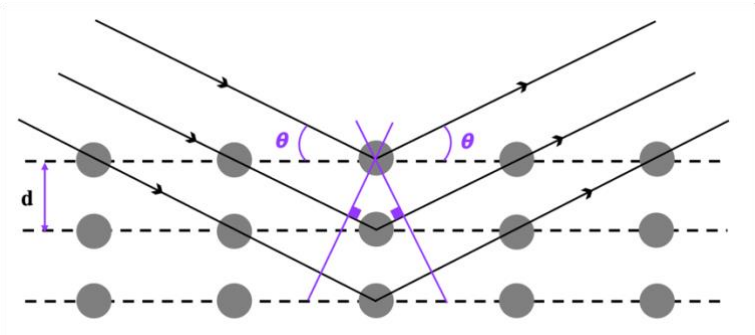

Figure 4.4 A visualization from Bragg's law

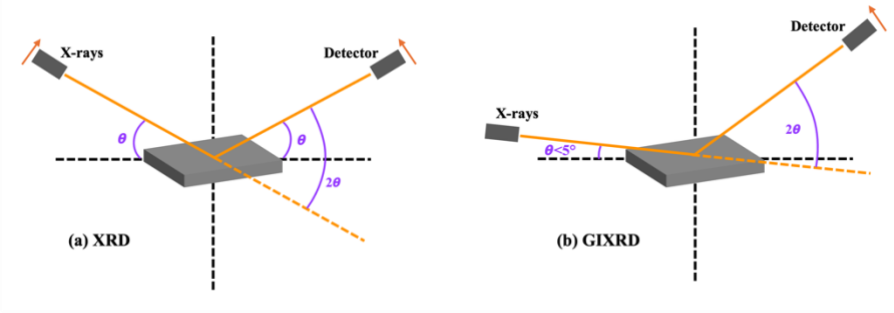

Figure 4.5 (a) XRD and (b) GIXRD techniques geometries.

films. Analyzing ultra-thin films can be challenging by XRD as its deep penetration depth can effectively provide information about bulk material. Grazing-incident X-ray diffraction (GIXRD) is a specialized measurement that analyzes near-surface crystal structures.

In standard XRD, the X-ray source and detector move symmetrically, providing diffraction from the whole volume of the sample. In GIXRD, however, the X-ray angle is set at a shallow value, between 0.5° to 1°, and the detector collects the diffraction at various angles (2θ). Therefore, the X-ray's penetration depth is reduced, making GIXRD sensitive to the surface and suitable for thin film analysis [87]. Figure 4.5 illustrates the difference between XRD and GIXRD setups.

As the crystal orientation of Sb_2Se_3 strongly influences the charge transportation, hence, identifying the preferred orientations is critical in fabricating high-performance Sb_2Se_3 solar cells. Also, in this thesis, Sb_2Se_3 has been applied with a thickness of less than 1μm, highlighting the role of GIXRD in the accurate detection of crystal patterns.

4.2.2 Secondary Ion Mass Spectroscopy (SIMS)

Secondary ion mass spectroscopy (SIMS) is an effective technique for investigating the composition profile of the materials. In this process, the sample's surface is bombarded by primary ions in a high vacuum environment, generating sputtered ions from the material in analysis. These secondary ions are then directed by an electric field to the detector to be analyzed using a mass spectrometer to determine their mass-to-charge ratio. The mass spectrometer, including time-of-flight (TOF), magnetic sector, or quadrupole mass spectrometers, measures the ion's kinetic energy to determine its mass-to-charge ratio.

In the TOF approach, the ratio is calculated by the velocity of ions, while the other methods analyze the sputtered ions at different depths. Accordingly, TOF-SIMS has a higher resolution than SIMS and is suitable for surface analysis and the detection of molecular species [88].

Generally, in thin film solar cell fabrication, SIMS is widely employed to detect impurities, analyze the composition, and study interdiffusion at heterojunctions. In Sb_2Se_3 any deviation from the stoichiometric Sb:Se ratio results in defect formation, emphasizing study of elemental distribution. SIMS profiling enables precise analysis of elements distribution and interfacial diffusion, providing essential insights for optimizing the efficiency and stability of Sb_2Se_3 solar cells.

4.3 Device Characterization

To evaluate solar cell performance, carrier collection, and charge carrier dynamics, current-voltage (I-V), external quantum efficiency (EQE), and capacitance spectroscopy have been performed.

4.3.1 Current – Voltage Measurement

I-V measurement is a fundamental technique that determines the efficiency and other photovoltaic parameters of a solar cell, as the I-V curve was explained in Section 2.5.1. This technique measures the current response of the device over a range of applied voltage, typically from -1 V to 1 V. The measurement can be performed under dark conditions to examine the rectifying behavior of the p-n junction or under standard illuminated conditions AM 1.5. AM stands for air mass, light undergoes a reduction in its power by passing through the atmosphere, and air mass quantifies this reduction. AM 1.5 is a simulated standard solar irradiance at ground level that allows accurate comparison of globally measured devices. During the measurement, the front and back contacts of the solar cell are electrically connected to a source meter. At the end understanding the provided photovoltaic parameters from J-V curve including the short-circuit current density (J_{sc}), open-circuit voltage (V_{oc}), fill factor (FF), series and shunt resistances, and power conversion efficiency (η) provide valuable insights into the operational mechanisms of the solar cell.

4.3.2 EQE

Solar cells undergo optical and recombination losses, reducing the J_{sc} value. EQE is a technique that measures the ability of a solar cell to absorb the incident light and convert it to photocurrent. As discussed in Section 2.5.3, EQE represents the ratio of collected charge carriers to incident photons at each wavelength and is typically measured across the solar spectrum. During EQE measurement, a monochromatic light source illuminates the cell, and the photocurrent generated at each wavelength is recorded. The resulting curve provides insight into the losses within the device. Also, Integration of the EQE spectrum with the AM1.5 solar spectrum allows the calculation of the J_{sc} under standard test conditions.

4.3.3 Capacitance Spectroscopy

Electronic defects strongly influence the performance of thin film solar cells. These defects consist of intrinsic defects of the polycrystalline absorber layer and interface defects under the formation of heterojunction. As the fabrication process impacts defect formation, it also offers the potential to control and mitigate their influence. Analyzing the defects helps in understanding their impact on the device's operation and can give important information for the optimization of solar cells. Capacitance spectroscopy techniques, including Capacitance-Voltage (C-V), Drive-Level Capacitance Profiling (DLCP), and Admittance Spectroscopy (AS), are advanced characterization methods to explore defects within diode-like devices.

Capacitance-Voltage Technique

Considering a solar cell as a parallel-plate capacitor where the depletion region is free of carrier allows us to explore carrier dynamics through differential capacitance. Capacitance spectroscopy analysis assumes an abrupt, one-sided junction with a depletion region that is fully depleted of free carriers.

The small charge response of a solar cell to the small change of applied voltage –an AC (fixed in frequency and amplitude) perturbation superimposed on a DC bias – is measured in C-V profiling. Therefore, capacitance variation is defined by

$$C = \frac{\partial Q}{\partial V} = \frac{\varepsilon \varepsilon_0 A}{W}$$

Where ε is the dielectric constant, ε_0 is the permittivity of free space, and A is the device area. For this junction, depletion region width (W) is

$$W = \sqrt{\frac{2\varepsilon \varepsilon_0 (V_{bi} - V_{dc})}{eN_B}}$$

Where V_{bi} is built-in voltage, V_{dc} is applied voltage, and N_B is doping concentration.
A linear response can be obtained by plotting C^{-2} against $V_{dc,}$ and the intercept will be V_{bi}. Also, a depth profile of doping density $N_B(x)$ can be derived from C(V), where $x = \varepsilon\varepsilon_0 A/C$ from the junction, and the doping concentration at the edge of the depletion region is:

$$N(W) = -\frac{2}{q\varepsilon\varepsilon_0 A^2}\left(\frac{d(1/C^2)}{dV}\right)^{-1}$$

where A is the area, q is the elementary charge and ε is the dielectric constant. The doping profile of the solar cell is obtained by plotting N_B versus depletion region width.
However, the accuracy of this technique depends on the validity of the depletion approximation, which assumes abrupt junction and depletion region free of mobile carriers. In thin films with higher defect density in the depletion region, the capacitance response to the applied voltage can be influenced by additional carrier dynamics, leading to an overestimated doping concentration.

Drive-Level Capacitance Profiling

Drive-level Capacitance Profiling (DLCP) is a specialized extension of CV profiling that is useful for detecting both shallow and deep defects. DLCP measures capacitance changes of the junction over a range of AC voltage amplitudes (drive levels). The charge response is assumed to be linear in CV profiling due to the small AC voltage applied. In contrast, in DLCP, larger AC voltages are applied, and the capacitance can be approximated as:

$$C \approx C_0 + C_1(\delta V)$$

where C_0 represents the capacitance at zero drive level, and C_1 is the first-order correction for a finite drive level. In DLCP, these parameters, C_0 and C_1, enable the calculation of gap state density:

$$N_{DL} = -\frac{C_0^3}{2e\varepsilon\ \varepsilon_0 A^2 C_1}$$

Additionally, DLCP offers a way to study deep defect densities by examining how they vary with frequency. For materials with deep traps, high-frequency DLCP provides a more accurate measurement of free-carrier density compared to traditional CV profiling. At lower frequencies, DLCP results closely match those of CV profiling because all the traps that react to the DC bias in C-V also respond to the AC bias. The difference between defect densities measured at low and high frequencies reveals the density of deep-level defects.

Admittance Spectroscopy

After identifying the densities of deep and shallow defects using CV and DLCP measurements, admittance spectroscopy (AS) plays a key role in further understanding the electrical properties of the device. This technique helps understand the recombination losses by identifying the energy depth of defect states within the band gap that affects the device's performance.

AS measures the capacitance response of the device under a small amplitude AC voltage as a function of frequency and temperature. Defects can behave differently depending on how quickly they respond to electrical signals –some react slowly (deep defects), while others respond faster (shallow defects).

This response is characterized by the emission time constant (τ), which is the average time that a charge carrier takes to escape from a defect level back into the conduction or valence band. For an electron trapped in an energy level of E_t, the emission time rate to the conduction band is given by:

$$\tau_n = \frac{1}{\sigma_n V_{th} N_c} \exp\left(\frac{E_C - E_t}{KT}\right)$$

Where σ_n is the capture cross-section of the trap, V_{th} is the thermal velocity of electrons, N_C is the effective density of states in the conduction band, $(E_C - E_t)$ is the energy difference between the conduction band edge and trap level, K is the Boltzmann constant, and T is temperature.

AS extracts the emission time constant and the energy level of the defects by sweeping the frequency and temperature. The temperature-dependent emission time follows the Arrhenius equation:

$$\tau_t = \tau_0 \exp\left(\frac{-E_a}{KT}\right)$$

Where τ_0 is the attempt-to-escape time, E_a is the activation energy of the defect, K is Boltzmann's constant, and T is the absolute temperature.

Since $f = 2\pi/\tau$ a defect can only respond if the AC frequency is slower than its emission rate. Therefore, shallow defects with a shorter emission rate contribute at higher frequencies while deep defects (longer τ) have more time to respond at low frequencies.

Performing AS over a range of temperatures and extracting the peak response frequency from the $-f_{ac}(dC/df_{ac})$. vs. f plot at each temperature allows for the construction of an Arrhenius plot of $\ln(f_t)$ versus 1/T. The slope of the plot yields the activation energy, while the intercept provides attempt-to-escape frequency, from which the capture cross-section can be estimated.

The material presented in this section (4.3.3) is primarily based on [26].

Chapter Five

Tailoring Window Layers for Sb_2Se_3 Solar Cells: CdS or CdSe?

5.1 Introduction

In superstrate configuration, the buffer layer is important not only for the charge separation and the band alignment but also for influencing the crystal structure of the absorber, so choosing a suitable buffer is even more important.

CdS is the widely used window layer in many solar cells, including Sb_2Se_3, and the highest efficiencies have been reported for CdS-based devices [31], [32]. However, alternative buffer layers have been introduced to these solar cells due to large mismatch, parasitic absorption, and elemental interdiffusion of CdS. SnO_2 [76] and TiO_2 [72] are transparent, stable materials that illustrated comparable efficiencies, about 8%.

Applying CdSe as a window layer despite its narrow band gap was promising in CdTe solar cells. It has been shown that diffusion of CdSe to CdTe leads to the formation of photoactive $CdTe_{(1-x)}Se_x$ that increases the J_{sc} [89], [90]. Guo et al. have introduced a CdSe buffer layer by RF-sputtering for Sb_2Se_3 grown by CSS, reporting an efficiency of 4.5% [91]. They showed that reducing S/Se interdiffusion to the junction improves the stability of the devices.

In this thesis, Sb_2Se_3 has been grown by thermal evaporation at a substrate temperature of 300°C. Although growing at low temperatures could minimize the element interdiffusion, prolonged deposition time may lead to Se loss that can be amplified by S diffusion to the junction. Applying CdSe can address the issue and contribute to the Se compensation in the

absorber. This study aims to compare the structural and electrical properties of Sb_2Se_3 solar cells based on CdS and CdSe window layers to identify the best-performed n-type layer.

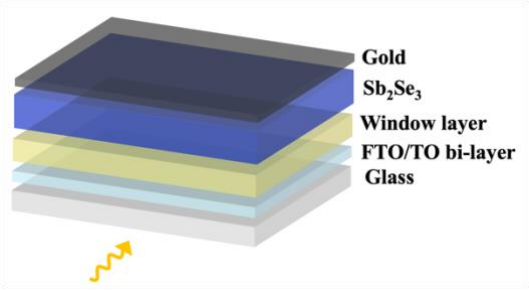

Figure 5.1 Schematic of superstrate Sb_2Se_3 solar cells

Based on our analysis, Sb_2Se_3 growth on both buffer layers shows the same crystal and morphology patterns. However, SIMS analysis reveals sulfur diffusion onto the CdS/Sb_2Se_3 junction while the selenium grad is constant at CdSe/Sb_2Se_3 junction. Also, our accelerated stability tests (AST) have demonstrated a remarkable stability of CdSe-based devices. Interestingly, introducing CdSe increased the average current density of 2 mA/cm^2 despite a narrower band gap compared to CdS.

5.2 Device Fabrication

Sb_2Se_3 solar cells are fabricated in superstrate configuration (Figure 5.1) on a commercial fluorine doped tin oxide (FTO)/tin oxide (TO) bi-layer coated soda lime glass. Subsequently, CdS is deposited by CBD, as explained in Section 4.1.3 and CdSe film is deposited by vacuum evaporation at a substrate temperature of 340 °C, and a pressure of 3×10^{-6} mbar. The CdSe-based device performance was optimized by applying three thicknesses of CdSe – 50, 100, and 150 nm. The device with 100 nm thick CdSe delivered the best results as for thinner film, the V_{oc} dropped, and the thicker layer showed higher parasitic absorption resulting from lower J_{sc}. As previously mentioned in Section 4.1.1, Sb_2Se_3 is prepared by thermal evaporation at a substrate temperature of 300°C. Immediately after deposition, the stack is annealed at 350 °C for 30 min in the same chamber to improve the crystallinity. In this study, the absorber thickness is kept at 600 nm. A 30 nm-thick gold layer is thermally evaporated on top as the back contact. A QCM monitors the thickness in all the deposition processes. Also, the finished devices are annealed in a muffle furnace in ambient air at 150°C for 20 min

5.3 Results

5.3.1 Structural and Compositional Analysis

The topography of the vacuum-deposited CdSe layer (Figure 5.2) is quite similar to that of the chemical bath-deposited CdS, exhibiting the same roughness with a root mean square (RMS) of 22 nm. The grains of the CdSe layer are slightly larger, but both films are compact without voids.

Similarly, for the Sb_2Se_3 layers deposited on the two different buffers, the grain shape and the roughness do not show very large differences, having a very near RMS roughness: 18 nm for CdSe and 25 nm for CdS. AFM images show similar growth of Sb_2Se_3 on both CdS to CdSe buffer layers.

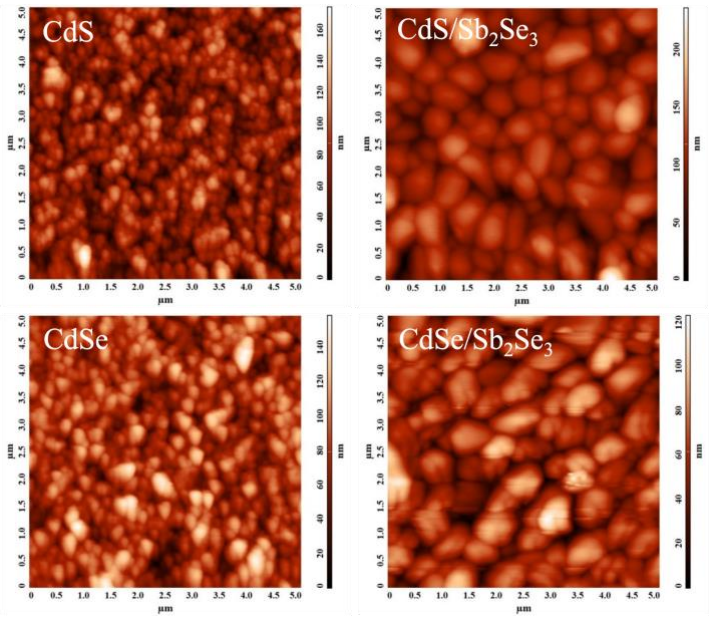

Figure 5.2 AFM images of CdS and CdSe window layers and grown Sb_2Se_3 on these films.

Sb_2Se_3 is an anisotropic material with a ribbon-like structure where orientation strongly affects electronic transport. Columnar-oriented ribbons facilitate the carrier transport between back contact and junction, requiring a predominance of the [hk1] orientations in the crystal pattern. On the other hand, [hk0] reflections highlight an orientation parallel to the substrate, which hinders the carriers' transport [47]. Sb_2Se_3 presents the typical peaks that are well-matched with the JCPDS card n. PDF 15 0861 when deposited on CdS and CdSe (Figure 5.3 (a)), with a large predominance of orientation along the [hk1] directions for both cases.

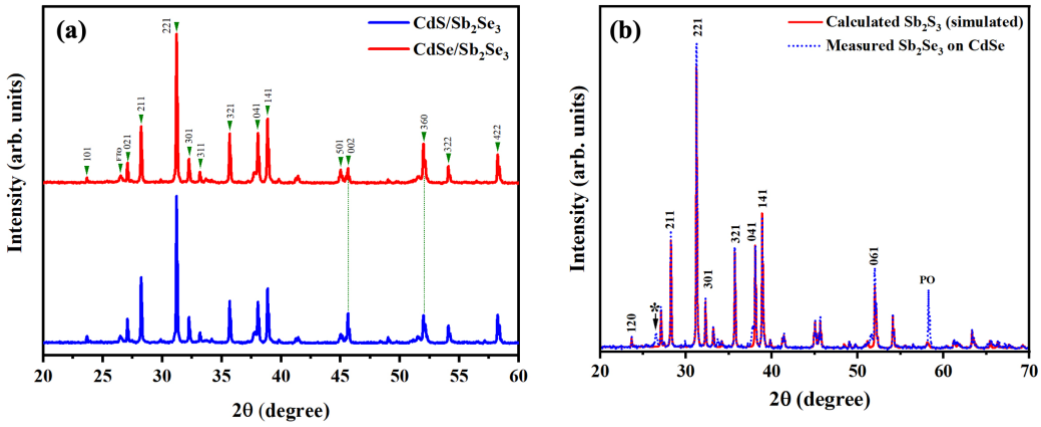

Figure 5.3 (a) XRD pattern of Sb_2Se_3 film on CdS and CdSe window layers and (b) Rietveld refinement of X-ray diffraction data for Sb_2Se_3 deposited on CdSe

Furthermore, Rietveld refinement [92], performed using the MAUD software [93] shows almost the same a and b lattice parameters but, on the other hand, highlights an increase in the value of the *c* lattice parameter for the CdSe case (Table 5.1). Consequently, the cell volume of the Sb_2Se_3 on the CdSe becomes larger than that for the CdS buffer; considering the smaller atomic radius of S compared to Se, this could suggest S diffusion and consequent replacement of Se atoms by S in the absorber with a CdS/Sb_2Se_3 junction.

Figure 5.3(b) shows the Rietveld refinement of Sb_2Se_3 deposited on a CdSe window layer. The blue circles represent the measured diffraction data, while the red line corresponds to the calculated pattern. The main diffraction peak of the CdSe substrate is marked with an asterisk (*). One specific diffraction peak, labeled "PO," is affected by the preferred orientation, as indicated by the refinement software. In this case, the effect could not be fully corrected during the refinement process.

Table 5.1 Lattice parameters of Sb_2Se_3 deposited on CdSe and CdS buffer layers, as determined by Rietveld refinement.

sample	a (Å)	b (Å)	c (Å)	V (Å^3)
Sb_2Se_3 on CdS	11.756 ± 0.001	3.970 ± 0.001	11.616 ± 0.001	542.13 ± 0.01
Sb_2Se_3 on CdSe	11.754 ± 0.001	3.972 ± 0.001	11.605 ± 0.001	541.80 ± 0.01

In the Raman spectra (Figure 5.4), the peaks around 153 and 191 cm^{-1} are commonly attributed to the Sb_2Se_3 phase; in particular, the first refers to the A_{2u} mode of the Sb-Sb bond, while the latter to the A_g mode of the Sb-Se-Sb mode. The peaks at 42 and 54 cm^{-1} have been previously

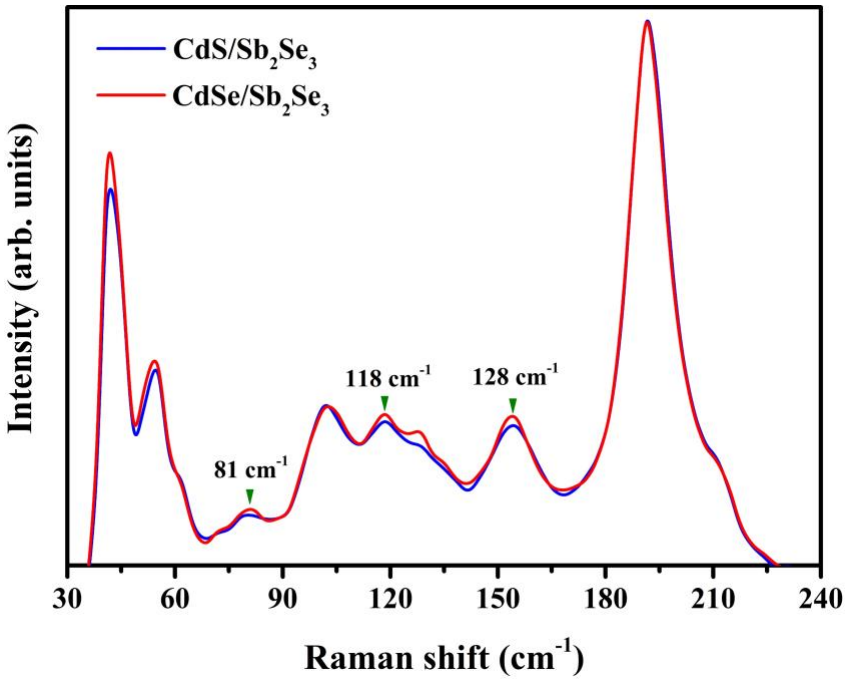

Figure 5.4 Raman spectra of Sb_2Se_3 film on CdS and CdSe window layers.

detected for the first time in our Sb_2Se_3 by evaporation, and they have been attributed to strong Sb-Se modes [94]. The Raman modes at 102 and 128 cm^{-1} are typically assigned to the Se_6 ring of the rhombohedral Se structure, while the peaks at 81 and 118 cm^{-1} are assigned to the Se-Se bond [95].

If we relate the intensity of the peaks to the main mode of Sb_2Se_3 at 191 cm^{-1}, the peaks at 81, 118, and 128 cm^{-1} are more intense for the CdSe as buffer layer; by the previous considerations, we can conclude that there is a larger presence of Se in the bulk for the CdSe/Sb_2Se_3 case. This corroborates the hypothesis that the Se-loss in the absorber is amplified by its diffusion in the CdS, driven by the concentration gradient. Thus, the application of a Se-containing buffer can strongly reduce this diffusion mechanism.

In Figure 5.5 illustrates SIMS analysis of Se and S atoms (in counts for second), as a function of the sputtering depth from the absorber surface down to the TCO. The behavior of the Se signal towards the junction is completely different in the two samples: in the CdSe case, the signal tends to be constant towards the junction; in contrast, for the CdS case, the signal decreases in the proximity of the junction.

This shows that the Sb_2Se_3 stoichiometry changes along the layer and becomes selenium-poor towards the junction. Also, the Se signal is still large in the region corresponding to the S peak,

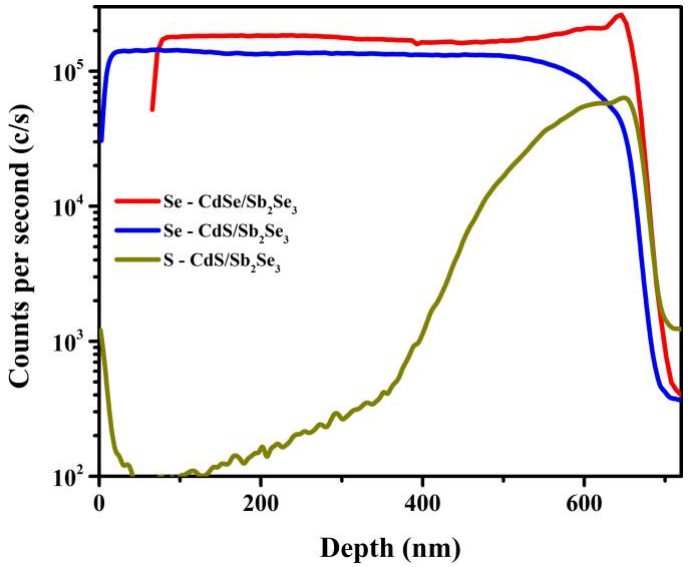

Figure 5.5 SIMS depth profiles of S and Se elements distribution through the absorber.

where we have the CdS layer. This is additional proof of the Se-diffusion into the CdS. On the other hand, the SIMS spectrum also shows an S signal for at least 200-300 nm from the junction in the Sb_2Se_3, we can conclude that in the proximity of the junction, we do have a mix of S-Se.

5.3.2 Characterization of the Device

Figure 5.6 shows the J-V characteristics of the best-performing devices (the photovoltaic parameters reported in Table 5.2), and surprisingly, CdSe-based devices illustrate a larger current. Also, the J-V parameters extracted from ten solar cells in each device are shown in Figure 5.7, where the higher average photocurrent generation is indicated. So, we have a clear improvement of the current despite the lower band gap of the CdSe layer. Overall, the fill factor and efficiency of CdSe-based devices are slightly higher and more uniform than CdS-based cells. However, the V_{oc} of $CdSe/Sb_2Se_3$ solar cells is lower than CdS/Sb_2Se_3 solar cells, which could refer to a higher conduction band offset between CdSe and Sb_2Se_3 compared to CdS. The

Table 5.2 Photovoltaic parameters of best-performing Sb_2Se_3 solar cells with CdS and CdSe buffer layers.

Device	J_{sc} (mA/cm^2)	V_{oc} (mV)	FF (%)	η (%)
CdS/S_2Se_3	21.8	335	47	3.4
$CdSe/S_2Se_3$	25	324	43	3.5

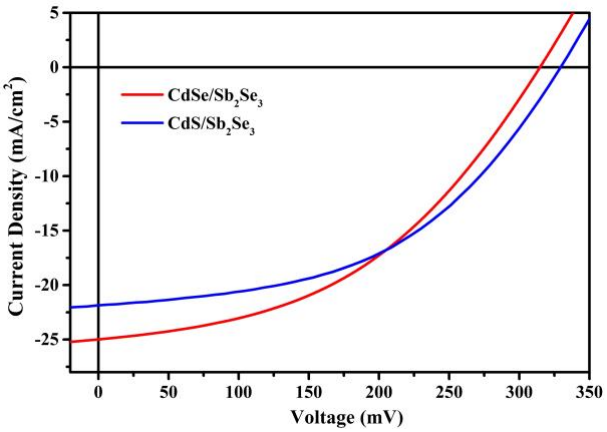

Figure 5.6 J-V curves of the best-performed Sb_2Se_3 solar cells with CdS and CdSe window layers.

parameters distribution is narrower in CdSe-based devices, offering a more homogeneous morphology of Sb_2Se_3 on the CdSe layer.

So far, CdSe has demonstrated interesting properties for Sb_2Se_3 devices. However, its narrower band gap (1.7 eV) than the CdS one (2.4 eV) would foresee reduced transparency and response in the short wavelength region of the light spectrum (Figure 5.8 b). The CdSe layer shows a lower transparency in the range from near-UV up to near-IR, but contrary to our expectation, it delivers a higher J_{sc}.

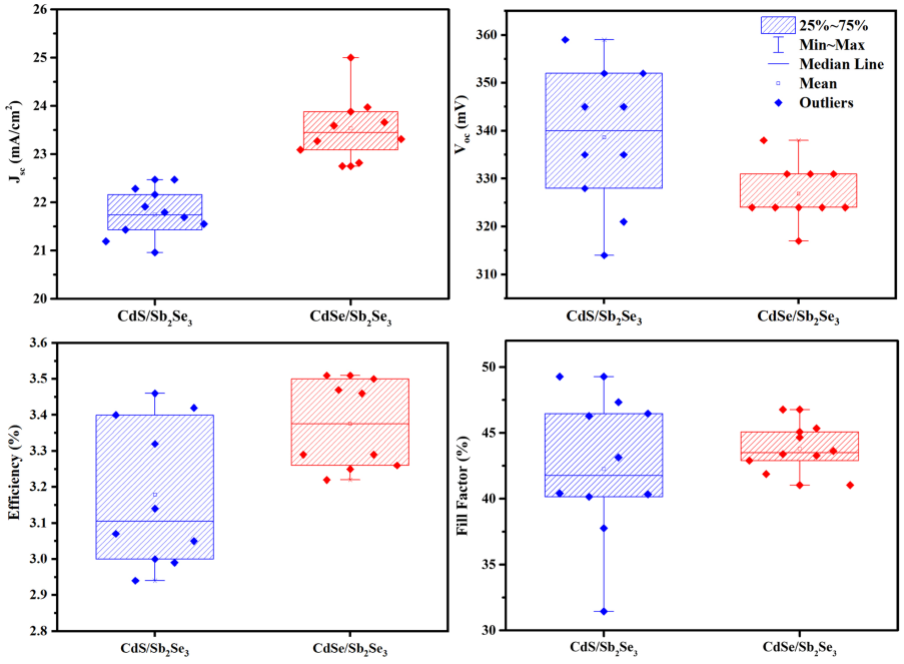

Figure 5.7 Box and whisker plots of J–V parameters extracted from CdS/Sb_2Se_3 and $CdSe/Sb_2Se_3$ solar cells (n=10)

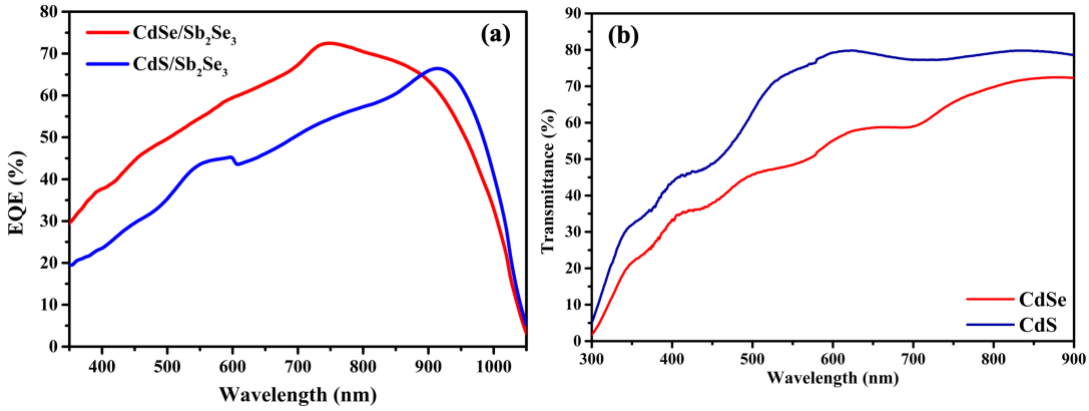

Figure 5.8 (a) EQE response of Sb_2Se_3 solar cells with CdS and CdSe window layers and (b) transmittance spectra of CdS and CdSe layers.

To address this increase in current density and verify that it is effectively connected with a different device structure, we have applied external quantum efficiency (EQE), as shown in Figure 5.8 (a). EQE shows a larger enhancement in photon absorption of CdSe/Sb_2Se_3 cells across almost the entire spectrum. The lower EQE response of the CdS/Sb_2Se_3 can be related to enhanced carrier recombination in the absorber, hence causing a larger number of defects (as recombination centers). Moreover, the EQE response tends to decrease with shorter wavelengths, corresponding to those photons collected in the proximity of the junction, suggesting an increasing number of defects near the buffer layer.

This is more pronounced for the CdS/Sb_2Se_3 devices, where the Se-S interdiffusion is demonstrated by the previously discussed SIMS analysis; the absence of this phenomenon in CdSe/Sb_2Se_3 devices explains the EQE gain and the consequent current density increase.

We addressed the defects suggested by the EQE analysis by electrical characterization of the finished devices. In Figure 5.9 (a), capacitance-voltage and drive-level capacitance profiling of cells with CdS and CdSe buffer layers are shown. CV and DLCP measurements allow us to estimate the net charge density of the absorber (acceptor minus donor states) depending on the distance from the junction. The main difference between DLCP and CV is that the first is not influenced by deep defects, so by comparing the two curves, we can identify the presence of deep states [96].

For the CdS case, the blue dots have a low carrier density, which explains the large depletion region (the strong rise of the profile is due to the influence of the back contact). Also, no difference between CV (open dots) and DLCP (full dots) is observed. Instead, for the case of CdSe, the red dots, the absorber shows a net higher charge density (roughly one order of

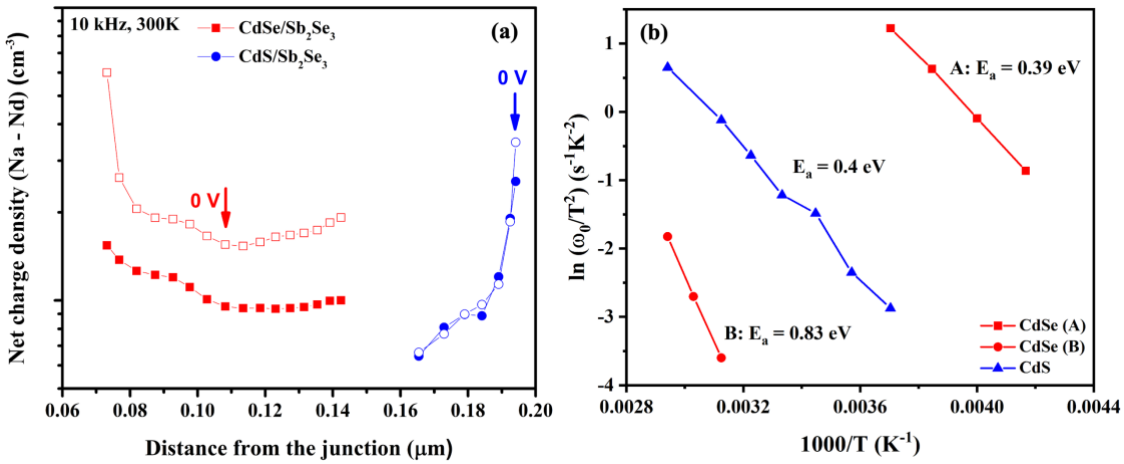

Figure 5.9 (a) CV (open dots) and DLCP (full dots) of devices with CdS (blue lines) and with CdSe (red lines) buffer layers, and (b) Arrhenius plots for three defects measured from CdS- and CdSe- based devices.

magnitude higher), with a consequent narrower depletion region. In this case, a clear difference between CV and DLCP is observed, highlighting the presence of deep defects.

To address these possible defects, we have analyzed the finished devices in terms of admittance spectroscopy, and two clear defects have been identified (Table 5.3): one level at around 400 meV (A) and the other at 830 meV (B) (Arrhenius plot is shown in Figure 5.9 (b)).

The first one is a deep acceptor, and it is generally attributed to either Sb vacancy [97], [98] or Sb_{Se} antisite [99], while the second one can be attributed only to Sb_{Se} antisite [97]. Typically, the V_{Sb} at 400 meV is always present in similar analyses, and it has been observed by many different laboratories [100], while the Sb_{Se} at 800 meV was detected by Chen et al. [97] in the case of samples with Se vapor in excess over Sb. Thus, we can conclude that the presence of the Sb_{Se} deep acceptor is additional proof that selenium loss is avoided for CdSe-based devices.

Table 5.3 Defects with their respective energy and cross sections identified by admittance spectroscopy.

CdSe				CdS		
Temp	E_a [meV]	σ_a [cm^{-2}]		Temp	E_a [meV]	σ_a [cm^{-2}]
240 K-270 K	390 ± 6	2.7 E^{-14}	A	270 K - 320 K	402 ± 14	7.5 E^{-16}
320 K- 340 K	832 ± 10	1.4 E^{-10}	B			

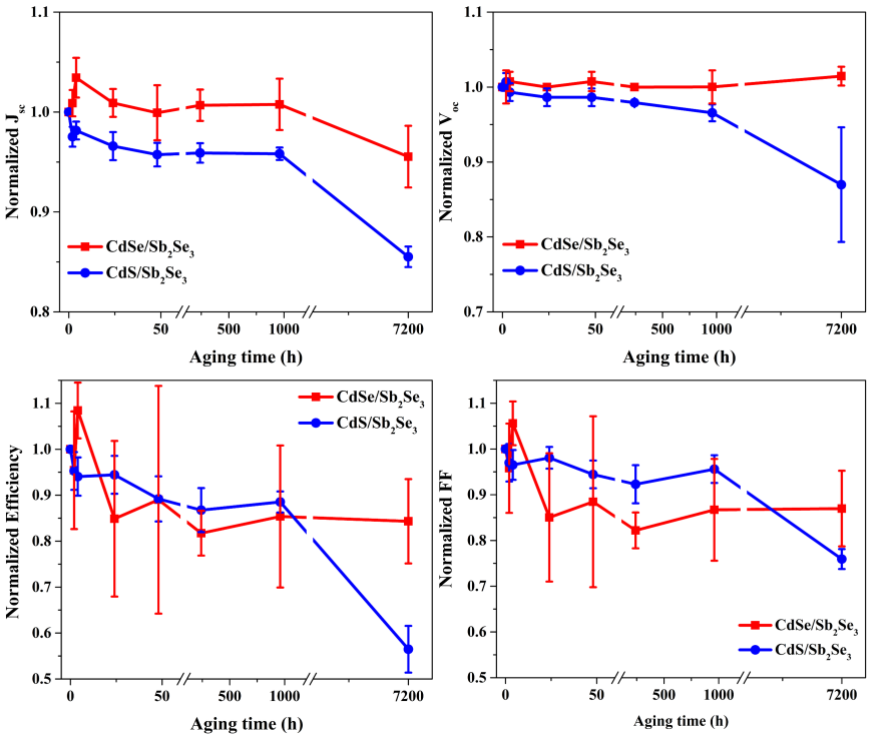

Figure 5.10 V_{oc}, J_{sc}, FF and the consequent efficiency degradation versus time under accelerated stability test of $CdSe/Sb_2Se_3$ and CdS/Sb_2Se_3 samples.

Finally, we have applied accelerated stability tests by keeping the samples in a special metal chamber where a rack of halogen lamps and a temperature-controlled system maintain an illumination of around 1000 W/m^2 and a temperature of 80 °C. The cells were placed for a time of up to 1000 hours, and their conversion efficiency was measured periodically, as shown in Figure 5.10, to see if the presence of sulphur in the structure would result in a long-term diffusion that could degrade the cells. For the $CdSe/Sb_2Se_3$ case, the values of the V_{oc} and the current are constant during the AST; on the other hand, the J_{sc} increases. For the CdS/Sb_2Se_3 case, the V_{oc} and the J_{sc} show a slight reduction; on average they respectively reach 97% and 96% of the initial values after 960 hours of AST.

The FF behaves differently: it is much more constant with CdS than with CdSe, it decreases respectively to 96% and 87% of the initial value. FF is essentially the only parameter that leads to the degradation of the efficiency of $CdSe/Sb_2Se_3$ cells, while it shows an initial improvement in the first hours: probably the generated carriers fill some of the traps at the junction leading to the initial improvement, then a second phenomenon takes place.

After 960 h of testing, both devices show good stability, with attested efficiency values of 89% and 85% of the initial ones, respectively, for CdS and CdSe.

Our results on degradation are in contrast with what has been reported by Guo et al. [91]. In particular, their devices with CdS showed a strong instability under AST just after 120 hours, with a reduction to 70 % of the initial conversion efficiency, while no degradation is reported with CdSe. The different behavior can be explained by the different absorber deposition techniques. For Guo et al., a high substrate temperature CSS deposition is used, enhancing the sulfur diffusion from the buffer to the absorber. Instead, our substrate temperature, during deposition, does not exceed 300 °C, resulting in a reduced intermixing of CdS and Sb_2Se_3.
However, going longer in time, if we look at the last point reported on the graphs, corresponding to 7200 hours, an evident degradation of the devices with CdS buffer layer is registered. This finally confirms that CdS enhances instability, even if for low substrate temperature deposited devices (like ours) is limited.

5.4 Conclusion

CdSe has been applied for the first time as an alternative buffer to Sb_2Se_3 cells on a superstrate configuration fabricated by vacuum evaporation at low substrate temperature. CdSe/Sb_2Se_3 devices have been analyzed and compared to the typical CdS/Sb_2Se_3 structure. The growth on CdSe leads to a flatter and more compact surface of the absorber, with a larger presence of bigger grains. XRD points out the predominance of [hk1] crystal orientations in Sb_2Se_3 deposited on both CdS and CdSe, therefore, with the ribbons oriented perpendicularly on the substrate to favor the carrier transport mechanism [101]. On the other hand, Rietveld refinement reveals a smaller cell volume for Sb_2Se_3 deposited on CdS, which suggests S diffusion and consequent replacement of Se atoms by S in the absorber. Raman analysis indicates a larger presence of Se in Sb_2Se_3 using CdSe, supporting the hypothesis that avoiding a concentration gradient for selenium at the junction reduces the loss of Se in the absorber. Moreover, SIMS analysis clearly shows the interdiffusion of S and Se with CdS, with a deficiency of Se in Sb_2Se_3 towards the junction, while with CdSe, in the absorber, the Se profile increases toward the junction.
Despite the lower transparency of CdSe, due to its narrower band gap, CdSe/Sb_2Se_3 cells perform at higher current densities. The FF also improves, while the V_{oc} slightly decreases, again due to the narrower band gap compared to CdS.

The current gain is due to an increase of the quantum efficiency at all wavelengths, which can be explained by a reduction of the carrier recombination in the absorber, therefore to a reduced number of defects, most probably related to S - Se interdiffusion.

Finally, CdSe/Sb_2Se_3 cells also show good stability when submitted to accelerated stability tests: after 960 h of accelerated lifetime testing, they perform 85% of the initial efficiency. A longer AST highlights a higher degradation for the CdS-based devices.

In conclusion, the use of a selenium-containing buffer layer has been proved to avoid the S – Se interdiffusion, a phenomenon observed in the more widely used CdS/Sb_2Se_3 structure, therefore and improving the current density.

Chapter Six

Cd-free vs. Cd-based window layers: Introducing SnO_2 window layer to Sb_2Se_3 solar cells

6.1 Introduction

The previous chapter introduced CdSe as an alternative window layer and compared it to the most common CdS window layer for Sb_2Se_3 thin film solar cells. However, Cd-based buffer layers introduce material incompatibility and environmental challenges due to the presence of Cd. Cd-based window layers –CdS (2.4 eV) and CdSe (1.7 eV)– are narrow-bandgap materials, resulting in parasitic absorption and lowering photocurrent generation. Cd interdiffusion (in our study, Figure 6.1) into the absorber (particularly in high-temperature growth techniques) results in an increased number of defects, lowering the efficiency of the devices [60]. These obstacles urge exploring alternative wide-bandgap, Cd-free window layers for Sb_2Se_3 solar cells.

The above issues have been addressed by introducing novel buffer layers such as TiO_2, SnO_2, and ZnO, which all have smaller lattice mismatches with Sb_2Se_3 [102]. However, the band alignment of each material with Sb_2Se_3 has been reported as both cliff-like and spike-like based on the fabrication process [69], [70], [75]. Lately, introducing these window layers has led to high-efficiency Sb_2Se_3 solar cells [72] and increased device stability [46], offering the potential of Cd-free transparent window layers for Sb_2Se_3 solar cells.

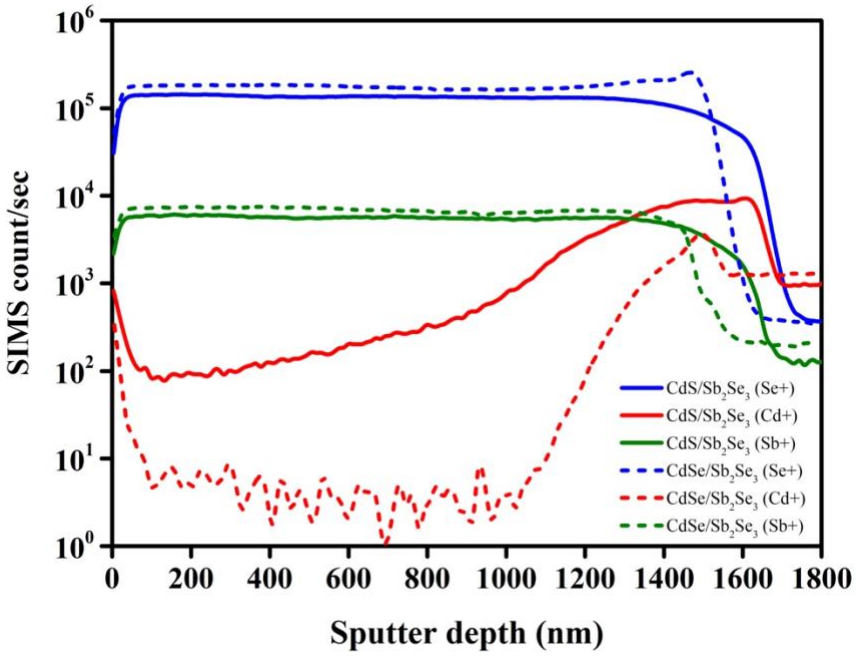

Figure 6.1 SIMS profiles of Cd, Sb, and S elements distribution through Sb_2Se_3 solar cells with CdS and CdSe window layers.

SnO_2 is a promising alternative window layer for Sb_2Se_3 thin-film solar cells due to its non-toxicity, suitable bandgap, good transparency, and stability. Theoretical studies suggest SnO_2 enables better charge separation and reduced carrier trapping compared to CdS [103]. Experimentally, efforts using SnO_2-based ETLs, such as spray pyrolysis [75], La-doping [104], TiO_2 modification [105], and $CdCl_2$ treatment [106], have achieved progressive improvements in efficiency, with PCEs exceeding 4%. Lately, annealing SnO_2 film deposited by atomic layer deposition (ALD) in a substrate device structure increased the efficiency to 7.29%, comparable to other Cd-free based solar cells [76].

As discussed in the previous chapter, the CdSe window layer improves the photocurrent and device stability compared to CdS-based devices. According to our results, Cd diffusion to the junction (Figure 6.1) and parasitic absorption (EQE curves, Figure 5.8 a) are still limiting factors for Cd-based buffer layers.

Here, we have introduced the SnO_2 buffer layer grown by ALD, allowing the deposition of a uniform pinhole-free film with precise thickness. The thickness of SnO_2 layer has been optimized to favor the best device performance. In this superstrate configuration, due to the impact of the window layer on active layer growth and the formation of the junction, the structural properties of Sb_2Se_3 and the electrical properties of the device have been analyzed.

The results are compared with those of a CdSe-based device to understand how these buffer layers affect the device's performance.

6.2 Device Fabrication

The solar cells have been fabricated using the same process as in Section 5.2.1, with two notable differences: fluorine-doped tin oxide (FTO) coated soda lime glass was used as the TCO, and no post-annealing treatment was applied on finished devices.

The SnO_2 window layer was prepared using the ALD method, as explained in Section 4.1.2. Figure 6.2 shows the J-V curves of the best-performed cells with various thicknesses of SnO_2, and their photovoltaic parameters are tabulated in Table 6.1.

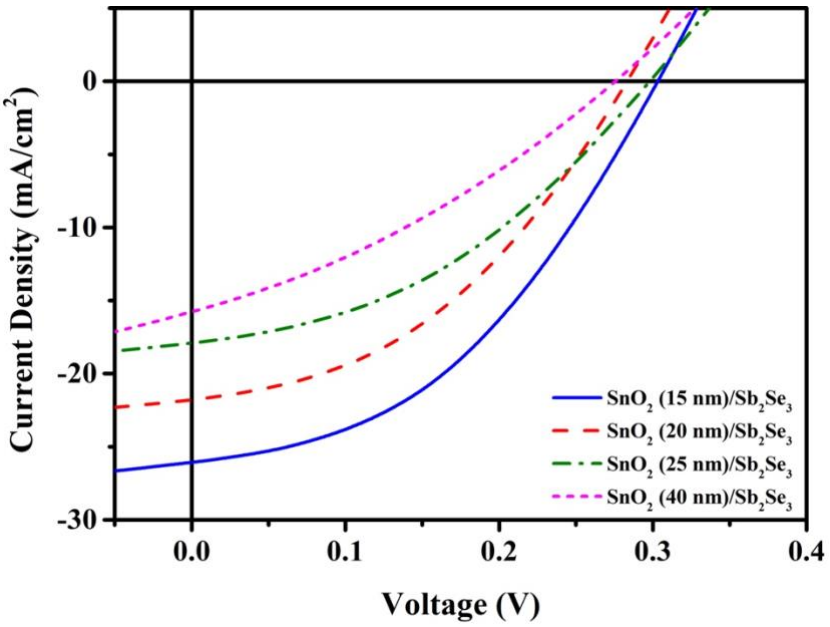

Figure 6.2 J-V curves of SnO_2/Sb_2Se_3 solar cells with different SnO_2 thickness.

All SnO_2 films provide good transparency, although the photocurrent has dropped by increasing the thickness of the window layer, which could originate from the higher resistivity of films. All devices present comparable V_{oc} values, indicating a decent p-n junction formation, but by increasing the thickness, V_{oc} decreases. R_{sh} and R_s lower the photocurrent and photovoltage values in all cases, but the effect appears extreme for J-V curves of thicker window-layer cells, especially 25 and 40 nm. Overall, the thinnest SnO_2 film with 15 nm thickness presents the best photovoltaic parameters.

The following sections will discuss the structural and electrical properties of Sb_2Se_3 solar cells and compare the optimized SnO_2- and CdSe-based devices.

Table 6.1 The photovoltaic parameters of best-performing SnO_2/Sb_2Se_3 solar cells with different thicknesses.

Device	J_{sc} (mA/cm^2)	V_{oc} (mV)	FF (%)	η (%)
SnO_2 (15 nm)	26	303	42	3.3
SnO_2 (20 nm)	22.6	282	40	2.6
SnO_2 (25 nm)	17	300	40	2
SnO_2 (40 nm)	15	278	34	1.5

6.3 Results

6.3.1 Structural and Compositional Analysis

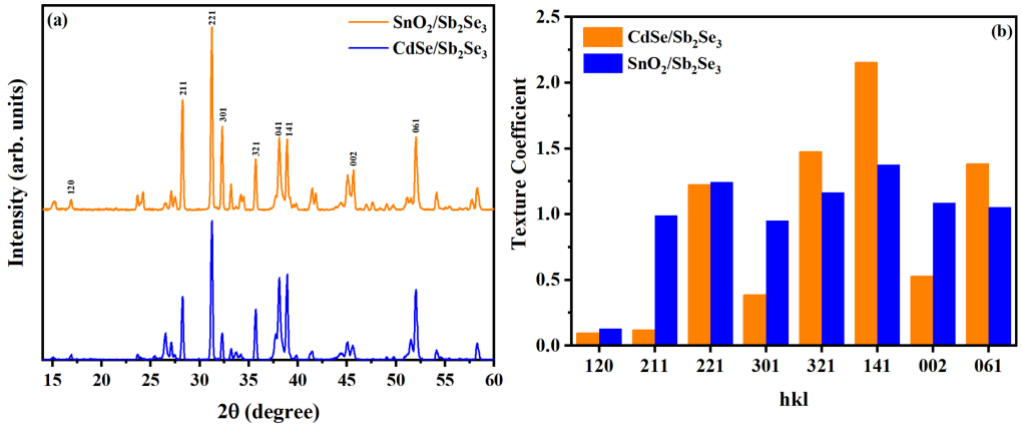

Figure 6.2 (a) XRD peaks and (b) TC values of Sb_2Se_3 film grown on CdSe and SnO_2 buffer layers.

Figure 6.2 (a) displays the XRD peaks of Sb_2Se_3 deposited on CdSe and SnO_2 buffer layers. The observed peaks are aligned with the orthorhombic Sb_2Se_3 structure (JCPDS No. 15-0861). Since Sb_2Se_3 is an anisotropic material, the crystal chains along [001] orientation enhance the charge transport mechanism. Among these orientations, the [221], [211], and [002] have been identified as preferred due to their larger angles relative to the surface [107]. The texture coefficient (TC) of the diffraction peaks (Figure 6.2 (b)) has been calculated using the Equation:

$$TC_{hkl} = \frac{I_{hkl}}{I_{0\,hkl}} / \left(\frac{1}{N} \sum_N \frac{I_{hkl}}{I_{0\,hkl}} \right)$$

Where I_{hkl} and $I_{0\,hkl}$ represent the observed peak intensity of the [hkl] direction and the intensity in the standard XRD pattern, respectively. N is the number of reflections considered for the calculation. TC value of a diffraction larger than one indicates a preferential orientation of the grains along that direction.

As illustrated in Figure 6.2 (b), Sb_2Se_3 on both buffer layers shows TC values greater than 1 for various [hk1] directions, including [221], [321], [141], and [061]. For the CdSe buffer layer, the preferred orientations are [321], [141], and [061], which have smaller angles to the surface. In comparison, Sb_2Se_3 on the SnO_2 substrate exhibits TC values of one for the [211] and [002] planes, which are more normal to the surface. This suggests that Sb_2Se_3 exhibits more columnar growth on the SnO_2 buffer layer, which could result in a higher photocurrent generation.

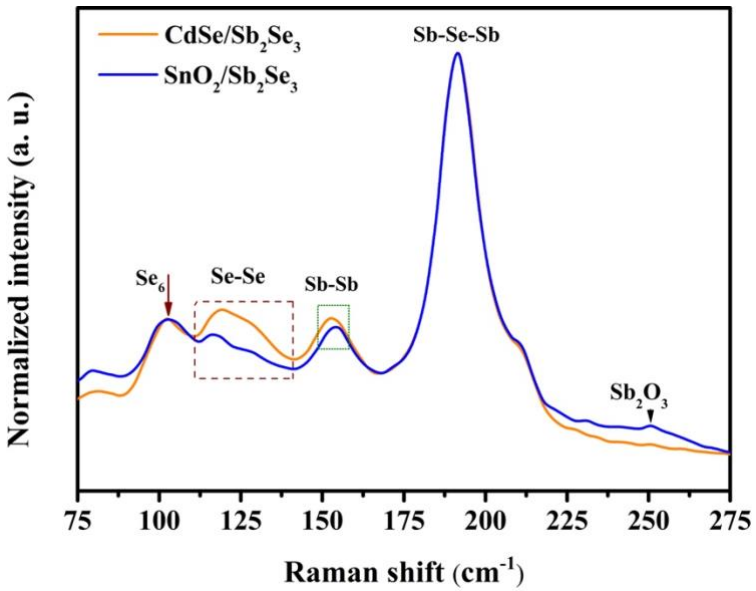

Figure 6.3 Raman spectra of Sb_2Se_3 on CdSe and SnO_2 buffer layers.

Raman analysis has been performed to confirm the composition and structural quality of Sb_2Se_3 (Figure 6.3). The peaks appear around 155 and 191 cm^{-1}, which are attributed to Sb_2Se_3 phase, referring to A_{2u} mode of the Sb-Sb bond, and A_g mode of the Sb-Se-Sb mode, respectively. The peaks observed between 100 to 140 cm^{-1} are associated with Se_6 and Se-Se bonds. At 101 cm^{-1}, both cases exhibit similar behavior, although the peak intensity in the 110 to 140 cm^{-1} area is reduced for the SnO_2 substrate. Additionally, a slight red shift and lower intensity are observed for the SnO_2 substrate around 155 cm^{-1}. According to Fleck et al., Sb_2Se_3 films

oriented along the [001] exhibit minimal or no Raman activity around 155 cm^{-1} which can be counted as an approach to confirm the crystallinity of Sb_2Se_3 [108]. The observed behavior at 155cm^{-1} could be consistent with the higher TC value of Sb_2Se_3 on the SnO_2 buffer layer.

Table 6.2 EDX results of Sb_2Se_3 films on CdSe and SnO_2 buffer layers.

Sample	Sb %	Se %	Sb/Se
$CdSe/Sb_2Se_3$	41.24	58.06	0.71
SnO_2/Sb_2Se_3	41.05	58.95	0.69

Figure 6.4 displays scanning electron microscope (SEM) images of Sb_2Se_3 grown on CdSe (a) and SnO_2 (b). Compared to Sb_2Se_3 on CdSe, Sb_2Se_3 on SnO_2 reveals a much larger grain size, reaching up to 1 μm, demonstrating a strong influence of the buffer on the growth of Sb2Se3. The EDX results (Table 6.2) reveal a deviation from the Sb:Se ratio, which is less pronounced in the case of the SnO_2 layer. This effect can be seen in Raman spectra as the area between 110 to 130 cm^{-1}, which is associated with Se bonds, shows different behavior between CdSe and SnO_2 layers.

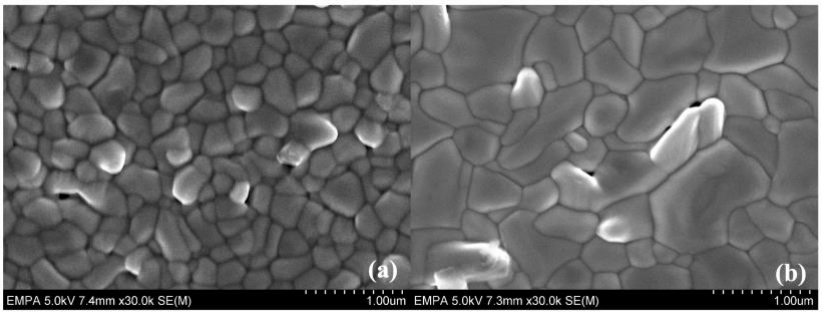

Figure 6.4 SEM images of Sb_2Se_3 films on (a) CdSe and (b) SnO_2 buffer layers.

6.3.2 Device Characterization

J–V curves (Figure 6.5 (a)) and the corresponding photovoltaic parameters (Table 6.3) of the best cells of SnO_2- and CdSe-based devices appear almost similar, but SnO_2/Sb_2Se_3 cell exhibits a higher photocurrent generation, which could be expected due to the transparency of SnO_2 layer. The statistics of photovoltaic parameters of both devices (Figure 6.6) provide

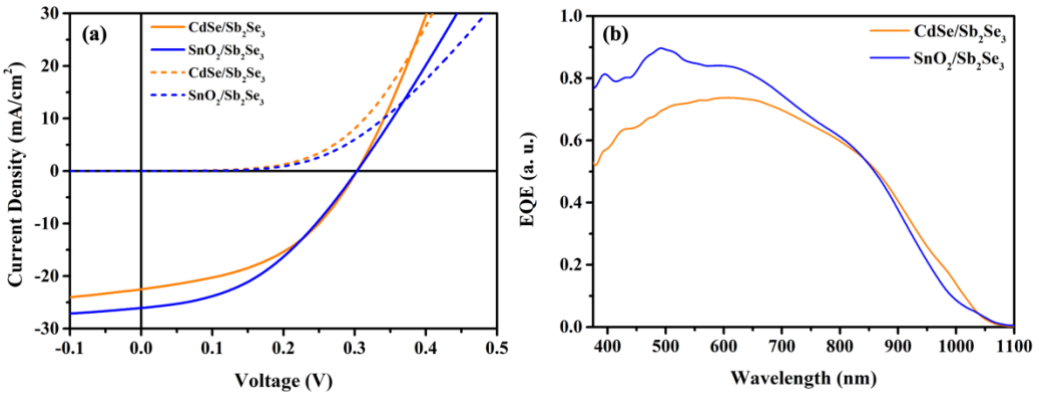

Figure 6.5 (a) J–V and (b) EQE curves of $CdSe/Sb_2Se_3$ and SnO_2/Sb_2Se_3 thin film solar cells.

further insight into the electric behavior of the p-n junctions. Overall, J_{sc} values are higher in the case of SnO_2 but more uniform in CdSe-based devices. EQE response of both devices (Figure 6.5 (b)) in the short wavelength region demonstrates how the SnO_2 layer compensates for carrier loss that occurs in the CdSe buffer layer. SnO_2/Sb_2Se_3 cell shows a higher EQE response (above 80%) between 400-700 nm wavelengths. But in longer wavelength region a carrier collection problem is observed in both cases. Despite more columnar and larger grain sizes of Sb_2Se_3 on SnO_2 buffer layer, the result confirms J_{sc} increase due to the wider bandgap of SnO_2 not necessarily improving film quality. Although the V_{oc} of the highest-performed cells in both cases are equal, the distribution of V_{oc} values is more uniform and in average, higher for the SnO_2/Sb_2Se_3 device. Also, the SnO_2/ Sb_2Se_3 solar cells illustrate slightly higher efficiencies. However, fill factor values are lower for the SnO_2 case –originating from the higher resistivity of this metal oxide film– resulting in larger series resistance (R_s).

Table 6.3 Photovoltaic parameters of the best-performing $CdSe/Sb_2Se_3$ and SnO_2/Sb_2Se_3 solar cells.

Sample	J_{sc} (mA/cm^2)	V_{oc} (mV)	FF (%)	η (%)
$CdSe/Sb_2Se_3$	22.8	303	45	3
SnO_2/Sb_2Se3	26	303	42	3.3

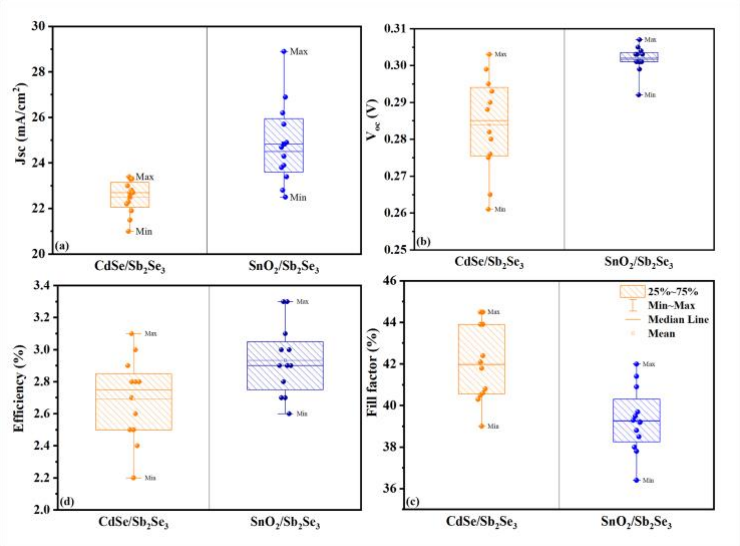

Figure 6.6 Box plot of photovoltaic parameters of SnO_2/Sb_2Se_3 and $CdSe/Sb_2Se_3$ solar cells (n=12).

Also, AST was performed for up to 100 hours to track the stability of the devices in stressed conditions. J-V measurement of solar cells was frequently carried out, and the results are presented in Figure 6.7. Both devices illustrate acceptable stability over time, but the J_{sc} values of the SnO_2-based cells degraded slightly while they improved for CdSe-based cells. However, photovoltage is stable in both cases, with a slight increase in CdSe/Sb2Se3 solar cells. Finally, the efficiency of CdSe-based solar cells is improved while it is decreased in SnO_2 case. This could suggest that leaving the device at temperatures just above room temperature (a mild

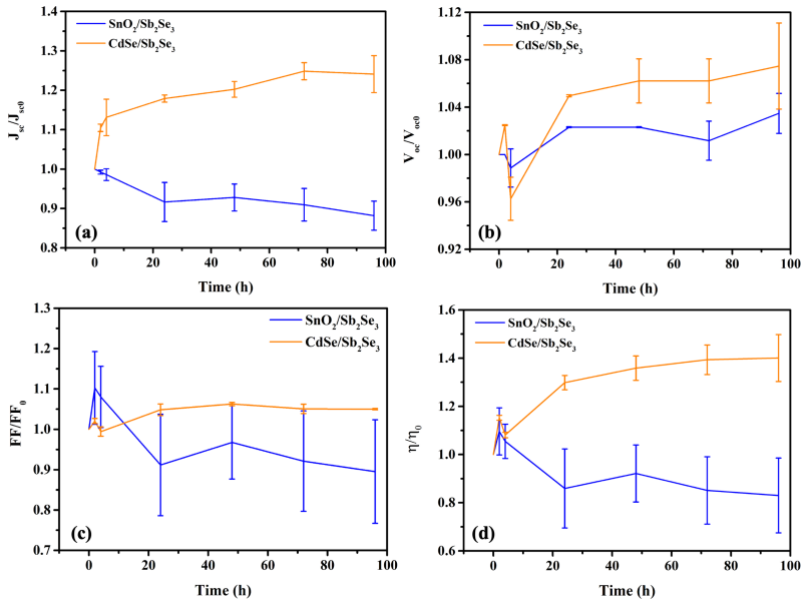

Figure 6.7 V_{oc}, J_{sc}, FF and the consequent efficiency degradation versus time under accelerated stability test of SnO_2/Sb_2Se_3 and $CdSe/Sb_2Se_3$ solar cells.

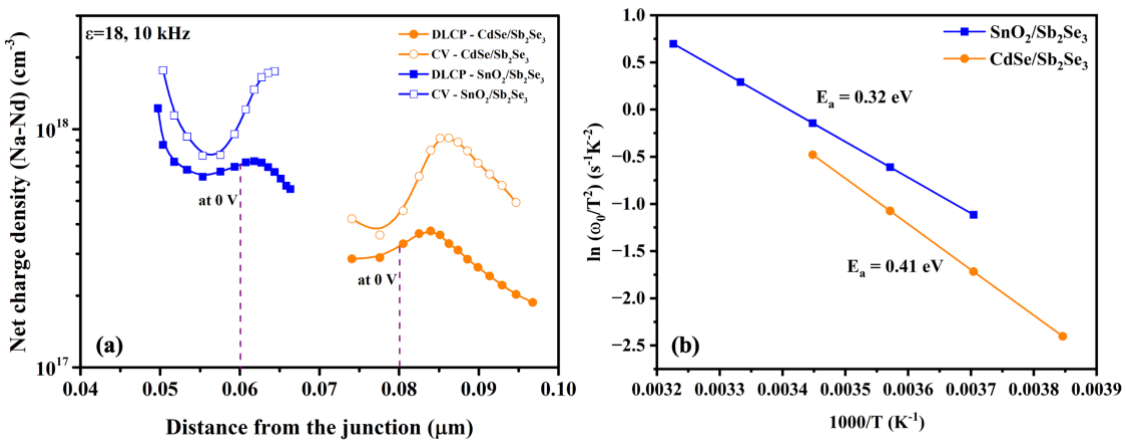

Figure 6.8 (a) CV (open dots) and DLCP (full dots) of devices with SnO_2 (blue lines) and with CdSe (red lines) buffer layers and (b) Arrhenius plot for two defects measured from CdSe- and SnO_2- based devices.

annealing treatment) could be beneficial in improving the efficiency of CdSe/ Sb_2Se_3 devices. An air post-annealing treatment (explained in section 5.2.1) was carried out after Sb_2Se_3 deposition that, in the CdSe case, resulted in improved photovoltaic parameters while being destructive in SnO_2-based devices. This could originate from different morphology of the active layer on these two substrates, eliminating the effect of the treatment. The effect of air post-annealing treatment is discussed in Chapter Seven.

Notably, the stability results for CdSe-based solar cells shown in Chapter 5 (Figure 5.10) and Chapter 6 (Figure 6.7) seem to show a discrepancy. This difference likely refers to different fabrication processes –the type of TCO used and whether a post-annealing treatment was applied. As mentioned earlier, post-annealing helped improve the performance of CdSe-based cells but had a negative impact on SnO_2-based ones. The AST experiments discussed in this chapter were carried out on devices that didn't undergo post-annealing in order to ensure a consistent basis for comparison.

Finally, to estimate the doping profile and the presence of deep-level defects, we performed capacitance-voltage (CV) and deep-level capacitance profiling (DLCP), presented in Figure 6.8. Doping concentrations in the space charge region (SCR) of SnO_2- and CdSe- based cells are estimated to be 2-3×10^{17} cm^{-3} and 6-7×10^{17} cm^{-3}, respectively. The higher doping density of solar cells with SnO_2 layer offers a lower defect concentration. In both devices, the deviation of DLCP from the CV curve demonstrates the presence of deep defects at the junction (V = 0). However, this deviation becomes larger and farther from the junction, which could suggest bulk defects in the absorber. This is consistent with the observed carrier loss at longer wavelengths in the EQE responses of both cells (Figure 6.5 (b)).

Additionally, admittance spectroscopy was implemented to identify the defect levels. We found one defect level for each device, which is presented in Table 6.4. The activation energies of these defects are in the range of 0.3-0.4 eV, which, according to the literature, are likely to be antistite defects like Sb-on-Se, Se-on-Sb, or selenium vacancies [100]. The defect levels were extracted by analyzing the temperature dependence of the emission time constants. These time constants were extracted from the frequency at which the capacitance response peaked in the admittance spectra. To estimate the activation energies of the defects we used the Arrhenius plot, which is shown in Figure 6.8(b). However, the identified defect in SnO_2-based solar cell appears shallower, which is inconsistent with the higher doping density.

Table 6.4 Defects with their respective energy identified by admittance spectroscopy.

Device	Temperature (K)	Ea (meV)
SnO_2/Sb_2Se_3	260-310	327 ± 6
$CdSe/Sb_2Se_3$	240-270	416 ± 9

6.4 Conclusion

Achieving high-efficiency Sb_2Se_3 solar cells requires mitigating defect formation, and a window layer plays a crucial role, especially in minimizing interface defects. While we addressed sulfur diffusion in Chapter Five, Cd diffusion into the active layer could result in interface defects. This interdiffusion was observed even under low-temperature growth conditions, such as thermal evaporation, degrading the device's performance.

SnO_2 can be an excellent alternative window layer for Cd-based buffer layers, although the high resistivity of the film can be a limiting factor. In this study, we applied SnO_2 using the ALD method, providing a flawless film and reducing the thickness to 15 nm. This ultra-thin film of SnO_2, with its wide band gap of 3.6 eV, significantly enhances the transparency of the window layer. As a result, it eliminated the parasitic absorption of CdSe, or similarly CdS, film in the short wavelength region (400-600 nm), resulting in an increased J_{sc} of SnO_2-based solar cells with a net gain of 2 mA/cm^2.

Additionally, our superstrate device structure provided an effective substrate, facilitating the columnar growth of Sb_2Se_3 with larger grain sizes compared to the CdSe case. The structural improvement is potentially beneficial for charge movement, as we observed a slightly higher

EQE response at the wavelengths between 600-800 nm for SnO_2-based solar cells. The carrier collection losses at higher wavelengths should be addressed by further optimizing the growth condition of Sb_2Se_3 or by introducing post-treatment.

Solar cells with SnO_2 buffer layer performed a higher V_{oc} that could originate from structural improvement and lower defect density due to eliminated Cd diffusion. The CV and DLCP profiling revealed the presence of deep defects at the junction in both cases, but admittance spectroscopy identified a shallower defect of solar cells with SnO_2 layer. Moreover, these devices showed a higher charge carrier density, suggesting a lower defect density, which led to improved efficiency.

Overall, by applying the SnO_2 window layer, parasitic absorption and Cd diffusion are eliminated, leading to improved J_{sc} and V_{oc} values. The carrier dynamics of CdSe- and SnO_2-based solar cells are different and present slightly better behavior in the SnO_2 case. The results present SnO_2 as a potential buffer layer for Sb_2Se_3. However, more optimization of Sb_2Se_3 growth on this buffer layer could result in enhanced efficiency.

Chapter Seven

Impact of Absorber Thickness and Air Annealing Treatment on Solar Cell Performance

7.1 Introduction

So far, CdSe has been applied as an alternative to CdS in Sb_2Se_3 solar cells. While CdSe increased the J_{sc} and enhanced the stability of the solar cells by eliminating sulfur diffusion, cadmium diffusion and parasitic absorption in these narrow bandgap window layers stayed challenging. Introducing the SnO_2 window layer addressed these issues; however, carrier collection losses within the bulk of the absorber remained a bottleneck to achieving higher efficiencies, guiding us toward further material optimization.

In this thesis, Sb_2Se_3 was grown via thermal evaporation– a growth method based on low substrate temperature compared to other deposition techniques that allow precise control of absorber thickness. Sb_2Se_3 can undergo phase transition during deposition due to the partial vapor pressure of selenium, resulting in a Se-poor film. Therefore, we kept the material source at low temperatures and deposition rates to avoid selenium loss during growth, leading to long deposition durations. Growing Sb_2Se_3 at a low substrate temperature and a long deposition time could result in reorientation in Sb_2Se_3 crystal planes in thicker films. Thus, in the first section of this study, we investigate the influence of thickness on structural and electrical properties on absorber and device performance.

Various annealing treatments of Sb_2Se_3 thin films have been reported to be beneficial, for instance, annealing in vacuum [109], Se [42], and H_2S [110] ambient. Post-annealing in a vacuum condition improved the crystallinity of the film, while post-selenization increased the V_{oc} of Sb_2Se_3 solar cells to 494 mV by passivating deep defects. Post-deposition of H_2S on thermally evaporated Sb_2Se_3 film compensated Se vacancies.

Additionally, positive impacts of oxygen presence at the junction [64], [111], and at the back contact [112] have been observed. Oxygenating the CdS window layer avoided the Cd diffusion and the consequent defect formation at the junction [64]. Controlled addition of oxygen during thermally evaporated Sb_2Se_3 leads to similar junction improvements resulting in higher J_{sc} and V_{oc} [8]. Also, leaving Sb_2Se_3 in air at room temperature has been demonstrated to form a few nanometers thick of the Sb_2O_3 layer. Oxygen exposure created a Se-rich film at the back contact, lowering the junction barrier and consequently improving the back contact [112].

As our results of the thickness impact on absorber properties have been offered, we applied a post-annealing treatment (PAT) in ambient air at low temperatures in the second section of the study.

7.2 Device Fabrication

The solar cells have been fabricated using the same process as in Section 5.2.1. Two different thicknesses of Sb_2Se_3 films were deposited to study the impact of the absorber thickness on the device's properties. The devices are labeled T400 and T1200 according to their absorber thickness, respectively 400 nm, and 1200 nm. Finally, one device from each batch undergoes a post-annealing treatment (PAT) in a muffle furnace, and the resulting samples are labeled T400-PAT and T1200-PAT. The annealing temperature and duration have been optimized at a temperature of 150°C for 20 min.

7.3 Thickness impact

7.3.1 Structural and Compositional Analysis

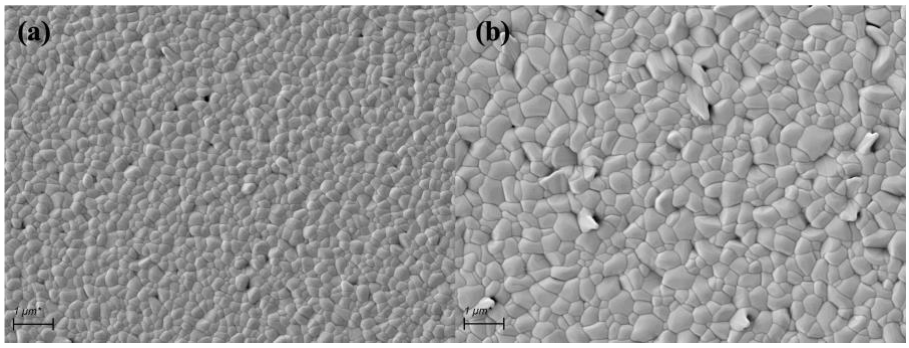

Figure 7.1 Top-view SEM images of (a) T400 and (b) T1200 Sb_2Se_3 thin films.

SEM images of Sb_2Se_3 films (Figure 7.1) display a morphology variation by increasing thickness. The grain shapes become more irregular, causing protrusions and voids in the thicker film. Such structural imperfections in thick film might eventually be responsible for generating defects associated with recombination losses. While the average grain size increases from about 200 nm to 300 nm, the 400-nm Sb_2Se_3 film provides densely packed grains with uniform distribution.

To determine how the thickness affects the crystalline properties of the Sb_2Se_3 film in a solar cell, structural characterizations have been analyzed using XRD and GIXRD measurements of CdSe/Sb_2Se_3 solar cells, confirming the orthorhombic Sb_2Se_3 phase. The peaks indicate that the films are oriented along the [hk1] directions but with different texture coefficients, as reflected by the different peak intensities. From the texture coefficient (TC) analysis, both films exhibit texture coefficients larger than one along the [021], [221], [321], [041], and [141].

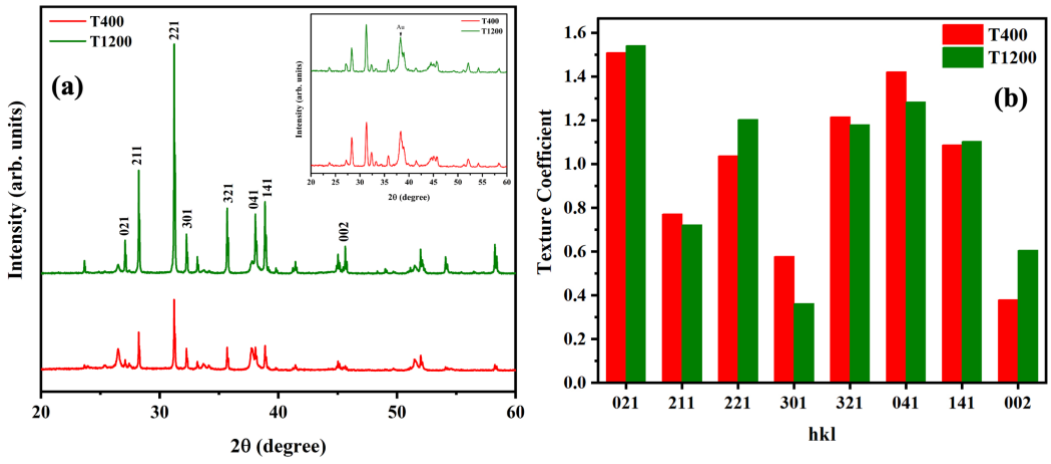

Figure 7.2 (a) XRD peaks, GIXRD peaks in the inset, and (b) texture coefficient of CdSe/Sb_2Se_3 solar cell with varying Sb_2Se_3 film thickness.

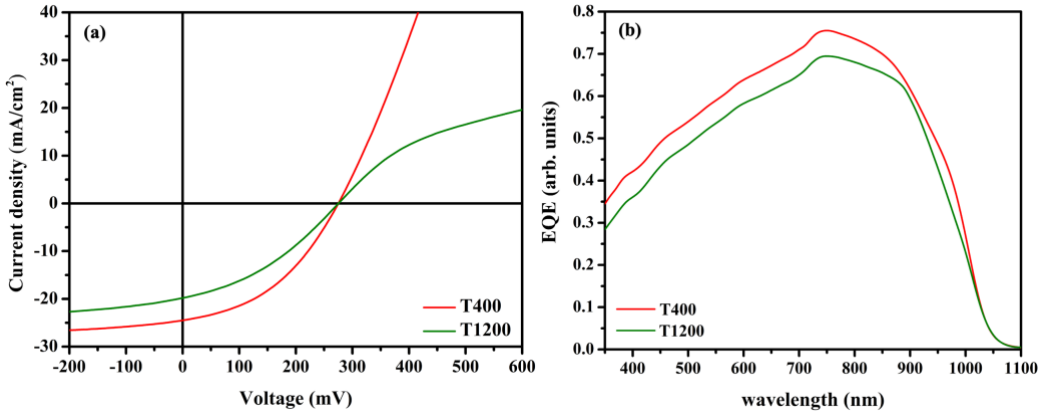

Figure 7.3 (a) J-V and (b) EQE results of CdSe/Sb_2Se_3 solar cells with varying absorber thickness.

However, by increasing the thickness, the T1200 film crystal orientation becomes more columnar showing higher intensity of reflection such as [221]. Such development may imply an increase in carrier mobility, which agrees with the larger grain size observed from the SEM images. GIXRD analysis is more surface-sensitive due to the shallow penetration of the incident X-rays, providing insight into the near-surface structure of Sb_2Se_3 films or ultra-thin films. In the inset of Figure 7.2 (a), GIXRD patterns are less intense and broader compared to the main XRD, indicating small grain sizes. Also, there is no evidence of reorientation of grains through growth and increasing the film thickness.

7.3.2 Device Characterization

J-V results for the best-performing solar cells of the discussed films are presented (Figure 7.3 (a) and Table 7.1), and the T400 device achieves a higher efficiency. Despite its relatively lower film thickness, which may limit the light absorption, this device demonstrated a higher J_{sc}. Furthermore, T400 solar cell shows the highest EQE response throughout the spectrum, confirming superior carrier collection with respect to T1200 cell. Also, in the J-V curve of T1200 solar cell, a drop in current density is noticeable at higher forward bias voltages. This

Table 7.1 Photovoltaic parameters of best-performing CdSe/Sb_2Se_3 thin film solar cells with different thicknesses.

Sample	J_{sc} (mA/cm^2)	V_{oc} (mV)	FF (%)	η (%)	R_{shunt} (Ω)	R_{series} (Ω)
T400	24.3	279	41.2	2.8	384.3	34.5
T1200	23	279	34.6	2.2	232.6	56.9

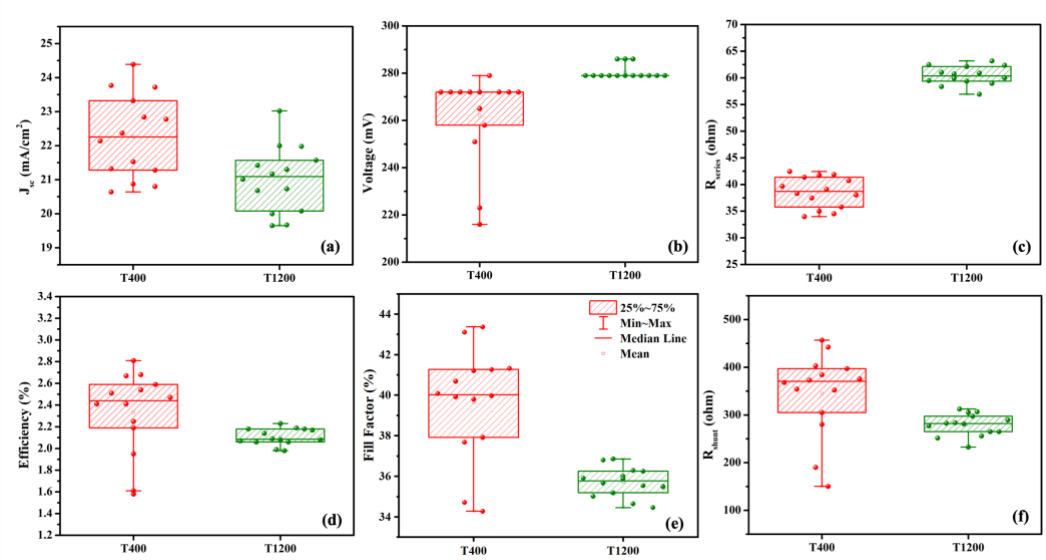

Figure 7.4 Plot box of photovoltaic parameters of different thick Sb_2Se_3 solar cells.

behavior is known as the *rollover effect* due to back contact issues commonly observed in thin film solar cells [113], [114]. It arises when the absorber layer forms a poor ohmic contact with the back metallic contact due to surface states, unfavorable band alignment, or other contact-related limitations [115]. As briefly discussed in Section 2.3, such conditions can create a barrier at the back contact, limiting hole transportation. The rollover effect mainly reduces the fill factor [115], as seen in the T400 cell, which shows no rollover and a higher fill factor.

A detailed insight into the performance of the devices is given by the box plot of twelve solar cells per device. Generally, the distribution of the photovoltaic values is narrower in the case of thicker-film devices due to their improved crystallinity, except for J_{sc}. Whereas the T400 device illustrates higher average values in most of the parameters, V_{oc} is rather higher for the

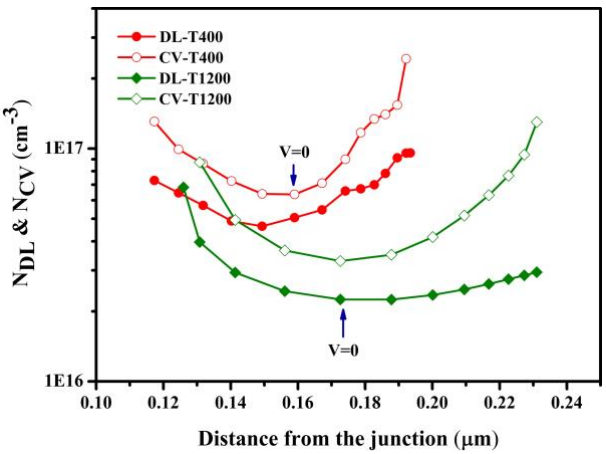

Figure 7.5 Capacitance-voltage (CV) and deep-level capacitance profiling (DLCP) of different thick Sb_2Se_3 solar cells.

T1200 solar cells. A higher V_{oc} within T1200 devices could refer to a larger depletion region, resulting in better charge carrier separation. Significantly different FF and R_s values are observed where R_s increases with increasing thickness, which may suggest a higher bulk defect density in the thicker film. Besides, the R_{shunt} value is found to be higher for the T400 devices, representing better isolation with fewer shunt paths.

Until now, the results suggest that increasing the thickness of Sb_2Se_3 films is accompanied by an increase in defect density. To evaluate the distribution of carrier density and defect characteristics across solar cells, we have performed C-V and DLCP measurements. For the T400 and T1200 devices, the doping concentrations in the space charge region were estimated at approximately 4.6×10^{16} cm^{-3} and 2.2×10^{16} cm^{-3}, respectively. The difference between the C-V and DLCP profiles in the T1200 device underscores the detrimental impact of deep-level defects on performance, as DLCP measurements are more sensitive to localized deep-level states often associated with intrinsic defects like vacancies, antisite defects, or interstitials. This indicates that intrinsic defects in thicker Sb_2Se_3 film are more pronounced, either due to growth conditions or simply the increased thickness, which leads to higher bulk defect density. These defects trap charge carriers, reducing the effective carrier density in the depletion region, as reflected by lower values in the DLCP profile compared to the C-V profile. This disparity

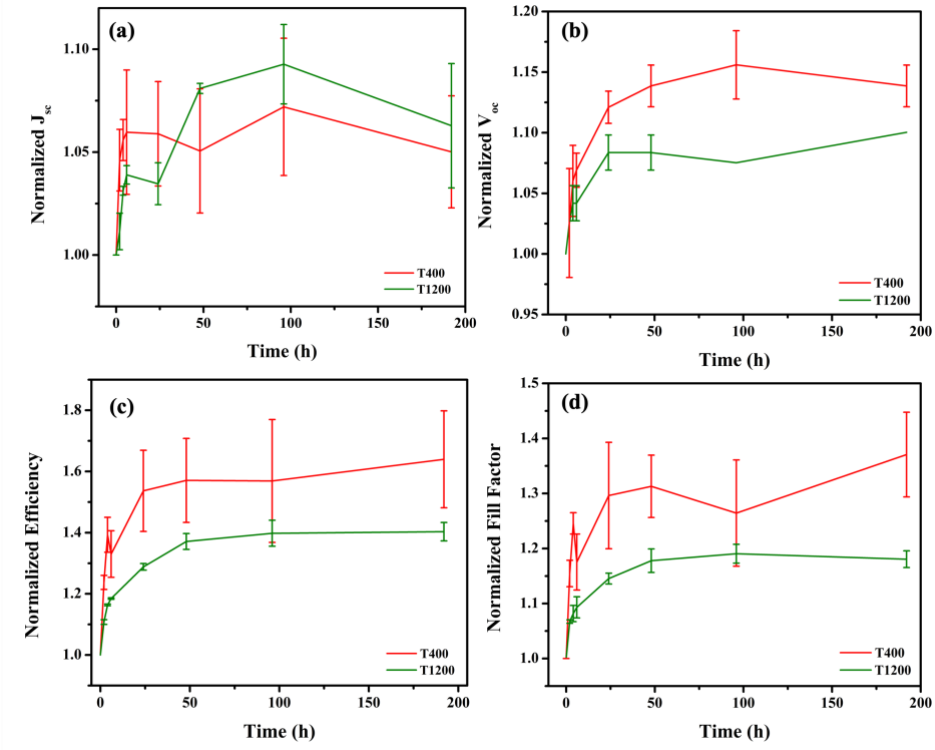

Figure 7.6 Photovoltaic parameters degradation over time under accelerated stability test of various thick Sb_2Se_3 solar cells.

suggests that a portion of charge carriers measured in the C-V profile are immobilized in deep traps, increasing recombination losses and lowering device efficiency. In summary, although thicker film improve crystallinity and extend the depletion region, the higher defect density ultimately limits the photovoltaic efficiency of these films.

AST has been carried out in order to assess the longevity and degradation mechanisms of the solar cells (Figure 7.6). Both devices show sharp improvements in photovoltaic parameters in the first 24 hours. Beyond this initial phase, parameters are stabilized during the 200-hour test. The T1200 solar cells exhibited the least improvement among the devices, especially in J_{sc}. Additionally, after 100 hours, there was a slight decrease in J_{sc} for all devices, while the other parameters remained stable. Increased J_{sc} and V_{oc} point toward better charge carrier collection and reduced recombination losses within solar cells, possibly due to improved material quality or defect passivation. These results thus highlight further scope for improvement, with low-temperature post-annealing treatment in an air ambient being one particular attempt at optimization.

7.4 Impact of Post-annealing Treatment

This section discusses the impact of applied post-annealing treatment (PAT) on Sb_2Se_3 solar cells with various thicknesses.

7.4.1 Structural and Compositional Analysis

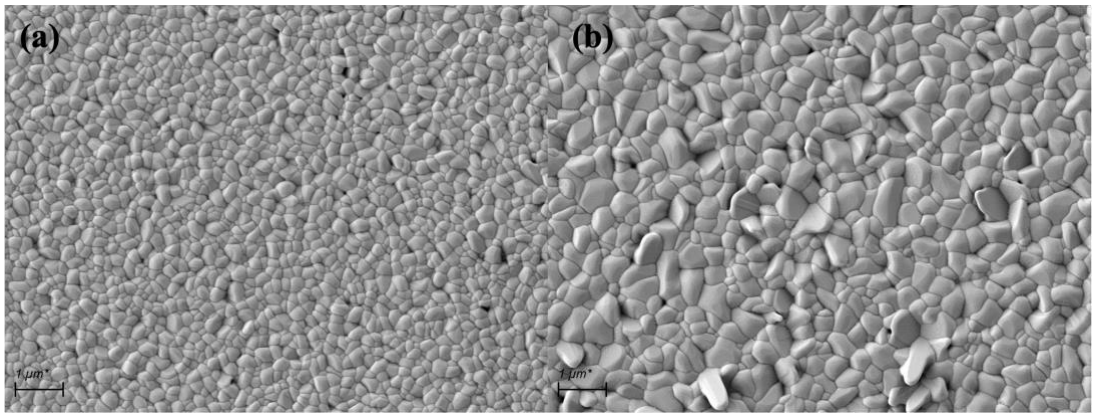

Figure 7.7 Top-view SEM images of (a) T400 and (b) T1200 Sb_2Se_3 thin films after PAT.

After PAT, the SEM images reveal negligible morphological changes across Sb_2Se_3 films. Despite the low temperature of PAT, a slight grain size increase (approximately 10–30 nm) and more pronounced surface protrusions can be observed. While not included here, AFM analysis revealed an increase of approximately 10 nm in the root mean square (RMS) roughness, supporting the surface changes. Since annealing was conducted in a normal atmosphere, oxide combinations such as Sb_2O_3 or SeO_2 are likely to form. Firstly, EDX results (Table 7.2) show that the annealing caused a deviation in the elemental ratio. Oxygen presence on the surface has been found to be negligible, but it shows a higher atomic percentage in the T400 film. Raman spectroscopy did not show any secondary phases, probably due to the challenge of detecting these combinations when they exist only within a few nanometers.

Table 7.2 EDX results of T400 and T1200 Sb_2Se_3 films after PAT

Sample	Atomic percentage (%)			
	Sb	Se	O	Sb:Se
T400	20.7	31.3	4.2	0.66
T400-PAT	19.5	31.2	4.4	0.62
T1200	26.2	38	0.6	0.68
T1200-PAT	28.8	39.2	0.8	0.73

Additionally, we performed SIMS analysis to get a compositional profile through the film. Oxygen is present throughout both T400 and T1200 solar cells, with a higher concentration in the T400 cells, likely due to increased diffusion as influenced by reduced thickness. The elemental ratio of Se to Sb remained practically identical in the SIMS analysis in both films before and after PAT.

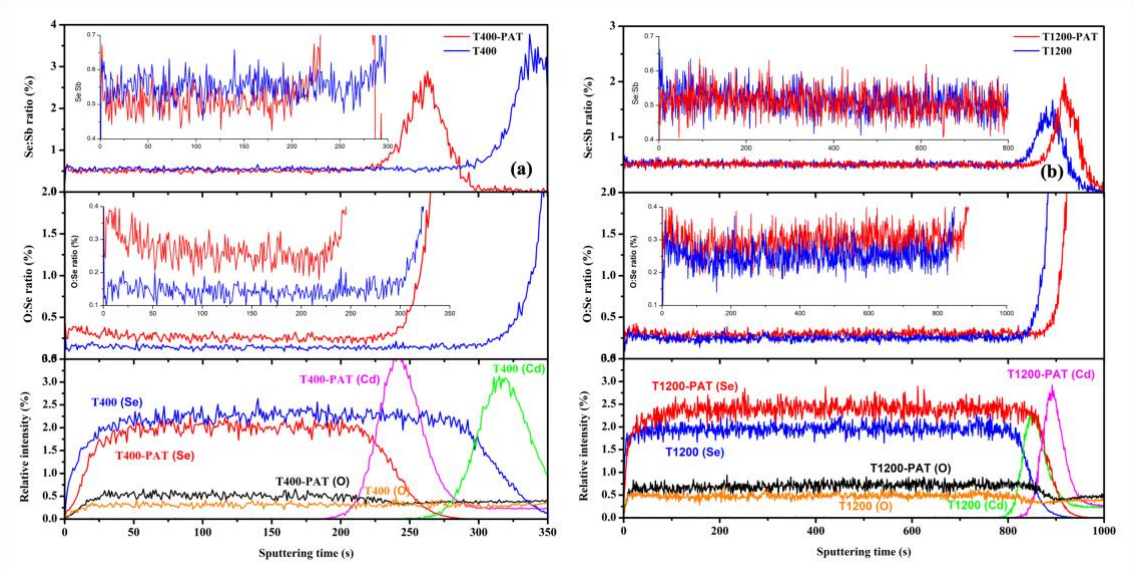

Figure 7.8 SIMS analysis of Sb_2Se_3 solar cells with different thicknesses before and after PAT.

XRD peaks of Sb_2Se_3 films, as shown in Figure 7.9(a), after PAT are similar to those without PAT. Despite the low annealing temperature, TC analysis shows slight reorientation in both films. Interestingly, in the thicker film, TC values of grain orientations with a larger angle to the surface, such as the [021] and [221], increase, while a reflection with a smaller angle to the surface, such as the [041], decreases. The predominant orientation becomes the [041], in the T400 film, while [021] reflection presents the highest values of TC before PAT. PAT promotes an increase in the average grain size and modifies Sb_2Se_3 structural orientations, resulting in a more columnar structure in the thicker film and a more inclined orientation in the thinner film.

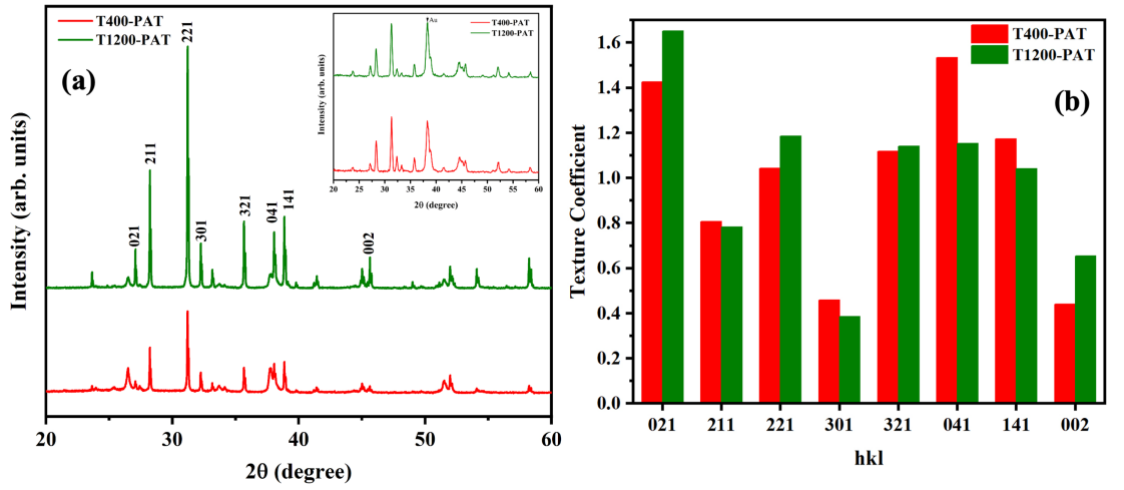

Figure 7.9 (a) XRD peaks, GIXRD peaks in the inset, and (b) texture coefficient of CdSe/Sb_2Se_3 solar cell with varying Sb_2Se_3 film thickness after PAT.

7.4.2 Device Characterization

J-V results of best-performed solar cells illustrate that PAT improved the efficiency of devices by over 1% (Figure 7.10 (a). Table 7.3). After PAT, all photovoltaic parameters have improved in both cases except the J_{sc} of the T400 cell. Although V_{oc} and FF exhibit the highest value in the T400 cell, these parameters have enhanced after PAT in the T1200 device. We can see a similar trend for shunt and series resistances, showing improved values of the ultra-thin Sb_2Se_3

Table 7.3 Photovoltaic parameters of best-performing T400 and T1200 Sb_2Se_3 solar cells after PAT.

Sample	J_{sc} (mA/cm^2)	V_{oc} (mV)	FF (%)	η (%)	R_{shunt} (Ω)	R_{series} (Ω)
T400-PAT	24.3	314	48.4	3.7	924	29.5
T1200-PAT	25	314	42.1	3.3	485.6	35.9

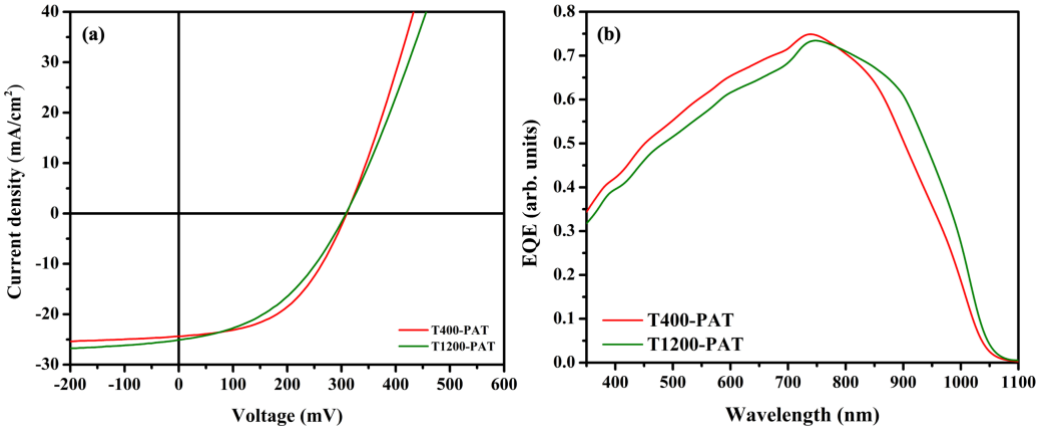

Figure 7.10 (a) J-V and (b) EQE results of T400 and T1200 Sb_2Se_3 solar cells after PAT.

solar cells. The observed rollover effect in T1200 solar cells vanishes after PAT. As mentioned earlier, the rollover effect, originating from a Schottky barrier at the back contact, reduces charge carrier collection. Fleck et al. [112] demonstrated that air exposure to Sb_2Se_3 film results in the formation of thin Sb_2O_3 film. The thin ultra-thin film of Sb_2O_3 acts like a passivation layer and leaves a Se-rich Sb_2Se_3 film. Thus, it reduces the back contact barrier, leading to the improvement of V_{oc} and FF values. Similarly, this PAT reduces the rollover effect, plus it decreases the series resistance.

The boxplot of twelve solar cells in each device is presented in Figure 7.11 (a-d). The uniformity of parameters, especially J_{sc}, is maintained the same way after PAT but the distribution of other values is still narrower in T1200 solar cells. The homogenesis distribution

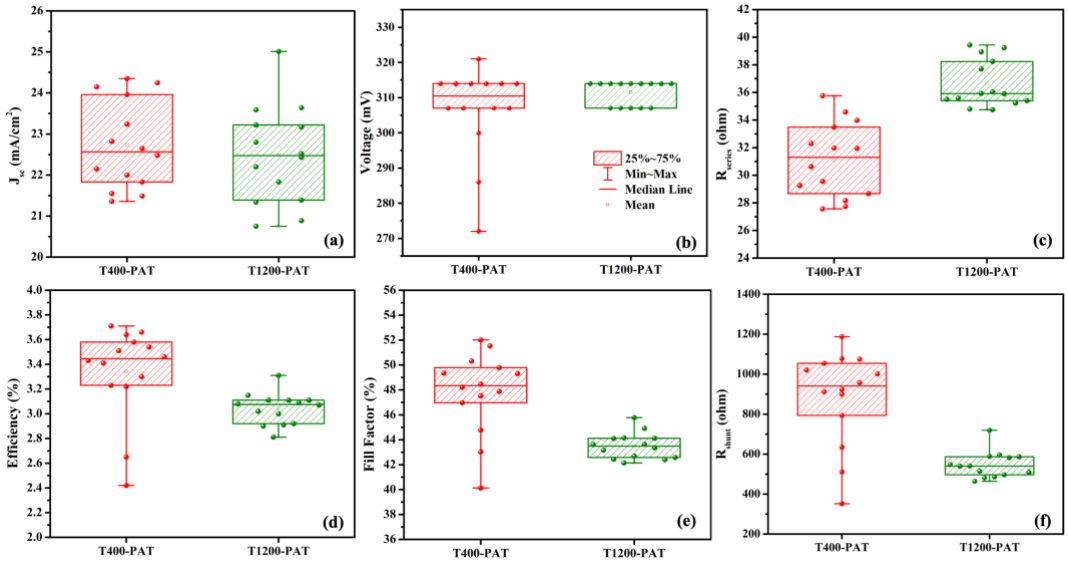

Figure 7.11 Plot box of photovoltaic parameters of T400 and T1200 Sb_2Se_3 solar cells after PAT.

of photovoltaic values could refer to a more developed crystal structure of T1200 film, as we observed in SEM and XRD analysis. Despite improving all photovoltaic parameters in T400 solar cells after PAT, J_{sc} shows the same average value with T1200 solar cells without increase. This observation could refer to the improvement of ribbon orientations in the T1200 film after PAT. Interestingly, R_{shunt} is lower in T1200 solar cells, suggesting more shunt patches in thicker film, but still, V_{oc} depicts a slightly higher average. Regardless of the improved structural properties of T1200 Sb_2Se_3 after PAT, solar cells based on 400 nm of Sb_2Se_3 had a higher performance.

The PAT improves the EQE response (Figure 7.10 (b)) of T1200 cell mainly for wavelengths longer than 850 nm, illustrating the reduction of losses at the back. The broad increase of EQE in the whole spectrum of the T1200-PAT cell supports the higher J_{sc} via an enhanced carrier collection. Although J_{sc} exhibits similar values after PAT for T400 cells, the EQE drops after 700 nm, which could be associated with the absorption coefficient.

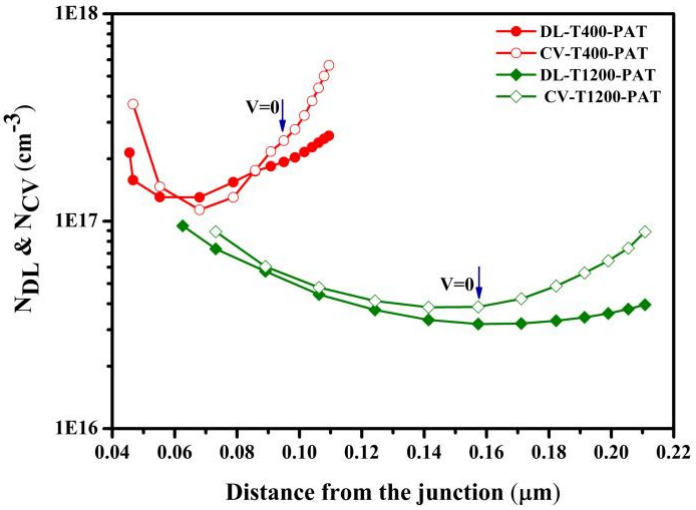

Figure 7.12 Capacitance-voltage (CV) and deep-level capacitance profiling (DLCP) of T400 and T1200 Sb_2Se_3 solar cells after PAT.

Figure 7.12 depicts CV and DLCP measurements of T400-PAT and T1200-PAT devices. The doping density of T400-PAT and T1200-PAT solar cells increases to $1.3x10^{17}$ cm^{-3} and $3.1x10^{16}$ cm^{-3}, respectively, leading to a reduced SCR width, shown at V=0 points on the graph. The overlap between CV and DLCP curves confirms a passivation effect introduced by PAT, which reduces defect-related carrier recombination. While the carrier distribution is more uniform in the T1200 solar cell, a noticeable deviation between CV and DLCP values persists far from the junction, indicating the presence of bulk defects in the absorber layer.

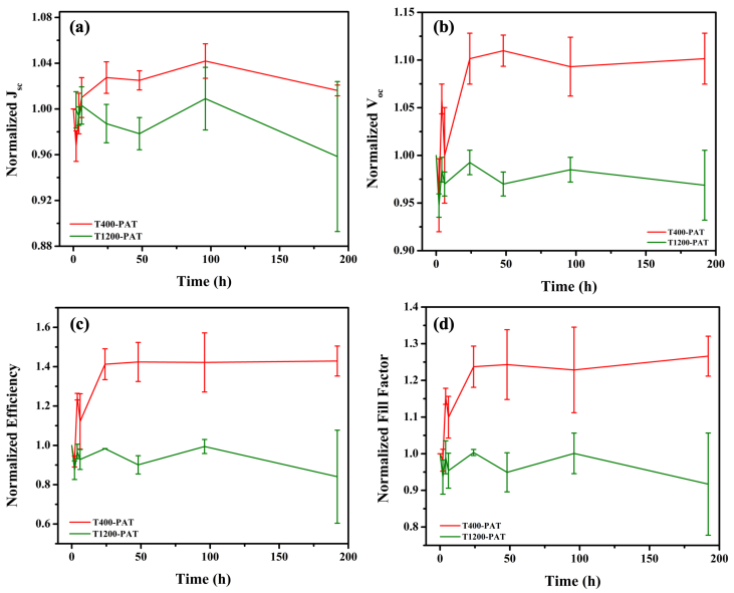

Figure 7.13 Photovoltaic parameters degradation over time under accelerated stability test of various thick Sb_2Se_3 solar cells after PAT.

Figure 7.13 shows how the solar cells performed during a stability test under stress conditions after PAT. For both devices, the J_{sc} fluctuated a bit before slightly decreasing by the end of the test. The V_{oc} stayed steady for the thicker T1200-PAT solar cells, but for the thinner T400-PAT solar cells, it actually improved over time. Both efficiency and fill factor showed a noticeable rise during the first 24 hours and then remained stable for the rest of the test.

Overall, both devices performed well under these conditions, but the thinner absorber layer in the T400-PAT cells performed better. It seems that thinner layers not only handle thermal and illumination stress better but also help extract charges more efficiently, with fewer losses from recombination, inconsistent with CV and DLCP results.

Interestingly, the early improvement in efficiency and fill factor for the T400-PAT cells might be because of the "healing effect" of some defects or improved quality of the material interfaces. On the other hand, the thicker T1200-PAT cells might have faced more thermal stress, which could slow down defect healing or even lead to more recombination over time.

7.5 Discussion and Conclusion

In the first consideration, the absorption coefficient defines the absorber thickness in thin film solar cells. In Sb_2Se_3 solar cells, the thickness can be reduced significantly due to its high absorption coefficient. A thin absorber can reduce the recombination because of the short travel

path of charge carriers, resulting in higher V_{oc}. In contrast, J_{sc} can show higher values in thicker films due to improvement in light absorption. However, the optimum thickness comes from balancing J_{sc} and V_{oc} values, ensuring the best performance.

It has been reported that 400 nm absorbs light under 800 wavelengths completely, and 1 μm is needed for light absorption in longer wavelengths [34]. Since absorber thickness influences the optoelectrical properties of the material, we have applied and compared a thin, 400 nm, and a thick, 1200 nm, Sb_2Se_3 films in our superstrate device structure.

We have observed that both thin- and thick-based solar cells illustrate comparable V_{oc} values, which is slightly higher for thicker-based solar cells. Surprisingly, our ultra-thin solar cell shows a higher J_{sc} and is well-performed overall. According to structural analysis, Sb_2Se_3 is more developed with 1200 nm thickness, which is expected to offer better charge transport. However, EQE results reveal carrier collection problems for T1200 solar cells, and deviation of CV and DLCP profiling shows higher defect density in these solar cells.

Our results suggest that increasing the thickness, regardless of more developed structural properties, forms more defects, lowering the overall performance of solar cells.

These devices have improved under AST, suggesting the potential for a post-annealing treatment. Therefore, as presented in Chapter Five, we applied our optimized annealing treatment in ambient air on both devices. Despite the low temperature of this PAT, we observed slight development in grain size and re-orientation of crystal pattern, which was more decent in 1200 nm film. After PAT, the photovoltaic parameters of both solar cells improved, and we observed that efficiency increased by more than 1%. The J_{sc} value remains the same in thinner-based solar cells, while it has increased in the case of thicker film. Additionally, this treatment reduces the back contact barrier, as observed from J-V curves before PAT, particularly in T1200 solar cells. The most improved values are V_{oc} and fill factor in both cases, although T400 still performs better. This suggests a passivation-like effect of PAT on films. CV and DLCP profiling confirm a reduction in defect density concentration after PAT. The SIMS profiles show the oxygen diffusion through the absorber to the junction. Thus, our results suggest that oxygen passivates some defects, resulting in an improvement in the overall performance of the solar cells. Also, positive oxygen influence at junctions [63], [64] and back contact [112] has been reported before.

Chapter Eight

Conclusion and Future Work

8.1 Final Summary

This thesis focused on studying and optimizing Sb_2Se_3 thin film solar cells grown via thermal evaporation. However, optimizing thin film solar cell performance includes various aspects such as window layer, active layer, and back contact. In this work, Cd-based and Cd-free window layers for Sb_2Se_3-based solar cells have been introduced and compared. Also, the influence of the absorber thickness and a post-annealing treatment of finished devices have been analyzed.

Initially, CdS by CBD was adjusted and applied to the superstate structure devices. Subsequently, CdSe by thermal evaporation was introduced as an alternative buffer layer. The influence of these window layers on the structure and electronic properties of Sb_2Se_3 solar cells was thoroughly compared and presented in Chapter Five. Moreover, due to the challenges of Cd-based materials (for example, parasitic absorption and cadmium diffusion), thin SnO_2 layers were applied via atomic layer deposition with precise thickness control.

Since CdSe improved J_{sc} and stability of the devices, a comparison between the application of SnO_2 and CdSe window layers was discussed in Chapter Six.

Finally, in Chapter Seven, solar cells with thin and thick absorber layers were fabricated and investigated to understand the impact of thickness on the performance of the finished devices. Also, we applied and analyzed an air post-annealing treatment on these devices, observing a clear efficiency improvement during our optimization process.

8.1.1 Window layer: Cd-free or Cd-based

In the structure of p-n junction-based solar cells, the window layer plays a crucial role in carrier dynamics and efficient light transmission. Forming an effective band alignment at the interface of the window and active layer leads to higher-performance devices. However, measuring the exact band alignment is challenging, as results often vary depending on the fabrication process.

CdS has been the most widely used window layer for thin film solar cells, such as CIGS, CZTS, CdTe (in the past) and also Sb_2Se_3. The most popular growth method of CdS is CBD due to its conformal coverage with extremely low thickness, which allows for a significant reduction of the parasitic absorption. In this work CdS was deposited by CBD, resulting in an average solar conversion efficiency of 3.5%.

The detrimental influence of sulfur diffusion on device performance prompted us to replace this layer. Moreover, growing Sb_2Se_3 by thermal evaporation often results in Se deficiency within the film. Thus, CdSe was introduced as a window layer, as its selenium content could avoid sulfur diffusion in the absorber, selenium diffusion in the buffer layer and reduce the selenium loss. Despite its narrow band gap, the application of CdSe increased J_{sc} compared to the CdS buffer layer. Replacing CdS with CdSe kept the morphology and the growth of Sb_2Se_3 polycrystals similar but improved the device stability remarkably. Testing the performance of solar cells for 960 h under the accelerated lifetime stability tests showed a significant reduction of the instability of the cells keeping it in the range of about 10%.
We observed a smaller cell volume for the Sb_2Se_3 grown on CdS, suggesting a sulfur diffusion at the junction. By introducing CdSe, the suppression of sulfur diffusion was confirmed, as well as the absence of Se deficiency at the junction. Regardless of the lower V_{oc} of CdSe-based solar cells, the devices have demonstrated a better performance than CdS-based solar cells.

Besides that, CdSe increased the carrier collection even at shorter wavelengths compared to CdS; but the parasitic absorption remained a bottleneck. Both CdS and CdSe solar cells presented Cd detrimental interdiffusion at the junction. To address these issues, SnO_2 was applied as a transparent, Cd-free window layer. A void-free, ultra-thin film of SnO_2 was grown by atomic layer deposition at the EMPA laboratories. Applying 15 nm of SnO_2 film in the same structure as the CdSe-based devices led to similar efficiency. Unlike CdS and CdSe, SnO_2 improved the morphology of Sb_2Se_3 films by increasing the grain size (to approximately 1µm) and the compactness. The comparison between SnO_2 and CdSe showed a more columnar growth of the Sb_2Se_3 grains on SnO_2 layers. As expected, SnO_2 improved carrier collection at shorter wavelength regions, increasing J_{sc} up to 28 mA/cm^2. On average, SnO_2 also illustrated higher V_{oc} and efficiency than Cd-based buffer layers.

8.1.2 Active layer: Thin or Thick

The absorption coefficient defines the thickness of the active layer, and due to the high absorption coefficient of Sb_2Se_3, the thickness can be reduced to 400 nm. According to the literature, this thickness is enough for light absorption under near-infrared regions [34]. Zhou et al. reported Sb_2Se_3 grown by rapid thermal evaporation with a thickness of 390 nm and an efficiency of 5.6% [47]. However, the thickness most reported for Sb_2Se_3 absorbers is between 600 nm to 1 μm [55], [116], [117].

The influence of Sb_2Se_3 thickness was studied by applying 400 nm and 1200 nm thick absorber layers. By increasing the thickness, the morphology of Sb_2Se_3 film developed by slightly increasing the grain sizes, as expected. Also, a subtle reorientation of planes toward the preferred crystal orientation of (001) was observed. Surprisingly, the solar cell with 400 nm of absorber performed better and had higher J_{sc}. Also, it showed a lower defect concentration and a higher charge carrier density. Our results illustrated that increasing the thickness of thermally evaporated Sb_2Se_3 film results in higher defect density, which decreases the device's performance.

8.1.3 Post-annealing Treatment of Solar Cells

Under our optimization process, post-annealing treatment at a low temperature of 150°C was discovered to be efficient in improving the performance of solar cells. To understand the impact of this treatment, it was applied to devices with different thicknesses. Sb_2Se_3 films showed slight developments in morphology and structure after PAT. The overall performance increased after this treatment, especially the V_{oc} and fill factor, resulting in higher efficiency. After PAT, the defect concentration was also reduced, confirming the treatment's role as a passivation layer. Moreover, the presence of oxygen was detected differently across the thin and thick films, suggesting diffusion behaved differently depending on the thickness. Based on our results, an ultra-thin layer of Sb_2Se_3 is even more efficient than a higher thickness, resulting in the same J_{sc}. Also, applying a simple PAT in air ambient acts like a passivation layer, improving the efficiency.

8.2 Impact of This Work and Future Suggestions

This work contributed to investigating Sb_2Se_3 thin film solar cells by exploring different window layers and the impact of absorber thickness. It showed the potential role of the CdSe-based and Cd-free window layers on the structural and optoelectronic properties of Sb_2Se_3 devices. Also, applying a thin layer of Sb_2Se_3 illustrated the capability of this photovoltaic material to deliver higher efficiency when combined with a passivation method. Building upon these findings, future work could explore:

- *Studying the band alignment between CdSe and Sb_2Se_3*

A detailed investigation of the interface could provide deeper insights to guide strategies for further improving device performance.

- *Exploring scalable growth techniques for SnO_2*

While ALD-deposited SnO_2 film performed well as a window layer in Sb_2Se_3 solar cells, the deposition method is unsuitable for large-scale manufacturing. Studying alternative scalable methods could facilitate scaling up the technology.

- *Systematic Study of Defects in Sb_2Se_3 Solar Cells*

The complex defects and V_{oc} deficiency of Sb_2Se_3 solar cells suggest a systematic material study to deepen the knowledge of the structural and electronic properties. According to the literature, defect formation under poor conditions of selenium is more likely. These defects can be located by analyzing Sb_2Se_3 films with various elemental ratios. Also, applying two different growth methods in the same structure of Sb_2Se_3 solar cells would help to understand how fabrication conditions influence defect formation and device performance. Also, integrating experimental results with computational methods, such as Density Functional Theory (DFT), can help to strengthen the knowledge about defect dynamics and electronic properties.

- *Challenges in Reproducibility of Sb_2Se_3*

While technical issues can happen during any experimental research, the reproducibility of Sb_2Se_3 devices remains challenging. The problem can originate from many factors during the fabrication process and growth conditions. Nevertheless, a systematic observation approach, possibly coupled with machine learning techniques, could be the key to developing methods that enhance reproducibility.

References

[1] J. Hansen, R. Ruedy, M. Sato, and K. Lo, "World of Change: Global Temperatures," *Reviews of Geophysics*, vol. 48, no. 4, Jan. 2020, doi: 10.1029/2010RG000345/ABSTRACT.

[2] H. Ritchie, P. Rosado, and M. Roser, "Energy Production and Consumption," *Our World in Data*, Jul. 2020, Accessed: Jan. 13, 2025. [Online]. Available: https://ourworldindata.org/energy-production-consumption

[3] "The Paris Agreement - Publication | UNFCCC." Accessed: Jan. 13, 2025. [Online]. Available: https://unfccc.int/documents/184656

[4] J. Nelson, "The Physics of Solar Cells," *The Physics of Solar Cells*, May 2003, doi: 10.1142/P276.

[5] John. Perlin, "From space to earth : the story of solar electricity," p. 224, 2002.

[6] G. M. Wilson, M. Al-Jassim, W. K. Metzger, al -, and M. A. Green, "Silicon solar cells: evolution, high-efficiency design and efficiency enhancements," *Semicond Sci Technol*, vol. 8, no. 1, p. 1, Jan. 1993, doi: 10.1088/0268-1242/8/1/001.

[7] M. A. Green, "Third generation photovoltaics: solar cells for 2020 and beyond," *Physica E Low Dimens Syst Nanostruct*, vol. 14, no. 1–2, pp. 65–70, Apr. 2002, doi: 10.1016/S1386-9477(02)00361-2.

[8] P. Würfel, "Physics of Solar Cells: From Principles to New Concepts," *Physics of Solar Cells: From Principles to New Concepts*, pp. 1–186, Dec. 2007, doi: 10.1002/9783527618545.

[9] F. Ise and P. Projects GmbH, "Photovoltaics Report-Fraunhofer Institute for Solar Energy Systems, ISE with the support of PSE Projects GmbH," 2024. [Online]. Available: www.ise.fraunhofer.de

[10] "Chinese PV Industry Brief: JA Solar, Longi, Jinko, Trina report Q3 results – pv magazine International." Accessed: Jan. 13, 2025. [Online]. Available: https://www.pv-magazine.com/2024/11/05/chinese-pv-industry-brief-ja-solar-longi-jinko-trina-report-q3-results/

[11] K. L. Chopra, P. D. Paulson, and V. Dutta, "Thin-film solar cells: an overview," *Progress in Photovoltaics: Research and Applications*, vol. 12, no. 2–3, pp. 69–92, Mar. 2004, doi: 10.1002/PIP.541.

[12] K. L. Chopra and S. R. Das, "Thin Film Deposition Techniques," *Thin Film Solar Cells*, pp. 195–273, 1983, doi: 10.1007/978-1-4899-0418-8_5.

[13] T. Matsui *et al.*, "High-efficiency amorphous silicon solar cells: Impact of deposition rate on metastability," *Appl Phys Lett*, vol. 106, no. 5, Feb. 2015, doi: 10.1063/1.4907001/29229.

[14] "First Solar opens US research facility – pv magazine International." Accessed: Jan. 13, 2025. [Online]. Available: https://www.pv-magazine.com/2024/07/19/first-solar-opens-us-research-facility/

[15] J. Keller *et al.*, "High-concentration silver alloying and steep back-contact gallium grading enabling copper indium gallium selenide solar cell with 23.6% efficiency," *Nature Energy 2024 9:4*, vol. 9, no. 4, pp. 467–478, Feb. 2024, doi: 10.1038/s41560-024-01472-3.

[16] "LONGi Sets New World-Record for Silicon Solar Cell Efficiency, Launching 2nd Generation Ultra-Efficient BC-Based Module -LONGi." Accessed: Jan. 13, 2025. [Online]. Available: https://www.longi.com/en/news/longi-hi-mo9-bc-world-record/

[17] Y. Li *et al.*, “Suppressing Element Inhomogeneity Enables 14.9% Efficiency CZTSSe Solar Cells,” *Advanced Materials*, vol. 36, no. 25, p. 2400138, Jun. 2024, doi: 10.1002/ADMA.202400138.
[18] J. Poortmans and V. Arkhipov, “Thin Film Solar Cells Fabrication, Characterization and Applications,” *Thin Film Solar Cells Fabrication, Characterization and Applications*, pp. 1–471, Sep. 2006, doi: 10.1002/0470091282.
[19] M. A. Green, A. Ho-Baillie, and H. J. Snaith, “The emergence of perovskite solar cells,” *Nature Photonics 2014 8:7*, vol. 8, no. 7, pp. 506–514, Jun. 2014, doi: 10.1038/nphoton.2014.134.
[20] A. J. Nozik, M. C. Beard, J. M. Luther, M. Law, R. J. Ellingson, and J. C. Johnson, “Semiconductor quantum dots and quantum dot arrays and applications of multiple exciton generation to third-generation photovoltaic solar cells,” *Chem Rev*, vol. 110, no. 11, pp. 6873–6890, Nov. 2010, doi: 10.1021/CR900289F.
[21] R. A. Hatton, “Organic Photovoltaics,” *A Comprehensive Guide to Solar Energy Systems*, pp. 255–277, Jan. 2018, doi: 10.1016/B978-0-12-811479-7.00012-9.
[22] R. Guerrero-Lemus, R. Vega, T. Kim, A. Kimm, and L. E. Shephard, “Bifacial solar photovoltaics – A technology review,” *Renewable and Sustainable Energy Reviews*, vol. 60, pp. 1533–1549, Jul. 2016, doi: 10.1016/J.RSER.2016.03.041.
[23] N. N. Lal, Y. Dkhissi, W. Li, Q. Hou, Y. B. Cheng, and U. Bach, “Perovskite Tandem Solar Cells,” *Adv Energy Mater*, vol. 7, no. 18, p. 1602761, Sep. 2017, doi: 10.1002/AENM.201602761.
[24] P. Heinstein, C. Ballif, and L. E. Perret-Aebi, “Building integrated photovoltaics (BIPV): Review, potentials, barriers and myths,” *Green*, vol. 3, no. 2, pp. 125–156, Jun. 2013, doi: 10.1515/GREEN-2013-0020/MACHINEREADABLECITATION/RIS.
[25] K. W. Böer, *Handbook of the Physics of Thin-Film Solar Cells*. Springer, 2013. doi: 10.1007/978-3-642-36748-9.
[26] D. Abou-Ras, T. Kirchartz, and U. Rau, “Advanced Characterization Techniques for Thin Film Solar Cells,” *Advanced Characterization Techniques for Thin Film Solar Cells*, Apr. 2011, doi: 10.1002/9783527636280.
[27] L. C. Hirst and N. J. Ekins-Daukes, “Fundamental losses in solar cells,” *Progress in Photovoltaics: Research and Applications*, vol. 19, no. 3, pp. 286–293, May 2011, doi: 10.1002/PIP.1024.
[28] K. W. Böer, “Handbook of the physics of thin-film solar cells,” *Handbook of the Physics of Thin-Film Solar Cells*, pp. 1–882, Jan. 2013, doi: 10.1007/978-3-642-36748-9/COVER.
[29] “Quantum Efficiency | PVEducation.” Accessed: Jan. 21, 2025. [Online]. Available: https://www.pveducation.org/pvcdrom/solar-cell-operation/quantum-efficiency
[30] Y. Zhou *et al.*, “Solution-Processed Antimony Selenide Heterojunction Solar Cells,” *Adv Energy Mater*, vol. 4, no. 8, p. 1301846, Jun. 2014, doi: 10.1002/AENM.201301846.
[31] Z. Duan *et al.*, “Sb2Se3 Thin-Film Solar Cells Exceeding 10% Power Conversion Efficiency Enabled by Injection Vapor Deposition Technology,” *Advanced Materials*, vol. 34, no. 30, p. 2202969, Jul. 2022, doi: 10.1002/ADMA.202202969.
[32] Y. Zhao *et al.*, “Regulating deposition kinetics via a novel additive-assisted chemical bath deposition technology enables fabrication of 10.57%-efficiency Sb2Se3 solar cells,” *Energy Environ Sci*, vol. 15, no. 12, pp. 5118–5128, Oct. 2022, doi: 10.1039/d2ee02261c.
[33] H. Zhu *et al.*, “Antimony selenide thin-film solar cells,” *Semicond Sci Technol*, vol. 31, no. 6, p. 063001, Apr. 2016, doi: 10.1088/0268-1242/31/6/063001.

[34] C. Chen *et al.*, “Optical properties of amorphous and polycrystalline Sb2Se3 thin films prepared by thermal evaporation,” *Appl Phys Lett*, vol. 107, no. 4, Jul. 2015, doi: 10.1063/1.4927741/30528.
[35] C. Chen *et al.*, “Characterization of basic physical properties of Sb2Se3 and its relevance for photovoltaics,” *Frontiers of Optoelectronics*, vol. 10, no. 1, pp. 18–30, Mar. 2017, doi: 10.1007/S12200-017-0702-Z/METRICS.
[36] C. Chen *et al.*, “Characterization of basic physical properties of Sb2Se3 and its relevance for photovoltaics,” *Frontiers of Optoelectronics*, vol. 10, no. 1, pp. 18–30, Mar. 2017, doi: 10.1007/S12200-017-0702-Z/METRICS.
[37] A. Kyono, M. Kimata, M. Matsuhisa, Y. Miyashita, and K. Okamoto, “Low-temperature crystal structures of stibnite implying orbital overlap of Sb 5s2 inert pair electrons,” *Phys Chem Miner*, vol. 29, no. 4, pp. 254–260, 2002, doi: 10.1007/S00269-001-0227-1/METRICS.
[38] N. W. Tideswell, F. H. Kruse, and J. D. McCullough, “The crystal structure of antimony selenide, Sb2Se3,” *urn:issn:0365-110X*, vol. 10, no. 2, pp. 99–102, Feb. 1957, doi: 10.1107/S0365110X57000298.
[39] C. N. Savory and D. O. Scanlon, “The complex defect chemistry of antimony selenide,” *J Mater Chem A Mater*, vol. 7, no. 17, pp. 10739–10744, Apr. 2019, doi: 10.1039/C9TA02022E.
[40] M. Huang, P. Xu, D. Han, J. Tang, and S. Chen, “Complicated and Unconventional Defect Properties of the Quasi-One-Dimensional Photovoltaic Semiconductor Sb 2 Se 3,” *ACS Appl Mater Interfaces*, vol. 11, no. 17, pp. 15564–15572, May 2019, doi: 10.1021/ACSAMI.9B01220.
[41] U. Wijesinghe, G. Longo, and O. S. Hutter, “Defect engineering in antimony selenide thin film solar cells,” *Energy Advances*, vol. 2, no. 1, pp. 12–33, Jan. 2023, doi: 10.1039/D2YA00232A.
[42] R. Tang *et al.*, “Highly efficient and stable planar heterojunction solar cell based on sputtered and post-selenized Sb2Se3 thin film,” *Nano Energy*, vol. 64, p. 103929, Oct. 2019, doi: 10.1016/J.NANOEN.2019.103929.
[43] C. N. Savory and D. O. Scanlon, “The complex defect chemistry of antimony selenide,” *J Mater Chem A Mater*, vol. 7, no. 17, pp. 10739–10744, Apr. 2019, doi: 10.1039/C9TA02022E.
[44] X. Liu *et al.*, “Thermal evaporation and characterization of Sb2Se3 thin film for substrate Sb2Se3/CdS solar cells,” *ACS Appl Mater Interfaces*, vol. 6, no. 13, pp. 10687–10695, Jul. 2014, doi: 10.1021/AM502427S/SUPPL_FILE/AM502427S_SI_001.PDF.
[45] X. Liu *et al.*, “Enhanced Sb2Se3 solar cell performance through theory-guided defect control,” *Progress in Photovoltaics: Research and Applications*, vol. 25, no. 10, pp. 861–870, Oct. 2017, doi: 10.1002/PIP.2900.
[46] L. Wang *et al.*, “Stable 6%-efficient Sb2Se3 solar cells with a ZnO buffer layer,” *Nature Energy 2017 2:4*, vol. 2, no. 4, pp. 1–9, Mar. 2017, doi: 10.1038/nenergy.2017.46.
[47] Y. Zhou *et al.*, “Thin-film Sb2Se3 photovoltaics with oriented one-dimensional ribbons and benign grain boundaries,” *Nature Photonics 2015 9:6*, vol. 9, no. 6, pp. 409–415, May 2015, doi: 10.1038/nphoton.2015.78.
[48] O. S. Hutter, L. J. Phillips, P. J. Yates, J. D. Major, and K. Durose, “CSS Antimony Selenide Film Morphology and High Efficiency PV Devices,” *2018 IEEE 7th World Conference on Photovoltaic Energy Conversion, WCPEC 2018 - A Joint Conference of 45th IEEE PVSC, 28th PVSEC and 34th EU PVSEC*, pp. 27–31, Nov. 2018, doi: 10.1109/PVSC.2018.8547653.

[49] X. Liu *et al.*, “Enhanced Sb2Se3 solar cell performance through theory-guided defect control,” *Progress in Photovoltaics: Research and Applications*, vol. 25, no. 10, pp. 861–870, Oct. 2017, doi: 10.1002/PIP.2900.
[50] K. Yang, B. Li, and G. Zeng, “Sb2Se3 thin film solar cells prepared by pulsed laser deposition,” *J Alloys Compd*, vol. 821, p. 153505, Apr. 2020, doi: 10.1016/J.JALLCOM.2019.153505.
[51] G. X. Liang *et al.*, “Thermally induced structural evolution and performance of Sb2Se3 films and nanorods prepared by an easy sputtering method,” *Solar Energy Materials and Solar Cells*, vol. 174, pp. 263–270, Jan. 2018, doi: 10.1016/J.SOLMAT.2017.09.008.
[52] Y. Zhao *et al.*, “Regulating deposition kinetics via a novel additive-assisted chemical bath deposition technology enables fabrication of 10.57%-efficiency Sb2Se3 solar cells,” *Energy Environ Sci*, vol. 15, no. 12, pp. 5118–5128, Dec. 2022, doi: 10.1039/D2EE02261C.
[53] M. Luo *et al.*, “Thermal evaporation and characterization of superstrate CdS/Sb2Se3 solar cells,” *Appl Phys Lett*, vol. 104, no. 17, p. 173904, May 2014, doi: 10.1063/1.4874878.
[54] Y. Zhou *et al.*, “Thin-film Sb2Se3 photovoltaics with oriented one-dimensional ribbons and benign grain boundaries,” *Nature Photonics 2015 9:6*, vol. 9, no. 6, pp. 409–415, May 2015, doi: 10.1038/nphoton.2015.78.
[55] X. Wen *et al.*, “Vapor transport deposition of antimony selenide thin film solar cells with 7.6% efficiency,” *Nature Communications 2018 9:1*, vol. 9, no. 1, pp. 1–10, Jun. 2018, doi: 10.1038/s41467-018-04634-6.
[56] Q. Fu *et al.*, “Reflection and lattice mismatch loss analysis in Sb2Se3 solar cells,” *Semicond Sci Technol*, vol. 37, no. 11, p. 115006, Oct. 2022, doi: 10.1088/1361-6641/AC93AB.
[57] V.-Q. Hoang *et al.*, “Interface engineering of antimony selenide solar cells: a review on the optimization of energy band alignments,” *Journal of Physics: Energy*, vol. 4, no. 4, p. 044002, Aug. 2022, doi: 10.1088/2515-7655/AC8578.
[58] F. Ayala-Mato, O. Vigil-Galán, M. Courel, and M. M. Nicolás-Marín, “Analysis of The Efficiency In Sb2Se3 Thin-Film Solar Cells Using Alternative Buffer Layers In n-p and n-i-p Structures By Numerical Simulation.,” Jun. 2021, doi: 10.21203/RS.3.RS-644062/V1.
[59] K. Kumar, P. Sharma, S. K. Saini, R. Yadav, S. P. Singh, and M. Kumar, “Substrate-Dependent Ultrafast Charge-Carrier Dynamics: Unveiling the Annealing Effect on Optoelectronic Performance of Sb2Se3 Thin Films,” *Journal of Physical Chemistry C*, vol. 127, no. 49, pp. 23706–23718, Dec. 2023, doi: 10.1021/ACS.JPCC.3C05015.
[60] Y. Zhou *et al.*, “Buried homojunction in CdS/Sb2Se3 thin film photovoltaics generated by interfacial diffusion,” *Appl Phys Lett*, vol. 111, no. 1, p. 013901, Jul. 2017, doi: 10.1063/1.4991539.
[61] H. Shiel *et al.*, “Natural Band Alignments and Band Offsets of Sb2Se3Solar Cells,” *ACS Appl Energy Mater*, vol. 3, no. 12, pp. 11617–11626, Dec. 2020, doi: 10.1021/ACSAEM.0C01477.
[62] W. Wang *et al.*, “Interface Etching Leads to the Inversion of the Conduction Band Offset between the CdS/Sb2Se3 Heterojunction and High-Efficient Sb2Se3 Solar Cells,” *ACS Appl Energy Mater*, vol. 5, no. 2, pp. 2531–2541, Feb. 2022, doi: 10.1021/ACSAEM.1C04078.
[63] C. Ou, K. Shen, Z. Li, H. Zhu, T. Huang, and Y. Mai, “Bandgap tunable CdS:O as efficient electron buffer layer for high-performance Sb2Se3 thin film solar cells,”

Solar Energy Materials and Solar Cells, vol. 194, pp. 47–53, Jun. 2019, doi: 10.1016/J.SOLMAT.2019.01.043.
[64] L. Guo *et al.*, "Interface Engineering via Sputtered Oxygenated CdS:O Window Layer for Highly Efficient Sb2Se3 Thin-Film Solar Cells with Efficiency Above 7%," *Solar RRL*, vol. 3, no. 10, p. 1900225, Oct. 2019, doi: 10.1002/SOLR.201900225.
[65] L. Guo *et al.*, "Interfacial engineering of oxygenated chemical bath–deposited CdS window layer for highly efficient Sb2Se3 thin-film solar cells," *Materials Today Physics*, vol. 10, p. 100125, Aug. 2019, doi: 10.1016/J.MTPHYS.2019.100125.
[66] Y. Liu *et al.*, "Nanorod array-induced growth of high-quality Sb2Se3 absorber layers for efficient planar solar cells," *J Alloys Compd*, vol. 949, p. 169729, Jul. 2023, doi: 10.1016/J.JALLCOM.2023.169729.
[67] L. Wang *et al.*, "Ambient CdCl2 treatment on CdS buffer layer for improved performance of Sb2Se3 thin film photovoltaics," *Appl Phys Lett*, vol. 107, no. 14, p. 143902, Oct. 2015, doi: 10.1063/1.4932544.
[68] G. Li, Z. Li, X. Liang, C. Guo, K. Shen, and Y. Mai, "Improvement in Sb 2 Se 3 Solar Cell Efficiency through Band Alignment Engineering at the Buffer/Absorber Interface," *ACS Appl Mater Interfaces*, vol. 11, no. 1, pp. 828–834, Jan. 2019, doi: 10.1021/ACSAMI.8B17611.
[69] S. Lu *et al.*, "In situ investigation of interfacial properties of Sb2Se3heterojunctions," *Appl Phys Lett*, vol. 116, no. 24, Jun. 2020, doi: 10.1063/5.0008879/986119.
[70] H. Shiel *et al.*, "Natural Band Alignments and Band Offsets of Sb2Se3Solar Cells," *ACS Appl Energy Mater*, vol. 3, no. 12, pp. 11617–11626, Dec. 2020, doi: 10.1021/ACSAEM.0C01477/ASSET/IMAGES/LARGE/AE0C01477_0010.JPEG.
[71] W. Wang, Z. Cao, H. Wang, J. Luo, and Y. Zhang, "Remarkable Cd-free Sb 2 Se 3 solar cell yield achieved by interface band-alignment and growth orientation screening," *J Mater Chem A Mater*, vol. 9, no. 47, pp. 26963–26975, Dec. 2021, doi: 10.1039/D1TA08404F.
[72] C. H. Don *et al.*, "Reactive DC Sputtered TiO2 Electron Transport Layers for Cadmium-Free Sb2Se3 Solar Cells," *Adv Energy Mater*, vol. 14, no. 34, p. 2401077, Sep. 2024, doi: 10.1002/AENM.202401077.
[73] C. H. Don *et al.*, "Multi-Phase Sputtered TiO2-Induced Current–Voltage Distortion in Sb2Se3 Solar Cells," *Adv Mater Interfaces*, vol. 10, no. 20, p. 2300238, Jul. 2023, doi: 10.1002/ADMI.202300238.
[74] X. Wen *et al.*, "Magnetron sputtered ZnO buffer layer for Sb2Se3 thin film solar cells," *Solar Energy Materials and Solar Cells*, vol. 172, pp. 74–81, Dec. 2017, doi: 10.1016/J.SOLMAT.2017.07.014.
[75] S. Lu *et al.*, "Sb2Se3 Thin-Film Photovoltaics Using Aqueous Solution Sprayed SnO2 as the Buffer Layer," *Adv Electron Mater*, vol. 4, no. 1, p. 1700329, Jan. 2018, doi: 10.1002/AELM.201700329.
[76] P. Luo *et al.*, "Electron Transport Layer Engineering Induced Carrier Dynamics Optimization for Efficient Cd-Free Sb2Se3 Thin-Film Solar Cells," *Small*, vol. 20, no. 4, p. 2306516, Jan. 2024, doi: 10.1002/SMLL.202306516.
[77] D. B. Li *et al.*, "Stable and efficient CdS/Sb2Se3 solar cells prepared by scalable close space sublimation," *Nano Energy*, vol. 49, pp. 346–353, Jul. 2018, doi: 10.1016/J.NANOEN.2018.04.044.
[78] C. Chen *et al.*, "6.5% Certified Efficiency Sb2Se3 Solar Cells Using PbS Colloidal Quantum Dot Film as Hole-Transporting Layer," *ACS Energy Lett*, vol. 2, no. 9, pp. 2125–2132, Sep. 2017, doi: 10.1021/ACSENERGYLETT.7B00648/SUPPL_FILE/NZ7B00648_SI_001.PDF.

[79] J. Zhang, R. Kondrotas, S. Lu, C. Wang, C. Chen, and J. Tang, “Alternative back contacts for Sb2Se3 solar cells,” *Solar Energy*, vol. 182, pp. 96–101, Apr. 2019, doi: 10.1016/J.SOLENER.2019.02.050.
[80] T. P. Shalvey, C. H. Don, L. Bowen, T. D. Veal, and J. D. Major, “Understanding the Role of Organic Hole Transport Layers on Pinhole Blocking and Performance Improvement in Sb2Se3 Solar Cells,” *Adv Mater Interfaces*, vol. 11, no. 35, p. 2400394, Dec. 2024, doi: 10.1002/ADMI.202400394.
[81] Z. Li *et al.*, “9.2%-efficient core-shell structured antimony selenide nanorod array solar cells,” *Nature Communications 2019 10:1*, vol. 10, no. 1, pp. 1–9, Jan. 2019, doi: 10.1038/s41467-018-07903-6.
[82] G. X. Liang *et al.*, “Sputtered and selenized Sb2Se3 thin-film solar cells with open-circuit voltage exceeding 500 mV,” *Nano Energy*, vol. 73, p. 104806, Jul. 2020, doi: 10.1016/J.NANOEN.2020.104806.
[83] K. S. Harsha, “Principles of Vapor Deposition of Thin Films,” *Principles of Vapor Deposition of Thin Films*, pp. 1–1160, Jan. 2006, doi: 10.1016/B978-0-08-044699-8.X5000-1.
[84] C. Y. Y. Cheol Seong Hwang, *Atomic Layer Deposition for Semiconductors*. New York, NY: Springer US, 2014.
[85] J. T. Tanskanen and S. F. Bent, “Insights into the surface chemistry of tin oxide atomic layer deposition from quantum chemical calculations,” *Journal of Physical Chemistry C*, vol. 117, no. 37, pp. 19056–19062, Sep. 2013, doi: 10.1021/JP4063324.
[86] R. W. M. K. D. P. Theodor Schneller, *Chemical Solution Deposition of Functional Oxide Thin Films*. Vienna, Austria: Springer Vienna, 2013.
[87] G. F. Harrington and J. Santiso, “Back-to-Basics tutorial: X-ray diffraction of thin films,” *J Electroceram*, vol. 47, no. 4, pp. 141–163, Dec. 2021, doi: 10.1007/S10832-021-00263-6/TABLES/3.
[88] Z. Shen and S. Fearn, “Back-to-basics tutorial: Secondary ion mass spectrometry (SIMS) in ceramics,” *J Electroceram*, pp. 1–28, Dec. 2024, doi: 10.1007/S10832-024-00375-9/FIGURES/12.
[89] T. Baines *et al.*, “Incorporation of CdSe layers into CdTe thin film solar cells,” *Solar Energy Materials and Solar Cells*, vol. 180, pp. 196–204, Jun. 2018, doi: 10.1016/J.SOLMAT.2018.03.010.
[90] N. R. Paudel, Y. Yan, and A. Phys Lett, “Enhancing the photo-currents of CdTe thin-film solar cells in both short and long wavelength regions Quantifying electron-phonon coupling in CdTe 1−x Se x nanocrystals via coherent phonon manipulation Effect of intermixing at CdS/CdTe interface on defect properties,” *Appl. Phys. Lett*, vol. 105, p. 183510, 2014, doi: 10.1063/1.4901532.
[91] L. Guo *et al.*, “Improved stability and efficiency of CdSe/Sb2Se3 thin-film solar cells,” *Solar Energy*, vol. 188, pp. 586–592, Aug. 2019, doi: 10.1016/J.SOLENER.2019.06.042.
[92] Robert Alan Young, *The Rietveld Method*, vol. 5. Oxford, UK: Oxford University Press, 1995.
[93] L. Lutterotti, “Maud: a Rietveld analysis program designed for the internet and experiment integration,” *Acta Crystallogr A*, vol. 56, no. s1, 2000, doi: 10.1107/s0108767300021954.
[94] A. Kumar, V. Kumar, A. Romeo, C. Wiemer, and G. Mariotto, “Raman Spectroscopy andIn SituXRD Probing of the Thermal Decomposition of Sb2Se3Thin Films,” *Journal of Physical Chemistry C*, vol. 125, no. 36, pp. 19858–19865, 2021, doi: 10.1021/acs.jpcc.1c05047.

[95] A. Kumar, V. Kumar, A. Romeo, C. Wiemer, and G. Mariotto, “Raman Spectroscopy and In Situ XRD Probing of the Thermal Decomposition of Sb 2 Se 3 Thin Films,” *J. Phys. Chem. C*, vol. 125, p. 2022, 2021, doi: 10.1021/acs.jpcc.1c05047.
[96] J. T. Heath, J. D. Cohen, and W. N. Shafarman, “Bulk and metastable defects in CuIn 1Àx Ga x Se 2 thin films using drive-level capacitance profiling”, doi: 10.1063/1.1633982¸.
[97] C. Chen *et al.*, “Vapor transport deposition of antimony selenide thin film solar cells with 7.6% efficiency,” *Nat Commun*, vol. 9, no. 1, 2018, doi: 10.1038/s41467-018-04634-6.
[98] M. Huang, P. Xu, D. Han, J. Tang, and S. Chen, “Complicated and Unconventional Defect Properties of the Quasi-One-Dimensional Photovoltaic Semiconductor Sb 2 Se 3,” *ACS Appl Mater Interfaces*, vol. 11, no. 17, pp. 15564–15572, 2019, doi: 10.1021/acsami.9b01220.
[99] A. Stoliaroff *et al.*, “Deciphering the Role of Key Defects in Sb2Se3, a Promising Candidate for Chalcogenide-Based Solar Cells,” *ACS Appl Energy Mater*, vol. 3, no. 3, pp. 2496–2509, 2020, doi: 10.1021/acsaem.9b02192.
[100] M. Huang, P. Xu, D. Han, J. Tang, and S. Chen, “Complicated and Unconventional Defect Properties of the Quasi-One-Dimensional Photovoltaic Semiconductor Sb 2 Se 3,” *ACS Appl Mater Interfaces*, vol. 11, no. 17, pp. 15564–15572, May 2019, doi: 10.1021/ACSAMI.9B01220/SUPPL_FILE/AM9B01220_SI_001.PDF.
[101] D. B. Li *et al.*, “Stable and efficient CdS/Sb2Se3 solar cells prepared by scalable close space sublimation,” *Nano Energy*, vol. 49, no. April, pp. 346–353, 2018, doi: 10.1016/j.nanoen.2018.04.044.
[102] A. Mavlonov *et al.*, “A review of Sb2Se3 photovoltaic absorber materials and thin-film solar cells,” *Solar Energy*, vol. 201, pp. 227–246, May 2020, doi: 10.1016/J.SOLENER.2020.03.009.
[103] Z. Zhang *et al.*, “Suppressing the Trapping Process by Interfacial Charge Extraction in Antimony Selenide Heterojunctions,” *ACS Energy Lett*, vol. 6, no. 5, pp. 1740–1748, May 2021, doi: 10.1021/ACSENERGYLETT.0C02660.
[104] Z. Chen *et al.*, “Efficiency improvement of Sb2Se3 solar cells based on La-doped SnO2 buffer layer,” *Solar Energy*, vol. 187, pp. 404–410, Jul. 2019, doi: 10.1016/J.SOLENER.2019.05.026.
[105] X. Wang *et al.*, “Enhancement in the efficiency of Sb2Se3 solar cells using a TiO2-modified SnO2 buffer layer,” *Vacuum*, vol. 166, pp. 201–205, Aug. 2019, doi: 10.1016/J.VACUUM.2019.05.001.
[106] J. Zhou *et al.*, “Dual-function of CdCl2 treated SnO2 in Sb2Se3 solar cells,” *Appl Surf Sci*, vol. 534, p. 147632, Dec. 2020, doi: 10.1016/J.APSUSC.2020.147632.
[107] F. Pattini *et al.*, “Role of the substrates in the ribbon orientation of Sb2Se3 films grown by Low-Temperature Pulsed Electron Deposition,” *Solar Energy Materials and Solar Cells*, vol. 218, p. 110724, Dec. 2020, doi: 10.1016/J.SOLMAT.2020.110724.
[108] N. Fleck *et al.*, “Identifying Raman modes of Sb2Se3 and their symmetries using angle-resolved polarised Raman spectra,” *J. Mater. Chem. A*, vol. 8, no. 17, pp. 8337–8344, 2020, doi: 10.1039/D0TA01783C.
[109] X. Hu *et al.*, “Improving the efficiency of Sb2Se3 thin-film solar cells by post annealing treatment in vacuum condition,” *Solar Energy Materials and Solar Cells*, vol. 187, pp. 170–175, Dec. 2018, doi: 10.1016/J.SOLMAT.2018.08.006.
[110] S. Yao *et al.*, “Improved Performance of Thermally Evaporated Sb2Se3 Thin-Film Solar Cells via Substrate-Cooling-Speed Control and Hydrogen-Sulfide Treatment,” *ACS Appl Mater Interfaces*, vol. 12, no. 21, pp. 24112–24124, May 2020, doi: 10.1021/ACSAMI.0C03674.

[111] X. Liu *et al.*, “Improving the performance of Sb2Se3 thin film solar cells over 4% by controlled addition of oxygen during film deposition,” *Progress in Photovoltaics: Research and Applications*, vol. 23, no. 12, pp. 1828–1836, Dec. 2015, doi: 10.1002/PIP.2627.
[112] N. Fleck *et al.*, “How Oxygen Exposure Improves the Back Contact and Performance of Antimony Selenide Solar Cells,” *ACS Appl Mater Interfaces*, vol. 12, no. 47, pp. 52595–52602, Nov. 2020, doi: 10.1021/ACSAMI.0C14256.
[113] X. Li, K. Shen, Q. Li, Y. Deng, P. Zhu, and D. Wang, “Roll-over behavior in current-voltage curve introduced by an energy barrier at the front contact in thin film CdTe solar cell,” *Solar Energy*, vol. 165, pp. 27–34, May 2018, doi: 10.1016/J.SOLENER.2018.02.075.
[114] J. H. Siew, Y. H. Chen, Y. L. Chang, C. H. Lai, and T. Y. Lin, “Heat Soaking for Improving Rollover from S at the Back of CIGSSe Solar Cells,” *IEEE J Photovolt*, vol. 13, no. 4, pp. 503–509, Jul. 2023, doi: 10.1109/JPHOTOV.2023.3271891.
[115] S. H. Demtsu and J. R. Sites, “Effect of back-contact barrier on thin-film CdTe solar cells,” *Thin Solid Films*, vol. 510, no. 1–2, pp. 320–324, Jul. 2006, doi: 10.1016/J.TSF.2006.01.004.
[116] Y. Yang, T. Guo, D. Wang, X. Xiong, and B. Li, “Preparation and characterization of pulsed laser deposited CdSe window layer for Sb2Se3 thin film solar cell,” *Journal of Materials Science: Materials in Electronics*, vol. 31, no. 16, pp. 13947–13956, Aug. 2020, doi: 10.1007/S10854-020-03954-Y/TABLES/3.
[117] D. A. Sindi, T. P. Shalvey, and J. D. Major, “Comparison of one and two-stage growth approaches for close space sublimation deposition of Sb2Se3 thin film solar cells,” *Mater Sci Semicond Process*, vol. 174, p. 108161, May 2024, doi: 10.1016/J.MSSP.2024.108161.
[118] K. Momma and F. Izumi, “VESTA 3 for three-dimensional visualization of crystal, volumetric and morphology data,” *J Appl Crystallogr*, vol. 44, no. 6, pp. 1272–1276, Dec. 2011, doi: 10.1107/S0021889811038970/HTTPS://JOURNALS.IUCR.ORG/SERVICES/RSS.HTML.
[119] “Atomic Layer Deposition – InRedox.” Accessed: Jan. 23, 2025. [Online]. Available: https://www.inredox.com/technology/atomic-layer-deposition/